QUANTITATIVE MODELING OF POLYMER SCRATCH BEHAVIOR

A Dissertation

by

MOHAMMAD MOTAHER HOSSAIN

Submitted to the Office of Graduate and Professional Studies of
Texas A&M University
in partial fulfillment of the requirements for the degree of

DOCTOR OF PHILOSOPHY

Chair of Committee, Hung-Jue Sue
Committee Members, Anastasia Muliana
Terry Creasy
Janet Bluemel
Head of Department, Andreas A. Polycarpou

December 2013

Major Subject: Mechanical Engineering

ABSTRACT

Scratch-induced surface deformation is a complex mechanical process due to high strain rate large-scale deformation, non-linear material response, heat dissipation and complex stress field evolved during the process. The rate, time, temperature and pressure dependent behavior of polymers, and the surface condition of the interacting surfaces also add to the complexity. In order to gain in-depth understanding of polymer scratch behavior; this dissertation focuses on numerical analysis and experimental study of scratch-induced deformation in polymers, leading to quantitative prediction of scratch behavior of model amorphous polymers.

A comprehensive three-dimensional finite element method (FEM) parametric study has been performed by incorporating key characteristics of polymer constitutive behavior to investigate the effect of material parameters and surface properties on the evolution of scratch-induced deformation in polymers, along with relevant experimentation. The qualitative analyses using FEM simulation and experimental work suggest that indeed correlation between material and surface properties, and scratch-induced damage mechanisms can be established.

To quantitatively predict the scratch behavior of polymers *via* FEM, PC and SAN model systems are chosen. A modification of Ree-Eyring theory is used to assess the rate dependent behavior of model polymers at high strain rates based on the experimental data obtained at low strain rates. By including the rate and pressure dependent mechanical behavior and pressure dependent frictional behavior in the FEM model, good

agreement has been found between FEM simulation and experimental observations. The results suggest that, by including proper constitutive relationship and friction model in the numerical analysis, the scratch behavior of polymers can be quantitatively predicted with reasonable success.

DEDICATION

To my parents

ACKNOWLEDGEMENTS

I would like to thank my committee chair, Dr. Sue, and my committee members, Dr. Muliana, Dr. Creasy, and Dr. Bluemel, for their guidance and support throughout the course of this research. I would also like to acknowledge the generous support provided by the Texas A&M Scratch Behavior Consortium members in this research endeavor. Special thanks to Styrolution GmbH and BASF SE for providing model polymer systems that made this work possible.

I would like to give my most sincere gratitude to Dr. H.-J. Sue, who has provided valuable guidance and served as a role model during my stay here at Texas A&M University.

Special thanks to Ehsan Moghbelli, Kevin White and Spencer Hawkins for helping me out in this research. I would also like to thank Dr. Han Jiang, Dr. Robert Browning, Allan Moyse and Noah Smith for their assistance and inspiration. Thanks also to my friends and colleagues for making my time here a great experience.

Next, I would like to thank Dr. Shyamal Kanti Biswas, who has been my inspiration in difficult times.

Finally, I would like to sincerely thank my father, Tofail Ahmed, my mother, Anowara Begum, my brother, sister, and their families, and my wife, Sonia, for their love and support.

TABLE OF CONTENTS

Page

ABSTRACT ii

DEDICATION iv

ACKNOWLEDGEMENTS v

TABLE OF CONTENTS vi

LIST OF FIGURES ix

LIST OF TABLES xv

CHAPTER

I INTRODUCTION 1

- 1.1 Overview of Polymer Scratch Research 2
- 1.2 Research Scope 12
- 1.3 Layout of the Dissertation 15

II PARAMETRIC STUDIES 17

- 2.1 FEM Parametric Study on Effect of different Constitutive Parameters [10, 14] 17
  - 2.1.1 FEM Modeling 18
  - 2.1.2 Results and Discussion 21
- 2.2 Effect of Asymmetric Constitutive Behavior [11] 30
  - 2.2.1 FEM Modeling 30
  - 2.2.2 Experimental 31
  - 2.2.3 Results and Discussion 34
- 2.3 Influence of Surface Friction [13] 44
  - 2.3.1 FEM Modeling 45
  - 2.3.2 Experimental 46
  - 2.3.3 Results and Discussion 48

III FACTORS CONSIDERED FOR QUANTITATIVE MODELING 62

- 3.1 Rate Dependent Mechanical Behavior of Amorphous Polymers 62
- 3.2 Pressure Dependent Mechanical Behavior of Polymers 76

3.3 Frictional Behavior during Sliding Contact involving Polymers 78

IV EXPERIMENTAL OBSERVATION OF MODEL SYSTEMS 87

4.1 Model Systems 87
4.2 Mechanical Property Characterization 88
  4.2.1 Testing Procedure 88
  4.2.2 Results and Discussion 89
4.3 Dynamic Mechanical Analysis 94
  4.3.1 Analysis Procedure 94
  4.3.2 Results and Discussion 94
4.4 Measurement of Surface Friction Coefficient 103
  4.4.1 Measurement Procedure 103
  4.4.2 Results and Discussion 103
4.5 Scratch-induced Deformation 104
  4.5.1 Scratch Test 104
  4.5.2 Microscopic Observation 105
  4.5.3 Results and Discussion 105

V FEM MODEL FOR QUANTITATIVE ANALYSIS 114

5.1 Constitutive Model 115
5.2 Contact Model 123
5.3 FEM Model Geometry, Boundary and Loading Conditions 125

VI RESULTS AND DISCUSSION ON QUANTITATIVE MODELING..127

6.1 Comparison of FEM Simulation and Experiment for Scratch Behavior of PC 127
6.2 Comparison of FEM Simulation and Experiment for Scratch Behavior of SAN 132

VII CONCLUSIONS AND CONSIDERATIONS FOR FUTURE RESEARCH 137

7.1 Summary and Conclusions 137
7.2 Considerations for Future Research 139
  7.2.1 Extended Study on Quantitative Modeling 139
  7.2.2 FEM Simulation of Brittle Damage Features Developed during Scratch 140
  7.2.3 FEM Simulation of Fish-scale Formation during Scratch 141

REFERENCES 142

APPENDIX A 151

APPENDIX B 153

APPENDIX C 155

LIST OF FIGURES

FIGURE Page

1.1 Schematic of the scratching process. 3

1.2 Tribology research branches. 3

1.3 Schematic of the cross section of scratch groove. 6

1.4 Maximum principal stress contour plot at normal loads of - (a) 8 N; (b) 14 N; (c) 20 N. [7]. 8

1.5 SEM of - (a) Parabolic crack pattern in PC; (b) Onset of fish-scale formation in TPO; (c) Well developed fish-scale in TPO; (d) Pseudo fish-scale pattern mixed with crazes/voids in PS; (e) Parabolic crack pattern in Epoxy [7]. 8

1.6 Polymer scratch damage evolution map [7]. 9

1.7 Compressive stress-strain behaviors of three glassy polymers [37]. 14

2.1 FEM simulation model. 19

2.2 Various steps involved during a scratch process (load-controlled). 20

2.3 Piece-wise linear true stress-strain plot with relevant material parameters used to describe the constitutive behavior of polymer substrate in FEM simulation. 21

2.4 Scratch depth profile for Case 1. 23

2.5 Plot of shoulder height as a function of scratch normal load for Case 1. 24

2.6 Scratch depth profile for Case 2. 25

2.7 Plot of shoulder height as a function of scratch normal load for Case 2. 26

2.8 Scratch depth profile for Case 3. 27

2.9 Plot of shoulder height as a function of scratch normal load for Case 3. 27

2.10 Scratch depth profile for Case 4. 28

2.11 Plot of shoulder height as a function of scratch normal load for Case 4. 29

FIGURE Page

2.12 Scratch depth profile. 36

2.13 Plot of shoulder height as a function of scratch normal load. 36

2.14 Comparison of scratch depth in SAN 19, SAN 27B and SAN 27C. 38

2.15 Comparison of shoulder height in SAN 19, SAN 27B and SAN 27C. 38

2.16 Comparison of scratch depth in SAN 19 and PC. 40

2.17 Comparison of shoulder height in SAN 19 and PC. 40

2.18 Micrographs of the scratch groove obtained *via* VLSCM in (a) SAN; (b) PC model systems. 42

2.19 Comparison of surface roughness in SAN 19 and PC. 43

2.20 LYSS *vs.* HYSS scratch depth profiles obtained *via* FEM simulation. 49

2.21 Plots of shoulder height of LYSS and HYSS as a function of scratch normal load obtained *via* FEM simulation. 49

2.22 Effect of yield stress and surface friction on onset of groove formation obtained *via* FEM simulation. 50

2.23 Relative frictional effect on scratch depth in LYSS and HYSS obtained *via* FEM simulation. 52

2.24 LSHS *vs.* HSHS scratch depth profiles obtained *via* FEM simulation. 53

2.25 Plots of shoulder height of LSHS and HSHS as a function of scratch normal load obtained *via* FEM simulation. 53

2.26 Effect of strain hardening slope and surface friction on onset of groove formation obtained *via* FEM simulation. 54

2.27 Relative frictional effect on scratch depth in LSHS and HSHS obtained *via* FEM simulation. 55

2.28 Uniaxial compression stress-strain curve for SAN and PC model systems. 56

2.29 Coefficient of friction measured for the model polymers. 57

FIGURE Page

2.30 Onset load for scratch groove formation in the model systems. 58

2.31 Comparison of scratch depth between SAN and PC. Dotted trend-line denotes SAN and solid trend-line denotes PC..59

2.32 Comparison of shoulder height between SAN and PC. Dotted trend-line denotes SAN and solid trend-line denotes PC...................................59

3.1 True compressive stress-strain curves of PC at various strain rates [48]. 63

3.2 Comparison of Ree-Eyring and Argon model with compressive experimental data of PC [54]..65

3.3 Theoretical compressive yield stress *vs.* logarithm of strain rate at 60 ºC for an amorphous polymer to compare the three models [54].............65

3.4 Comparison of experimental compressive and tensile yield stresses with the Ree-Eyring model with constants value listed in Table 3.1 at a constant strain rate, $\dot{\varepsilon} = 4.16\times10^{-3}$ /s [58]. 69

3.5 Plot of the ratio of tensile yield stress to temperature as a function of logarithm of strain rate (Range I denotes the region of single activated process and range I′ denotes the region of two rate activated process) [58]. 69

3.6 Plot of the compressive yield stress *vs.* temperature at constant strain rate [57]. 71

3.7 Plot of yield stress to temperature as a function of logarithm of strain rate for PVC [56]. 72

3.8 Plot of yield stress to temperature as a function of logarithm of strain rate for PMMA [61]..73

3.9 PC loss tangent peak for α-transition as a function of temperature and strain rate [48]...75

3.10 Decomposition α and β components of PC storage modulus curve at 3.2×10^{-3} /s [48]. 75

3.11 DSR model prediction of PC elastic modulus at different strain rates (The vertical dash line denotes room temperature: 298 ºK) [48]. 76

FIGURE Page

3.12 Effect of hydrostatic pressure on the initial moduli of HDPE and PC [68]. 77

3.13 Plot of tensile yield stress as a function of pressure in PC [69]. 78

3.14 Pressure dependent shear stress-strain response in PC [80]. 82

3.15 Maximum shear stress as a function of pressure in PMMA (ʘ: yield, ×: fracture) [81]. 83

3.16 Variation of coefficient of friction due to adhesion as a function of applied normal load using 5 mm spherical steel tip on PTFE [38]. 84

4.1 PC - (a) Representative stress-strain plot in compression; (b) True compressive yield stress as a function of strain rate. 90

4.2 PC - (a) Compressive modulus; (b) Yield strain in compression; as a function of strain rate. 90

4.3 PC - (a) Yield stress; (b) Modulus; (c) Yield strain; in tension as a function of strain rate. 91

4.4 SAN - (a) Representative stress-strain plot in compression; (b) True compressive yield stress as a function of strain rate. 92

4.5 SAN - (a) Compressive modulus; (b) Yield strain in compression; as a function of strain rate. 93

4.6 SAN - (a) Strength; (b) Modulus; in tension as a function of strain rate. 93

4.7 PC storage modulus and loss tangent as a function of temperature at 1 Hz. 95

4.8 Shift in β transition with increasing frequency in PC. 96

4.9 Dependence of PC storage modulus on strain rate as a function of temperature (°K). 97

4.10 Decomposition of PC storage modulus into α and β components at a strain rate of 2×10^{-2} /s. 98

4.11 Prediction of onset of β restriction in PC (The vertical line denotes room temperature). 98

FIGURE Page

4.12 SAN storage modulus and loss tangent as a function of temperature at 1 Hz. 100

4.13 Dependence of SAN storage modulus on strain rate as a function of temperature (°K). 101

4.14 Storage modulus (solid line) and loss modulus (dashed line) of PMMA as a function of temperature at 1 Hz [48]. 102

4.15 True compressive yield stress of PMMA as a function of true strain rate (logarithmic scale) [48]. 102

4.16 Coefficient of friction measured using 10 mm × 10 mm flat tip for the model systems. 104

4.17 Plot of scratch depth as a function of scratch normal load in PC. 106

4.18 Plot of shoulder height as a function of scratch normal load in PC. 107

4.19 Plot of scratch width as a function of scratch normal load in PC. 107

4.20 Plot of scratch depth as a function of scratch normal load in SAN. 109

4.21 Plot of shoulder height as a function of scratch normal load in SAN. 109

4.22 Plot of scratch width as a function of scratch normal load in SAN. 110

4.23 Percent viscoelastic recovery in - (a) Scratch depth; (b) Shoulder height; in PC. 112

4.24 Percent viscoelastic recovery in - (a) Scratch depth; (b) Shoulder height; in SAN. 112

5.1 Yield surface in principal stress space for Drucker-Prager criterion [92]. 116

5.2 Yield surface in meridional plane for linear Drucker-Prager model [40]. 118

5.3 PC - (a) Yield stress; and (b) Post-yield behavior; in uniaxial compression used for FEM modeling. 120

5.4 SAN - (a) Yield stress; and (b) Post-yield behavior; in uniaxial compression used for FEM modeling. 120

FIGURE Page

5.5 Friction model used in the FEM simulation. 125

6.1 Comparison of FEM simulation and experiments on scratch depth evolution as a function of scratch normal load for PC. 128

6.2 Comparison of FEM simulation and experiments on development of shoulder height as a function of scratch normal load for PC. 129

6.3 Comparison of FEM simulation and experiments on development of scratch width as a function of scratch normal load for PC. 129

6.4 Comparison of scratch coefficient of friction (SCOF) obtained *via* experiments with development of friction calculated using FEM simulation for PC. 131

6.5 FEM simulation findings on – (a) Instantaneous and residual scratch depth; and (b) Percent elastic recovery; for PC. 131

6.6 Comparison of FEM simulation and experiments on scratch depth evolution as a function of scratch normal load for SAN. 132

6.7 Comparison of FEM simulation and experiments on shoulder height evolution as a function of scratch normal load for SAN. 133

6.8 Comparison of FEM simulation and experiments on development of scratch width as a function of scratch normal load for SAN. 133

6.9 Comparison of scratch coefficient of friction (SCOF) obtained *via* experiments with development of friction calculated using FEM simulation for SAN. 134

6.10 FEM simulation findings on – (a) Instantaneous and residual scratch depth; and (b) Percent elastic recovery calculated; for SAN. 135

A.1 Effect of meshing on - (a) Scratch depth formation at 1 m/s; (b) Scratch depth formation at 10 m/s; and (c) Instantaneous scratch depth formation at 10 m/s; during FEM simulation of PC scratch.......... 152

B.1 Effect of scratch speed on - (a) Scratch depth; and (b) Instantaneous scratch depth formation; during FEM simulation of scratch behavior of PC. 154

C.1 Effect of load gradient on scratch depth formation during FEM simulation of scratch behavior of PC. 155

LIST OF TABLES

TABLE Page

2.1 Range of material constitutive parameters used in the simulations. 22

2.2 Molecular weight information of the model systems investigated. 31

2.3 Uniaxial tension-compression properties of the model polymers. 37

2.4 True Stress-strain plots used in the FEM simulation.................................46

3.1 Constants calculated for fitting the curve in Figure 3.4 [58]. 68

4.1 Molecular weight information of the model polymers. 87

5.1 Values of linear Drucker-Prager model used in the FEM simulation. 122

5.2 Modulus and Poisson’s ratio values used in the FEM simulation. 123

5.3 Values used for calculating coefficient of adhesive friction using Equation 3.13. 124

A.1 Mesh information to study the effect of meshing. 151

CHAPTER I

INTRODUCTION

Surface quality retention in durable polymer parts has recently become one of the critical property attributes in material selection for many engineering applications, both from functionality and from aesthetics points of view. While producing desirable surface finish of a polymer has its inherent level of difficulty, the true daunting challenge lies in the preservation of surface quality over its service life. Scratch, which is a form of surface deformation process, can be considered as one of the primary causes for reduction in surface quality of polymers upon frequent usage in various applications.

For polymer applications, surface quality concerned herein can be broadly classified into surface aesthetics, structural integrity and durability [1, 2]. Surface aesthetics of the automotive exterior and interior, housing for electronic products and telecommunication devices, etc, are important due to the fact that surface scratches may reduce the product values even though their intended functionality is still generally unaffected. As for applications like food packaging, e.g., military MRE's (Meals Ready to Eat), retaining structural integrity of the packaging films is a major concern for preservation of food quality and safety. Scratches, if formed on food packaging films, can cause them to tear prematurely or compromise its barrier properties, which in turn may spoil the food inside. In coating applications, damaged surface may lead to corrosion or damage of the underlying metal or wood substrate. Therefore, coatings mechanical integrity must remain intact for as long as the expected product service life.

Such surface durability is also appreciated in the data storage industry, where scratches on hard disk and optical storage devices can cause permanent loss of data. Another important concern is from the structural point of view where scratches can act as stress concentration points, leading to reduction in load bearing capacity and ultimately result in premature fracture and failure of a structural component. Scratch is also relevant to the micro-mechanical devices and the up-and-coming nano-devices where scratch formation can easily result in a total loss of functionality in these devices at such small scales.

In view of the critical issues mentioned above, it is evident that surface scratch is of particular concern for polymeric materials. In this chapter, a brief review of polymer scratch research is given in order to highlight different aspects of polymer scratch behavior. Important factors and considerations that motivate the current study are discussed. Finally, different components of this research and their arrangements are outlined.

1.1 Overview of Polymer Scratch Research

Figure 1.1 shows the schematic of a scratching process where a rigid spherical tip traverses a polymer substrate at a particular velocity under a specified normal load. Scratch resistance is generally determined by the ability of a material to resist surface deformation due to this sliding indentation of an asperity under the application of a prescribed normal load. In view of this definition, it can be considered as a single-pass single-asperity branch of tribology as shown in Figure 1.2. This single-asperity description of scratch also distinguishes it from the multi-asperity tests used in wear analysis and allows for a rather straightforward and quantitative analysis of resistance to surface deformation.

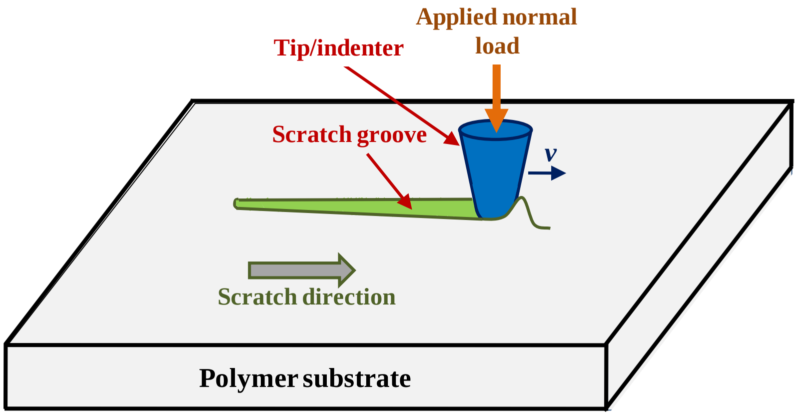

Figure 1.1. Schematic of the scratching process.

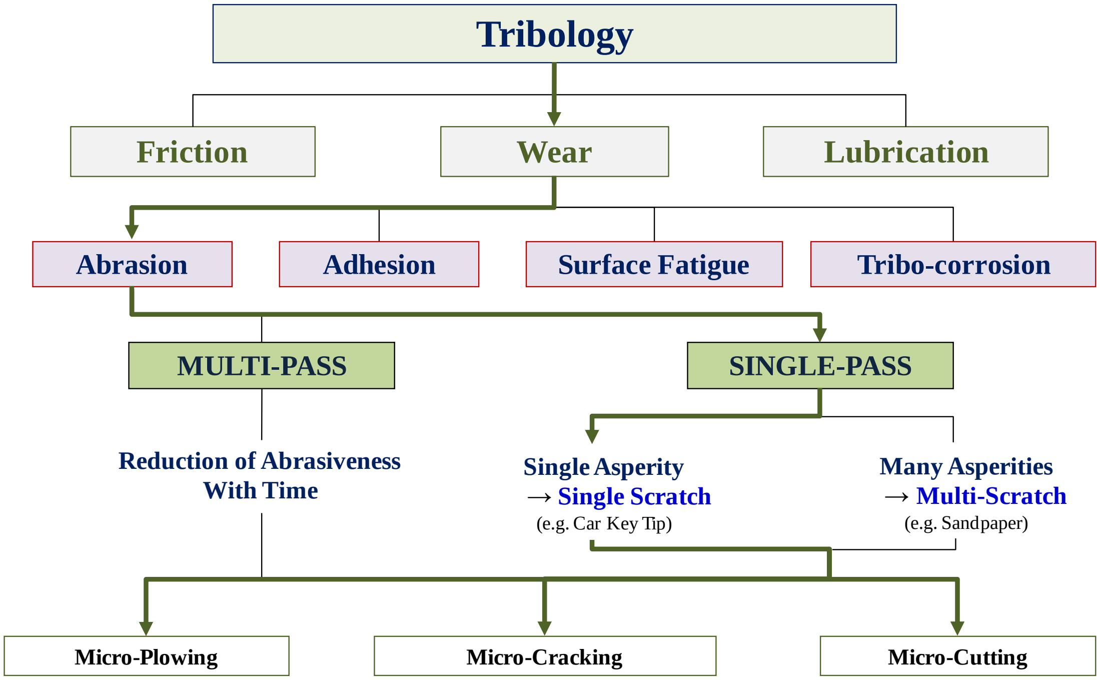

Figure 1.2. Tribology research branches.

Although retention of surface quality in polymers demands paramount attention due to its susceptibility to surface deformation and damage under low contact loads compared to metals and ceramics, research on scratch behavior of polymers achieved sufficient breakthroughs for fundamental understanding only quite recently. Prior to that, there was a lack of standardized test methodology and equipment to administer adequate scratch experiments on polymers. As a result, researchers developed their own unique testing equipment to perform scratch experiments under a specific set of conditions. There are simplistic test methods like the pencil hardness test to more sophisticated methods like the Taber test, pin-on-disc test, Ford five-finger test, single-pass pendulum sclerometer [3], to name a few, to evaluate the scratch resistance. For a compendious list of equipments and testing methods used by various researchers, one can refer to the articles [1, 4]. Furthermore, other than the variation in testing techniques, the methodologies utilized for quantitative evaluation of scratch performance also varied considerably, ranging from using subjective human observers to more objective optical instruments like high-resolution scanners, atomic force microscopy, and scanning electron microscopy. These factors unfavorably lead to a difficult situation for researchers to verify and compare experimental results published in the literature, thus inevitably hindering fundamental understanding of polymer scratch behavior. Fortunately, recent establishment of the ASTM/ISO scratch test standard [5] that employs a linearly increasing normal load applied on a 1 mm diameter spherical stainless steel tip for scratch testing has led to significant progresses in understanding the fundamental nature of polymer scratch behavior. The standardized test generates a continuous progression of deformation and damage on the scratch path, allowing for a straightforward analysis and establishment of structure-property relationship. Furthermore, the combined usage of a commercially available software package (Automatic Scratch Visualization (ASV©) software by Surface Machine Systems®) and the ASTM/ISO scratch test standard enables meaningful quantitative evaluation of the onset of scratch visibility, which is a key criterion to evaluate scratch resistance from aesthetic point of view. The corresponding physical origin(s) can also be investigated as it has been shown that the development of such deformation features is responsible for the scratch to become visible [6].

The onset and extent of different scratch-induced deformation features, such as scratch depth, shoulder height and scratch width (Figure 1.3), micro-cracks or crazes, fish-scale formation and plowing depends on a rather complex surface deformation process that involves dynamic rate dependent deformation, surface contact between the tip and the substrate, friction interaction, heat dissipation, and large-scale material and geometrical nonlinearity. Another level of complexity is added when considering polymers due to their unique material and surface properties. Since the development of scratch-induced damage features in polymers involves deformation comparable to the bulk, extensive research work has been carried out to correlate the evolution of scratch-induced deformation features with the bulk mechanical and surface properties [7-14].

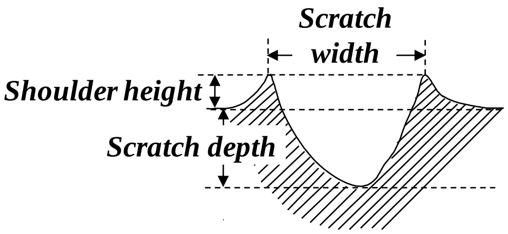

Figure 1.3. Schematic of the cross section of scratch groove.

To study the mechanics involved during the scratch process, finite element methods (FEM) [15] has been widely used by the researchers due to its capability to formulate several physical phenomena and unique material response into a single analysis. Even so, the research effort on scratch behavior using FEM remains scanty and most FEM simulations are also restricted to the study of indentation [16]. Lee et al. [17] performed FEM analysis by modeling a steel ball scratching a rotating polycarbonate (PC) disk using ABAQUS®. Although a realistic material law was adopted for the PC substrate, they over-simplified a three-dimensional (3-D) problem to a two-dimensional plane-strain problem. Bucaille et al. [18] and Subhash and Zhang [19] performed 3-D simulations of a displacement-controlled scratch-induced deformation process by employing a rigid conical indenter on elastic-perfectly-plastic and bilinear materials. Unfortunately, their 3-D FEM models did not take into account the strain softening-strain hardening nature of the polymers. Researchers in the last decade have extensively used FEM along with accompanying experiments to study the underlying mechanics involving scratch deformation of polymers following the ASTM D7027-05 scratch test [2, 7, 9, 20-22] and other testing methods [12, 23-27].

To understand the development of stress state and corresponding material response during the scratch process, FEM modeling along with the ASTM/ISO standard scratch tests was carried out by Jiang et al. [7]. The primary focus of the study was to investigate the evolution of scratch-induced deformation features in the scratch groove, i.e., development of fish-scale, crack etc., not taking into account the scratch depth and shoulder height formation along the scratch path. The stress analysis using FEM simulation showed that (Figure 1.4), as the scratch tip moves with an increasing normal load, the material in front of the tip experiences tensile stress which quickly changes into compressive and then back to tensile again. Since the development of scratch-induced deformation features depends on both stress state and material type, variation in deformation features (fish-scale, micro-crack etc.) in the scratch groove in different polymers was observed experimentally. At a low scratch normal load, the scratch penetration depth was low due to small plastic deformation. The extent of this so-called “mar” region and the development of scratch-induced damage features in the scratch groove (fish-scale, crack etc.) were observed to vary with the material type (Figure 1.5). Based on the experimental data, they developed a polymer scratch damage evolution map (Figure 1.6) to qualitatively differentiate the scratch behavior based on the respective material constitutive relation. Similar scratch deformation map, developed by other researchers [28-30] using conical indenter and constant or dead weight scratch normal load, showed evolution of different scratch-induced deformation to vary with the scratch speed due to the change in strain rate imposition.

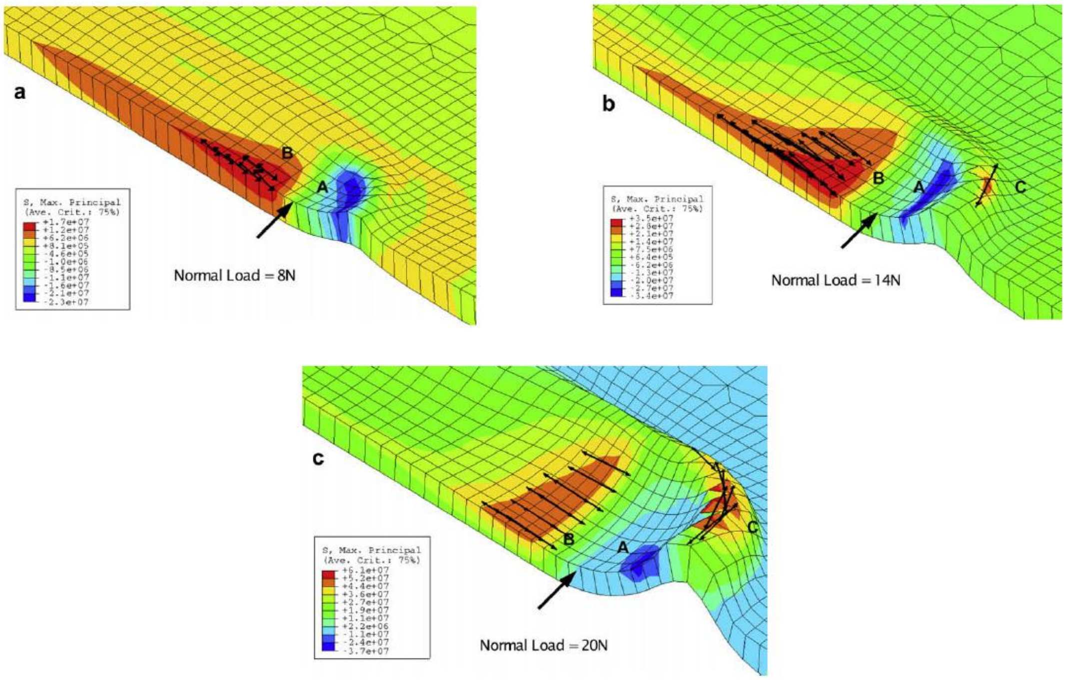

Figure 1.4. Maximum principal stress contour plot at normal loads of - (a) 8 N; (b) 14 N; (c) 20 N. (Top layer of the material elements is plotted and the scratch tip is removed for better visualization; location of the scratch tip center is indicated by the bold arrow) [7].
(Figure reprinted from Polymer, **50**, Jiang, H., Browning, R.L., Sue, H.-J., *Understanding of scratch-induced damage mechanisms in polymers*, 4056-4065, Copyright (2009), with permission from Elsevier)

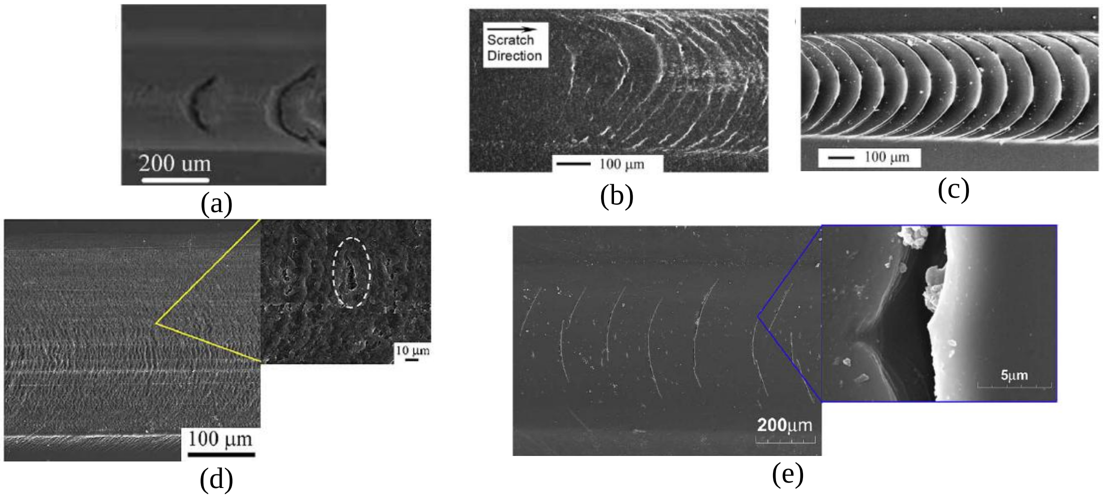

(a) (b) (c)

(d) (e)

Figure 1.5. SEM of - (a) Parabolic crack pattern in PC; (b) Onset of fish-scale formation in TPO; (c) Well developed fish-scale in TPO; (d) Pseudo fish-scale pattern mixed with crazes/voids in PS; (e) Parabolic crack pattern in Epoxy [7].
(Figure reprinted from Polymer, **50**, Jiang, H., Browning, R.L., Sue, H.-J., *Understanding of scratch-induced damage mechanisms in polymers*, 4056-4065, Copyright (2009), with permission from Elsevier)

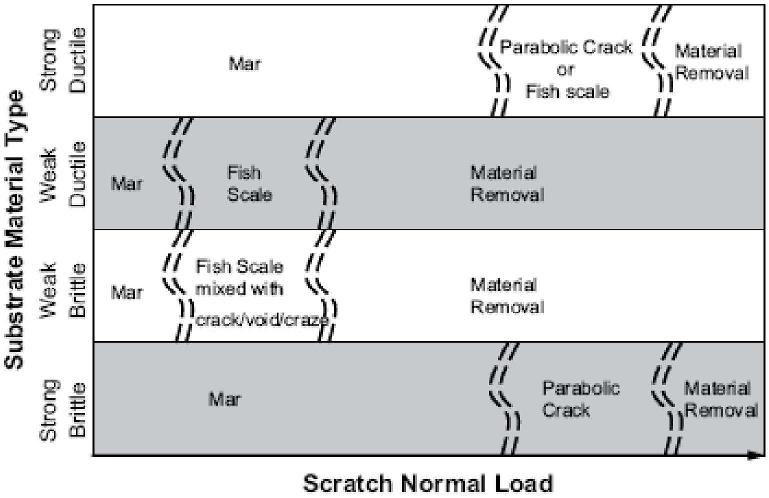

Figure 1.6. Polymer scratch damage evolution map [7].
(Figure reprinted from Polymer, **50**, Jiang, H., Browning, R.L., Sue, H.-J., *Understanding of scratch-induced damage mechanisms in polymers*, 4056-4065, Copyright (2009), with permission from Elsevier)

Parametric studies on scratch behavior of polymers using FEM have long been carried out to study the effect of various material and surface properties on scratch-induced deformation mechanisms. Simplified material models, not including mechanisms involving node or element separation during the scratch process and rate, time, temperature and pressure dependent response of polymers, have been used to gain fundamental understating on the effect of various material constitutive parameters on scratch-induced deformation. In an earlier attempt, FEM parametric study was performed [9] by employing an elastic-perfectly-plastic model to investigate the effect of material and surface properties on scratch behavior of polymers. It was concluded that the yield stress and coefficient of surface friction are the most important parameters that have significant influence on residual scratch depth of a polymer. Increasing the yield stress and/or reducing the coefficient of friction induce a shallower residual scratch depth, thus improving the scratch performance of polymers. Poisson's ratio has shown not to influence the residual scratch depth. Furthermore, Young's modulus in the range of 1.65 GPa to 4 GPa does not significantly affect the residual scratch depth, which is similar to the analytical study done by Xiang et al. [31] for 1 mm spherical tip based on the Hamilton and Goodman expression [32, 33].

Pelletier et al. [24] employed FEM for elastic-plastic contact and showed that the shape of the residual groove during scratching is related to the plastic strain field in the deformation beneath the indenter. Bucaille et al. [12] employed experimental work and FEM to study the effect of compressive strain hardening slope on piling-up phenomena during scratch. They concluded that a larger strain hardening led to greater elastic deformation, thus less plastic strain [12, 27], which improves the scratch resistance. In case of metals and metallic alloys, Bellemare et al. [34] reported a decrease in pile-up height (shoulder height) with the increase in strain hardening exponent using pure Copper and Copper/Brass alloy.

Extensive experimental work has also been carried out to study the effect of bulk mechanical and surface properties on the evolution of different scratch-induced deformation features. Hadal et al. [35] in their study showed that both higher modulus and yield strength are responsible for superior resistance to scratch deformation using different grades of ethylene-propylene copolymers and polypropylene. Unfortunately, only tensile properties were utilized in drawing their conclusions. Browning et al. [8] investigated the effect of acrylonitrile (AN) content and molecular weight (MW) on scratch behavior of styrene-acrylonitrile (SAN) random copolymers by employing

ASTM/ISO standard scratch test. The critical load for onset of scratch groove formation, periodic micro-cracking, and plowing were measured and correlated with the compressive and tensile properties of the model SAN systems. Since the compressive properties of the chosen model SAN systems were virtually the same, they concluded that increasing the AN content or MW can have a positive effect on improving the scratch resistance as it increases the tensile strength and ductility.

The effect of coefficient of friction on scratch behavior of polymers has also been investigated experimentally by employing the ASTM D7027-05 standard scratch test on four model thermoplastic olefin (TPO) systems, with and without slip agent and talc fillers [36]. Through the standard scratch test and microscopy, it was shown that a reduction in coefficient of friction delays the fish-scale formation in the TPO systems. Also, reduction in coefficient of friction induces shallower scratch depth, which corroborates the FEM findings described above [9]. Using their analytical expressions for stress field due to a circular contact region carrying a hemispherical Hertzian normal pressure and a proportionally distributed shearing traction, Hamilton and Goodman [32, 33] showed that an increase in surface friction intensifies and move the maximum yield parameter from subsurface toward the surface, and, thus, inducing greater deformation. According to the study, a maximum tensile stress also develops at the rear end of the circular contact when increasing the surface friction, which can be thought of responsible for the ring crack in brittle materials.

The experimental studies carried out to correlate mechanical properties with the evolution of various scratch-induced deformation features are deemed qualitative since the bulk mechanical properties used to draw the conclusion were measured at a strain rate much lower than the rate polymer surface would experience at the corresponding scratching speed. Most, if not all, of the FEM simulation efforts employed simplistic constitutive model in their analyses which did not take into account the strain softening-strain hardening phenomena and asymmetric tension-compression nature of polymers. Heat dissipation during scratching process; rate, time and pressure dependent behavior of polymers were also not considered. Furthermore, simplistic description of contact between the tip and the substrate was employed using the Coulomb's law of friction. As a result, most of the numerical analyses emphasize only on qualitative comparison between the FEM simulation and experimental findings. Hitherto, no known numerical analysis has been carried out to quantitatively predict the scratch behavior of polymers. Thus, although these studies provide the groundwork for fundamental understanding on the evolution of scratch-induced deformation features, a more comprehensive and realistic analysis on scratch behavior of polymers can be performed if the FEM simulation can quantitatively capture the scratch behavior in a more realistic scenario.

1.2 Research Scope

Polymers in general exhibit some distinctive features in their mechanical response, such as the strain softening-strain hardening phenomena, different behavior in tension and compression. As an illustration, Figure 1.7 shows uniaxial compressive stress-strain behaviors of polystyrene (PS), polycarbonate (PC), and polymethylmethacrylate (PMMA) [37]. For the three polymers, reduction in true stress upon yielding is observed primarily due to the inability of the polymer to sustain the imposed stress upon reorganization of molecular chains during deformation, known as strain softening. At a larger strain, the stress begins to increase with the applied strain due to the alignment of molecular chains along the stretching direction, termed as strain hardening. Thus, the strain softening-strain hardening phenomenon has to be included in the FEM simulation in order to perform an in-depth analysis on the effect of different material parameters on scratch behavior of polymers. Polymers, in general, are also known to show different mechanical responses in tension and compression. Some polymers can fail in brittle manner in tension while showing ductile behavior in compression. The yield stress of the same ductile polymer can also be different in tension and compression. As the stress field changes with the tip movement during an increasing normal load scratch test [7], it is expected that the asymmetric tension-compression behavior can greatly influence the scratch-induced deformation in polymers, and, should be included in the numerical analysis. Albeit qualitative, inclusion of these unique features in describing the constitutive behavior of polymers in FEM simulation of scratching process along with relevant experimentation would allow understanding the mechanics involved in the evolution of scratch-induced deformation features and their correlation with different material parameters in a more comprehensive fashion.

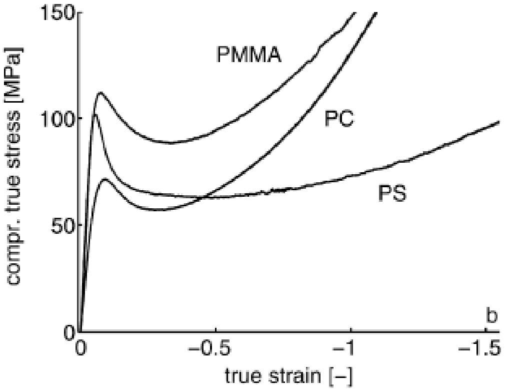

Figure 1.7. Compressive stress-strain behaviors of three glassy polymers [37].
(Figure reprinted from Polymer, **44**, van Melick, H.G.H., Govaert, L.E., Meijer, H.E.H., *On the origin of strain hardening in glassy polymers*, 2493-2502, Copyright (2003), with permission from Elsevier)

Surface friction is also known to greatly influence the scratch-induced deformation features as changes in coefficient of surface friction alter the stress state polymer substrate experiences near the surface during the scratch process. It is thus of great interest to learn how the combination of surface friction coefficient and constitutive behavior affect scratch-induced deformation.

To quantitatively predict the scratch behavior of polymers, inclusion of strain softening-strain hardening phenomena, asymmetric behavior in tension and compression in the FEM simulation is not sufficient. The rate, temperature and pressure dependent behavior, viscoelasticity will also have to be considered. Chain orientation of the polymers is also very important as it can affect the frictional properties, specifically the friction due to adhesion, and, hence, the scratch behavior of polymers [38, 39]. The contact between the tip and the polymer substrate has to be modeled properly to account for not only the coefficient of friction due to adhesion but also the friction developed due to large scale material deformation. The scratch tip geometry and surface roughness of the polymer substrate also plays an important role during the contact between the rigid tip and polymer substrate. A quantitative model for predicting scratch behavior of polymers can then be developed if all these features can be included in the FEM simulation.

The primary objective of this research is to quantitatively predict the scratch behavior of polymers using finite element method. To achieve this objective, initially, FEM parametric studies by including strain softening-strain hardening phenomena, different behavior in tension and compression with simplistic contact model will be carried out for an in-depth investigation on the effect of different material and surface properties on scratch behavior of polymers. This qualitative modeling along with relevant experimentation would further our understanding on polymer scratch behavior. Finally, attempts will be made to quantitatively predict the scratch behavior of amorphous polymers by including key characteristics of polymer mechanical behavior, appropriate contact model and adequate description for material damage in the FEM simulation.

1.3 Layout of the Dissertation

The brief review of polymer scratch research presented in this chapter covering the fundamental aspects of polymer scratch behavior provides the groundwork to perform comprehensive study on the evolution of scratch-induced deformation features in polymers. Extensive FEM parametric studies along with experimental work on model polymeric systems are performed and the results are summarized in Chapter II in order to establish correlation between different material and surface properties with scratch-induced deformation features in polymers. After establishing the correlation qualitatively, the succeeding chapters focus on developing FEM model to quantitatively predict the scratch behavior of amorphous polymers. In Chapter III, different aspects of polymer mechanical and surface behavior that needed careful consideration for quantitative modeling of scratch behavior along with corresponding literature review are presented. Chapter IV discusses the various experimental work performed on model polymers in order to characterize their rate, time and pressure dependent mechanical behavior, frictional properties and scratch behavior. Chapter V describes the methodology to include the experimental data obtained in the previous chapter into the constitutive and frictional model along with the model geometry and loading conditions employed in the FEM simulation. In Chapter VI, numerical results based on the FEM model developed in the previous chapter is compared with the experimental findings. The capability of the developed FEM model to quantitatively predict the scratch behavior of the model polymers is discussed in detail. Concluding remarks summarizing the research outcome and considerations for future research efforts are given in Chapter VII. Finally, citation of the references in this dissertation is documented.

CHAPTER II

PARAMETRIC STUDIES*

Parametric studies on scratch behavior of polymers using finite element method (FEM) allow systematic investigations on the effect of various material and surface properties on scratch-induced deformation features. The objective of this chapter is to identify key material and surface properties that significantly influence the scratch behavior of polymers. Three-dimensional FEM parametric studies along with experimental work on model polymers are conducted for that purpose.

2.1 FEM Parametric Study on Effect of Different Constitutive Parameters [10, 14]

A comprehensive FEM parametric study has been conducted on the effect of different constitutive parameters on scratch-induced deformation features in polymers based on a set of hypothetical piece-wise linear true stress-strain curves with variations in yield stress ($\boldsymbol{\sigma_y}$), strain softening slope ($\boldsymbol{s}$), strain hardening slope ($\boldsymbol{h}$), strain at stress recovery ($\boldsymbol{\varepsilon_r}$), and strain before hardening ($\boldsymbol{\varepsilon_{ES}}$). In this particular study, polymers were assumed to show similar behavior in tension and compression although they are

---

* Part of this chapter is reprinted from Wear, **270**, Hossain, M.M., Jiang, H., Sue, H.-J., *Effect of constitutive behavior on scratch visibility resistance of polymers-A finite element method parametric study*, 751-759, Copyright (2011), with permission from Elsevier.

* Part of this chapter is reprinted from Springer and the Tribology Letters, **47**, 2012, 113-122, *Effect of asymmetric constitutive behavior on scratch-induced deformation of polymers*, Hossain, M.M., Browning, R.L., Minkwitz, R., Sue, H.-J., original copyright notice is given to the publication in which the material was originally published; with kind permission from Springer Science and Business Media.

* Part of this chapter is reprinted from Polymer Engineering & Science, **53**, Hossain, M.M., Minkwitz, R., Sue, H.-J., *Minimization of surface friction effect on scratch-induced deformation in polymers*, 1405-1413, Copyright © 2012 Society of Plastics Engineers, with permission from John Wiley & Sons, Inc.

generally known to show different constitutive behavior under tension and compression. Since the focus of this study is to investigate the effect of different constitutive parameters on the development of scratch-induced deformation features in polymers, the asymmetric behavior in tension and compression and their effect is not considered here and will be addressed in a separate study discussed in Section 2.2.

2.1.1 FEM Modeling

The commercial finite element package ABAQUS® [40] (V. 6.9) was employed to perform the numerical analysis. Because of the width symmetry of the scratch path, the computational domain can be reduced by half. As shown in Figure 2.1, the dimensions of the FEM computational domain for the substrate was 20 mm × 2 mm × 2 mm with a spherical scratch tip of 1 mm diameter. Eight-node 3D linear brick elements were adopted in the modeling. Nodes on both ends were restrained in all three directions to simulate the clamping condition while nodes on the bottom surface were restrained in vertical direction to simulate the substrate resting on a rigid surface. Also, nodes on the symmetry plane were prevented from translating in the normal direction. For a tractable computational time, while maintaining a reasonably good level of accuracy, a mesh with 256 elements along the critical length (A-B) was chosen for this parametric study. Though not presented, convergence study was conducted to guarantee that this adopted mesh has a good numerical accuracy [2].

As a reasonable approximation, the scratch tip was assumed to be rigid. A piece-wise linear true stress–strain curve was used in the numerical simulation to describe the constitutive behavior of the polymer substrate. To simplify the modeling complexity, the time-dependent response of polymers was not included in this study. The FEM simulation also assumed no heat generation during the scratch process. Dynamic stress analysis with adaptive meshing was employed in the simulation to overcome excessive element distortion in the area near the scratch.

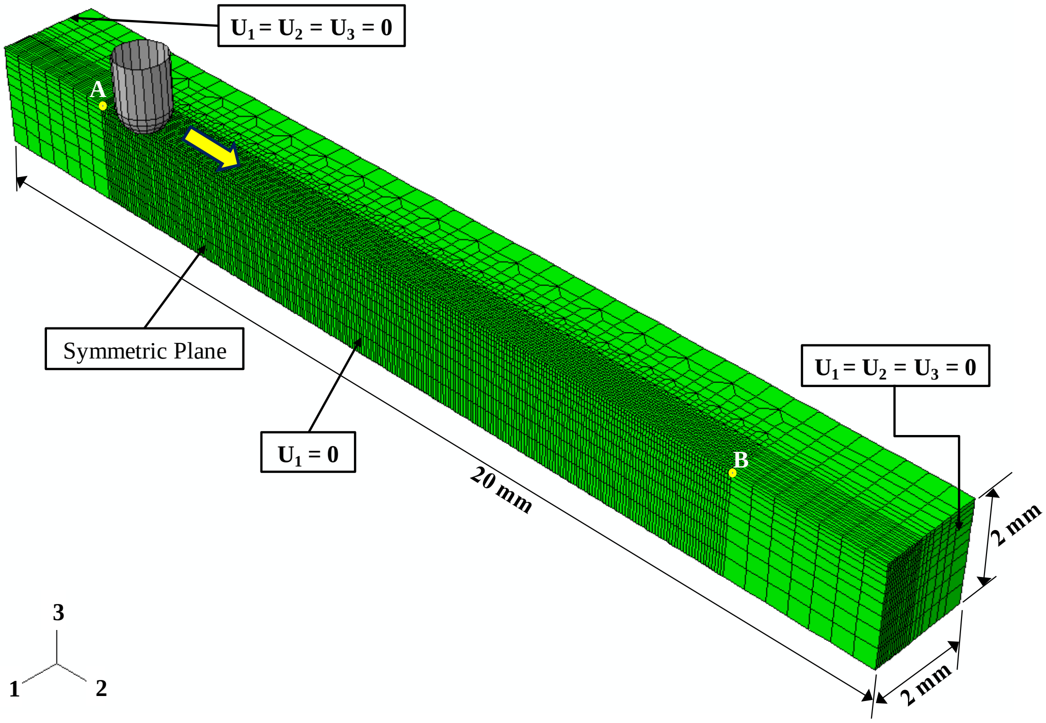

Figure 2.1. FEM simulation model.

The FEM simulation of scratch deformation is generally divided into three steps (Figure 2.2) following the ASTM/ISO standard for scratch testing [5]. The first step is the indentation process where the rigid scratch tip moves down to the substrate according to a specified loading condition. The second step is the scratch process where the tip scratches the substrate at a constant velocity with an increasing normal load. Finally, in the last step, referred to as the tip removal step, the scratch tip comes to a stop and is raised vertically upward away from the substrate to allow for the elastic recovery of the material. The tip removal step is not required if viscoelastic and viscoplastic behaviors are not considered and the scratch deformation of interest is a few mm behind the end of the scratch. Thus, in this simulation, the tip removal step was eliminated to save computational time. As the half model was used in this simulation due to symmetry condition, the normal load applied on the scratch tip during the simulation was half the actual value of the normal load of 1-30 N. Since no rate effect was considered in this FEM modeling, to save computation time of the numerical simulation, the tip moves over a length of 12 mm at a constant speed of 10 m/s was prescribed.

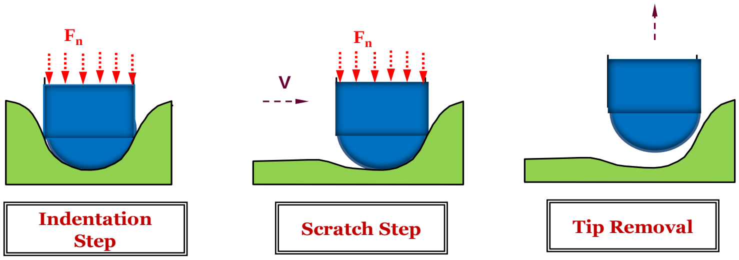

Figure 2.2. Various steps involved during a scratch process (load-controlled).

Figure 2.3 shows a schematic of the true stress-strain plot with the key parameters identified as: yield stress ($\boldsymbol{\sigma_y}$), strain softening slope ($\boldsymbol{s}$), strain hardening slope ($\boldsymbol{h}$), strain at stress recovery ($\boldsymbol{\varepsilon_r}$), and strain before hardening ($\boldsymbol{\varepsilon_{ES}}$). These parameters were varied systematically to study their effect on scratch depth and shoulder height formation during scratching of polymers.

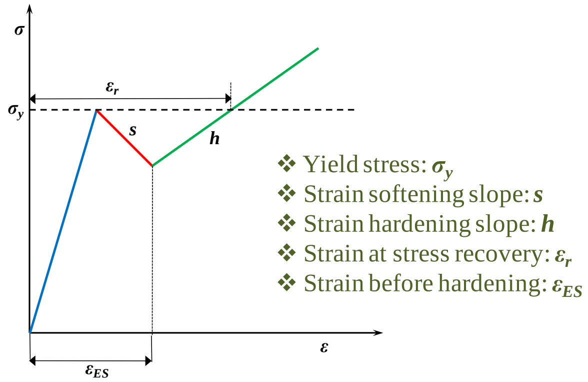

Figure 2.3. Piece-wise linear true stress-strain plot with relevant material parameters used to describe the constitutive behavior of polymer substrate in FEM simulation**.**

Table 2.1 lists the values of material constitutive parameters along with the true stress-strain plots used for four cases considered in this study. Although additional cases/scenarios were also analyzed using the FEM parametric study and results can be found elsewhere [10], these results are not included in this section to avoid redundancy. Young's modulus (***E***) was assumed to be 1.5 GPa and Poisson's ratio (***ν***) was taken to be 0.4 for all the simulation cases. Also, surface friction coefficient was assumed to be 0.3. The difference between the instantaneous scratch depth and the amount of scratch depth recovered due to elastic recovery is denoted as scratch depth throughout this dissertation, although it is termed as residual scratch depth elsewhere [9].

2.1.2 Results and Discussion

As can be seen from Table 2.1, in all cases, at least two parameters were changed simultaneously, as alteration in one parameter usually leads to changes in others, as well.

Table 2.1. Range of material constitutive parameters used in the simulations.

Case 1 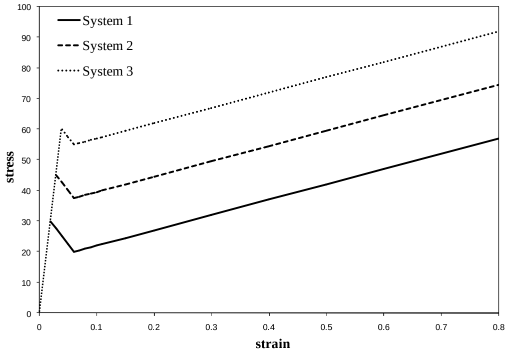 **Constants:** $\boldsymbol{s}$: -250 MPa; $\boldsymbol{h}$: 50 MPa; $\boldsymbol{\varepsilon_{ES}}$: 0.06 **Variables:** System 1 ($\boldsymbol{\sigma_y}$: 30 MPa, ε_r: 0.26) System 2 ($\boldsymbol{\sigma_y}$: 45 MPa, ε_r: 0.21) System 3 ($\boldsymbol{\sigma_y}$: 60 MPa, ε_r: 0.16)	**Case 2** 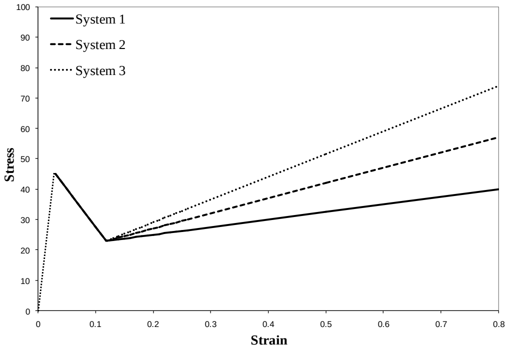 **Constants:** $\boldsymbol{\sigma_y}$: 45 MPa; $\boldsymbol{s}$: -250 MPa; $\boldsymbol{\varepsilon_{ES}}$: 0.12 **Variables:** System 1 ($\boldsymbol{h}$: 25 MPa, ε_r: 1.00) System 2 ($\boldsymbol{h}$: 50 MPa, ε_r: 0.56) System 3 ($\boldsymbol{h}$: 75 MPa, ε_r: 0.41)
Case 3 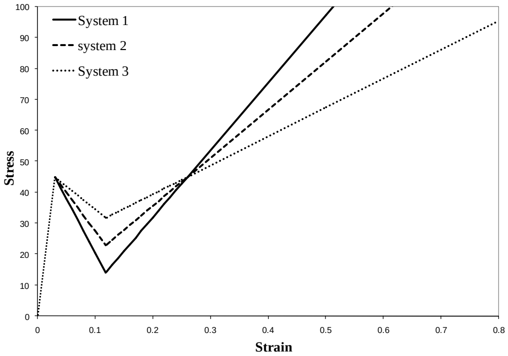 **Constants:** $\boldsymbol{\sigma_y}$: 45 MPa; $\boldsymbol{\varepsilon_{ES}}$: 0.12; ε_r: 0.26 **Variables:** System 1 ($\boldsymbol{s}$: -350 MPa, $\boldsymbol{h}$: 218.3 MPa) System 2 ($\boldsymbol{s}$: -250 MPa, $\boldsymbol{h}$: 155.9 MPa) System 3 ($\boldsymbol{s}$: -150 MPa, $\boldsymbol{h}$: 93.5 MPa)	**Case 4** 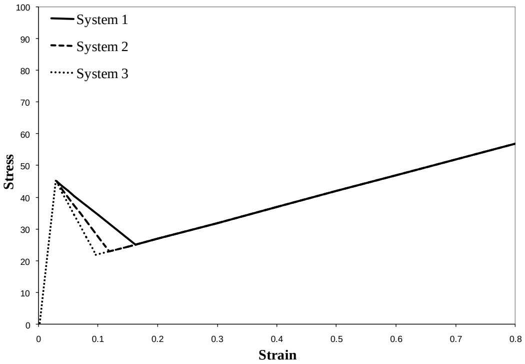 **Constants:** $\boldsymbol{\sigma_y}$: 45 MPa; $\boldsymbol{h}$: 50 MPa; ε_r: 0.56 **Variables:** System 1 ($\boldsymbol{s}$: -150 MPa, $\boldsymbol{\varepsilon_{ES}}$: 0.16) System 2 ($\boldsymbol{s}$: -250 MPa, $\boldsymbol{\varepsilon_{ES}}$: 0.12) System 3 ($\boldsymbol{s}$: -350 MPa, $\boldsymbol{\varepsilon_{ES}}$: 0.10)

2.1.2.1 Case 1: Effect of Yield Stress and Strain at Stress Recovery

According to the simulation results, higher $\boldsymbol{\sigma_y}$ induces shallower scratch depth (Figure 2.4) and lower shoulder height (Figure 2.5). Thus, polymer with higher yield stress is expected to show better scratch resistance. Similar findings were also reported by Jiang et al. [9] in their FEM simulation based on an elastic-perfectly-plastic constitutive model. It should be noted that ε_r is also inadvertently altered. Consequently, there might be a combined effect of σ_y and ε_r on scratch depth and shoulder height.

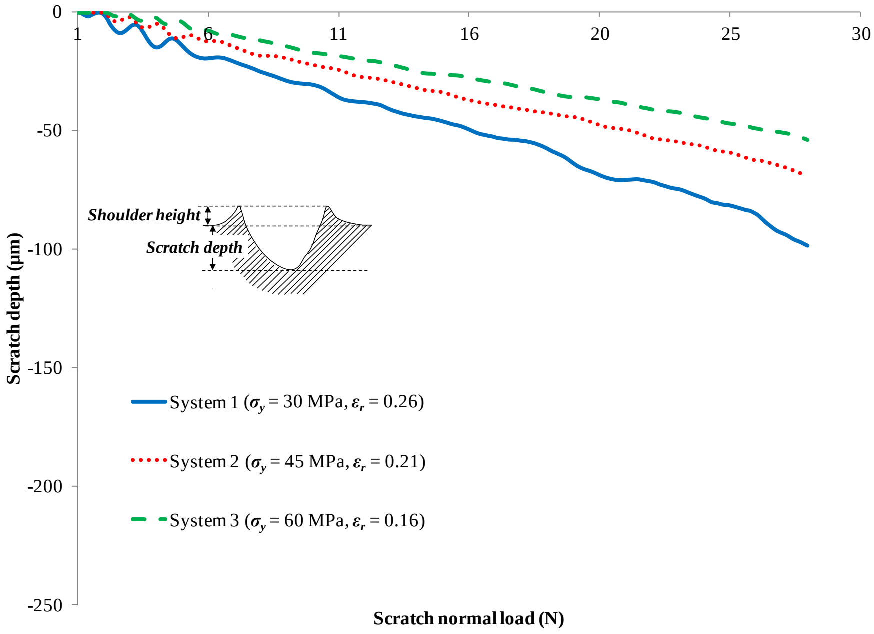

Figure 2.4. Scratch depth profile for Case 1.

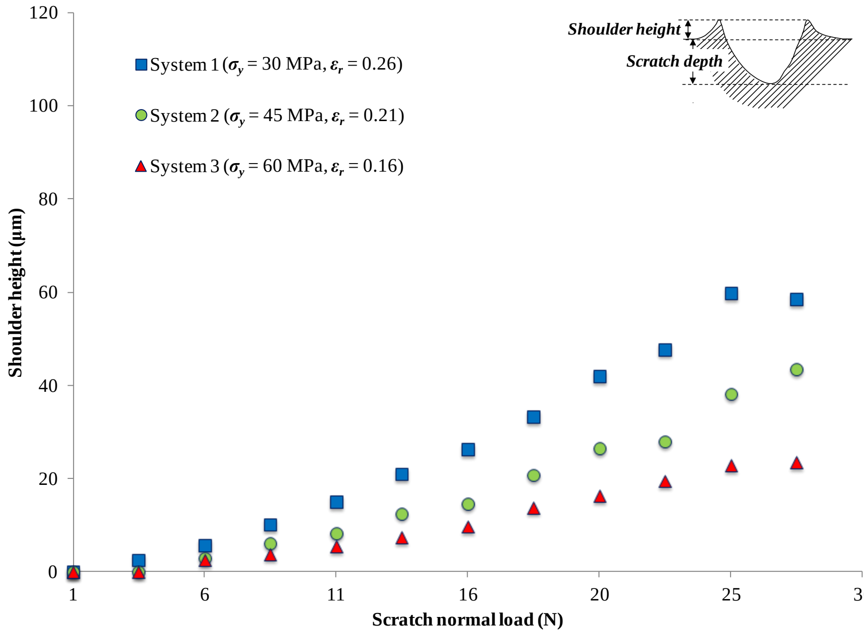

Figure 2.5. Plot of shoulder height as a function of scratch normal load for Case 1.

2.1.2.2 Case 2: Effect of Strain Hardening Slope and Strain at Stress Recovery

In case 2, when $\boldsymbol{h}$ is altered, $\boldsymbol{\varepsilon_r}$ is also affected. As shown in the FEM simulation results, a stiffer/higher $\boldsymbol{h}$ induces shallower scratch depth (Figure 2.6) and lower shoulder height (Figure 2.7). Although not shown here, the opposite is true if the polymer possesses a higher $\boldsymbol{s}$. Since $\boldsymbol{\varepsilon_r}$ is also changed if there is a variation in $\boldsymbol{h}$ or $\boldsymbol{s}$ considering all other constitutive parameters kept constant, it can also be concluded that a larger $\boldsymbol{\varepsilon_r}$ induces deeper scratch depth and higher shoulder height.

The above findings appear to be consistent with what have been reported in the literature. Bucaille et al. [12] performed scratch analysis using a micro-scratch tester in conjunction with FEM and found that a larger strain hardening coefficient led to a greater elastic recovery at the bottom and sides of the scratch groove, i.e., a reduction in scratch depth and shoulder height. Bellemare et al. [34] carried out parametric study on nano-scratch behavior of metals, and reported a decrease in pile-up height (i.e. shoulder height) with an increase in strain hardening exponent. While it is true that neither author considered the strain softening phenomena, and, thus, strain at stress recovery, along with different testing procedures, their results regarding the influence of strain hardening slope on scratch depth and shoulder height are consistent with the present findings.

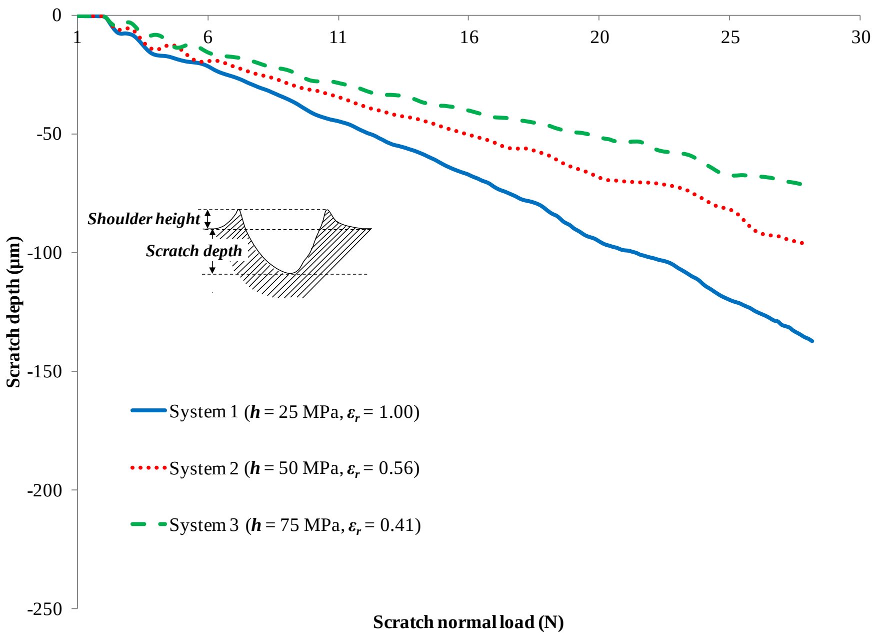

Figure 2.6. Scratch depth profile for Case 2.

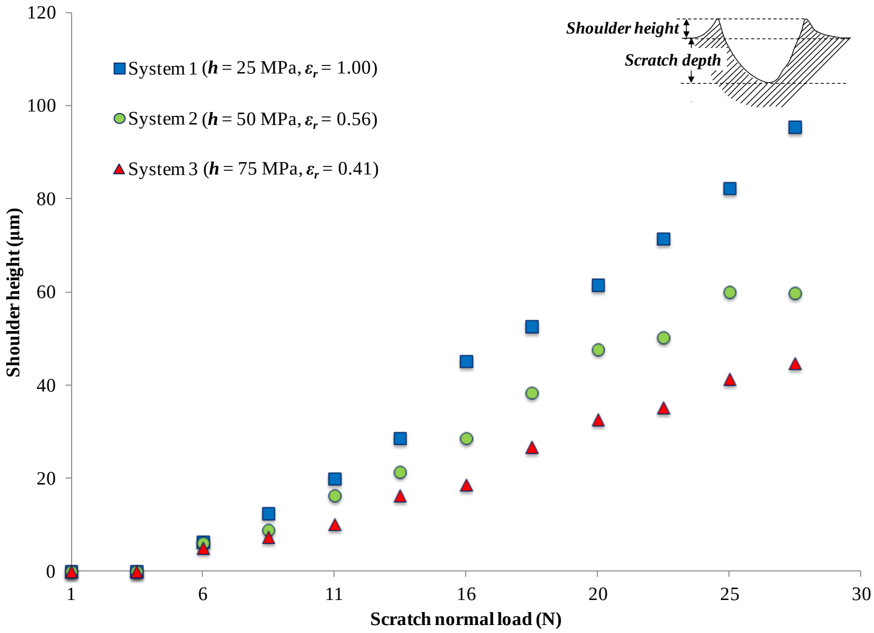

Figure 2.7. Plot of shoulder height as a function of scratch normal load for Case 2.

2.1.2.3 Case 3: Combined Effect of Strain Hardening and Strain Softening Slopes

The previous simulation results indicate that $\boldsymbol{\varepsilon_r}$ plays an important role in influencing the scratch depth and shoulder height. As the other parameters are coupled with $\boldsymbol{\varepsilon_r}$, the effect of a constant $\boldsymbol{\varepsilon_r}$ on the evolution of scratch-induced deformation features is investigated in this case. FEM simulation results indicate that when $\boldsymbol{\varepsilon_r}$ is kept constant along with $\boldsymbol{\sigma_y}$ and $\boldsymbol{\varepsilon_{ES}}$, little difference in scratch depth and shoulder height can be found among the systems (Figures 2.8-2.9). Thus, the effect of strain softening and strain hardening slopes on the development of scratch depth and shoulder height can be approximated by strain at stress recovery if all other material parameters remains the same.

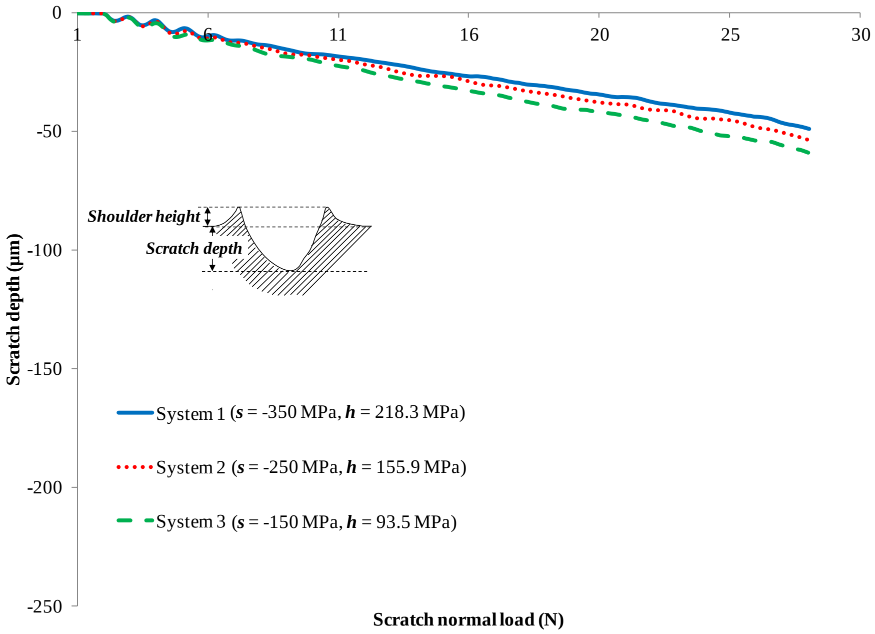

Figure 2.8. Scratch depth profile for Case 3.

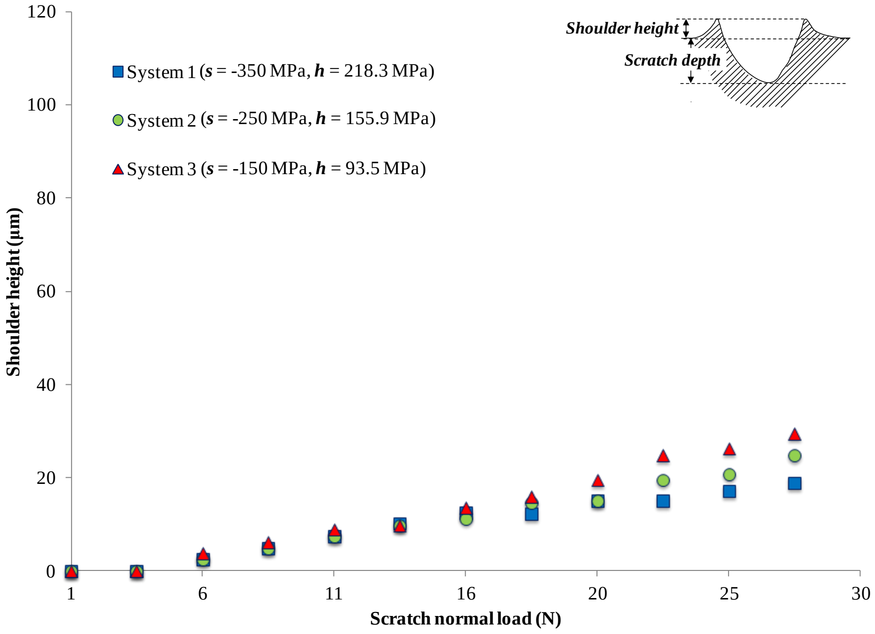

Figure 2.9. Plot of shoulder height as a function of scratch normal load for Case 3.

2.1.2.4 Case 4: Combined Effect of Strain Softening Slope and Strain before Hardening

In this case, $\boldsymbol{\varepsilon_r}$, $\boldsymbol{\sigma_y}$ and $\boldsymbol{h}$ remains constant for all three systems while $\boldsymbol{s}$ and $\boldsymbol{\varepsilon_{ES}}$ is varied. As can be seen in the FEM simulation results (Figures 2.10-2.11), all the systems show similar scratch depth and shoulder height. Thus, strain softening slope and strain before hardening have negligible effect on scratch depth and shoulder height formation.

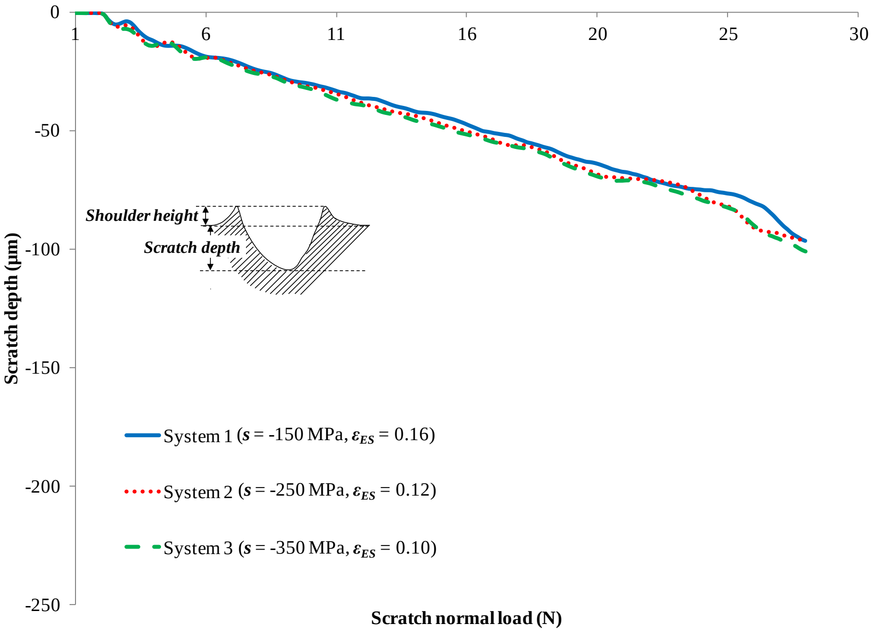

Figure 2.10. Scratch depth profile for Case 4.

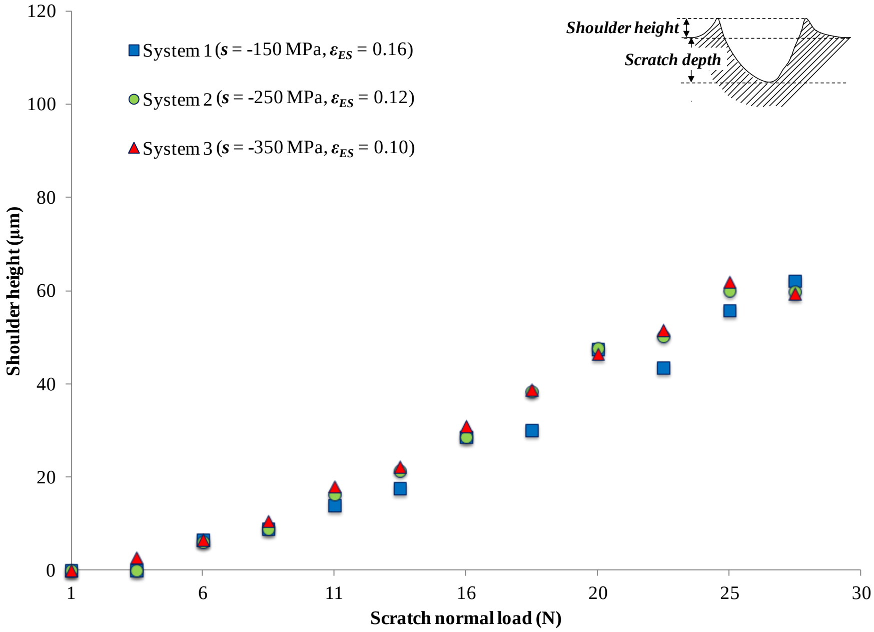

Figure 2.11. Plot of shoulder height as a function of scratch normal load for Case 4.

This FEM parametric study suggests that yield stress ($\boldsymbol{\sigma_y}$), strain at stress recovery ($\boldsymbol{\varepsilon_r}$) and strain hardening slope ($\boldsymbol{h}$) beyond the strain at stress recovery are the critical parameters that collectively represent how the constitutive behavior of a polymer affects scratch-induced deformation in polymers. According to the simulation results, polymers having the same yield stress ($\boldsymbol{\sigma_y}$), strain at stress recovery ($\boldsymbol{\varepsilon_r}$) and strain hardening slope ($\boldsymbol{h}$) beyond the strain at stress recovery are expected to show similar scratch depth and shoulder height formation along the scratch path. This study also suggests that the scratch resistance of polymers can be enhanced by altering the constitutive behavior, which, in turn, can be altered by changing the physical state or molecular structure of the polymer.

2.2 Effect of Asymmetric Constitutive Behavior [11]

In this study, attempts are made to correlate asymmetric tension-compression constitutive behavior with the scratch-induced deformation in polymers *via* FEM based on a set of hypothetical piece-wise linear true stress-strain plots. Furthermore, ASTM/ISO standard scratch tests were performed on a set of model polymers to validate the FEM findings. With the help of material science and mechanics tools, a better understanding on the relationship between scratch-induced deformation and material constitutive behavior is sought.

2.2.1 FEM Modeling

The commercial finite element package ABAQUS® [40] (V. 6.9) was employed to perform the numerical analysis. The detailed description of the FEM model used in this study is given in Section 2.1.1. The surface friction coefficient ($\boldsymbol{\mu}$), Young's modulus ($\boldsymbol{E}$), elastic Poisson's ratio ($\boldsymbol{v}$) and plastic Poisson's ratio ($\boldsymbol{v_{pl}}$) were assumed to be 0.3, 1.5 GPa, 0.4, and, 0.5, respectively.

To perform the FEM parametric study, the scratch depth and shoulder height development of a base system with equal tensile and compressive yield stress ($\boldsymbol{\sigma_{yt}}$ = 30 MPa; $\boldsymbol{\sigma_{yc}}$ = 30 MPa) is compared with two systems modified from the base system: i) ICYS - Increased Compressive Yield Stress with tensile behavior same as the base system ($\boldsymbol{\sigma_{yt}}$ = 30 MPa; $\boldsymbol{\sigma_{yc}}$ = 60 MPa) and ii) ITYS - Increased Tensile Yield Stress with compressive behavior same as the base system ($\boldsymbol{\sigma_{yt}}$ = 60 MPa; $\boldsymbol{\sigma_{yc}}$ = 30 MPa). The post-yield behavior of all the systems was assumed to be the same.

2.2.2 Experimental

2.2.2.1 Model Systems

SAN, in the form of reactor-grade random copolymers polymerized by free-radical reactions, and PC (Makrolon 2800 from Bayer MaterialScience) systems were provided by BASF SE (Ludwigshafen, Germany). The SAN model systems were provided with 19, 27 and 35 percent AN by weight, with variation in MW. Furthermore, three grades of SAN having 27 weight percent of AN were provided with variations in MW. Molecular weight information of the model systems utilized in this study was provided by BASF SE and is summarized in Table 2.2.

The resins were produced into injection-molded plaques with dimensions of 150 mm × 150 mm × 6 mm. The surface finish of the plaques was smooth (RMS Roughness = 65 nm). Upon receipt, the injection-molded plaques were annealed between two smooth glass plates at ~10 °C below their glass transition temperature ($\boldsymbol{T_g}$) in an oven for 2 hours to minimize residual surface stresses resulting from the injection molding process.

Table 2.2. Molecular weight information of the model systems investigated.

	SAN 19	**SAN 27A**	**SAN 27B**	**SAN 27C**	**SAN 35**	**PC**
Acrylontrile Content (wt%)	*19*	*27*	*27*	*27*	*35*	-
Weight Average Molecular Weight, M_W (kg/mol)	*134*	*106*	*119*	*134*	*104*	*67*
Polydispersity	*4.1*	*4.4*	*4.3*	*3.9*	*3.7*	*2.6*

2.2.2.2 Mechanical Property Characterization

Uniaxial tension and compression tests were performed following the ASTM D638 and D695 standard, respectively [41, 42]. A screw-driven MTS® Insight load frame equipped with a 30 kN capacity load cell was used for all tests. MTS® Testworks 4 was used as the software interface for data collection.

For uniaxial tensile testing, injection-molded dog-bone specimens of SAN model systems were prepared by BASF SE with a nominal thickness of 4 mm and width of 10 mm. Actual dimensions were measured with a digital micrometer caliper. A crosshead speed of 5 mm/min was used for the tensile tests and an MTS® extensometer with a gauge length of 25.4 mm was used to monitor the displacement for strain calculations. The uniaxial tension tests for PC were carried out by BASF SE.

Prismatic uniaxial compression specimens (12.7 mm × 6 mm × 6 mm) were prepared from the 6 mm thick injection molded plaques by precision-cutting using a diamond saw. After cutting the samples, the surfaces were polished using P2400 first, and, then P4000 grit silicone-carbide abrasive paper. Care was taken to ensure that all the edges were flat and square. A crosshead speed of 2.5 mm/min was chosen so that the nominal strain rate in compression was equal to that in tension. Similar to the tensile tests, an MTS® extensometer was used to monitor the displacement for strain calculations. White lithium grease was used to provide sufficient lubrication to minimize contact friction between the fixture and the sample surfaces under compression.

2.2.2.3 Scratch Tests

Scratch tests were carried out according to the conditions outlined in ASTM D7027-05/ISO 19252:08 [5] by using a progressive normal load range of 1-90 N. A constant scratch speed of 100 mm/s was used for the scratch tests with a scratch length of 100 mm. The spherical scratch tip used to conduct the tests was made of stainless steel with a diameter of 1 mm. Three scratch tests were performed on the same plaque. All tests were performed in such a way that the tip movement was the same as the melt flow direction.

2.2.2.4 Microscopic Observation

After completing the scratch tests, all the samples were stored for over 48 hours to allow for sufficient viscoelastic recovery of the scratch-induced deformation. Afterwards, a Keyence® VK9700 violet laser scanning confocal microscope (VLSCM) was used for high-resolution analysis of the scratch-induced damage mechanisms. The microscope is equipped with a 408 nm wavelength violet laser and has a height resolution of ~1 nm. The VK Analyzer software provided with the microscope was used to obtain optical images as well as topographical profiles. The tilt-correction and noise-filtering capabilities available in the software were used to process the raw images. The scratch depth, shoulder height, and RMS surface roughness at different locations on the scratch path were measured using the VK Analyzer software. The window for roughness measurement was circular with a diameter of 270 μm to correspond with the physiological resolution criterion of the human eye.

Shoulder heights and scratch depths were reported based on measurements at three adjacent locations along the scratch path corresponding to a specified scratch normal load, from which the average value and standard deviation is reported. For surface roughness, two adjacent circular areas at a specified scratch normal load on the scratch path were chosen for the measurement.

2.2.3 Results and Discussion

2.2.3.1 FEM Analysis

Figures 2.12 and 2.13 show the plots of variation in scratch depth and shoulder height as a function of scratch normal load obtained *via* FEM simulation. As shown, a higher compressive yield stress, $\boldsymbol{\sigma_{yc}}$, induces shallower scratch depth (Figure 2.12) and lower shoulder height (Figure 2.13) compared to the base system. On the other hand, system with increased tensile yield stress (ITYS) shows similar scratch depth and shoulder height compared to the base system. The scratch depth and shoulder height formed during the scratch process is due to the material being compressed in front of the scratch tip, and, then, displaced to the sides. Since the material in front of scratch tip is in compression during the scratch process, the groove formation, i.e., scratch depth and shoulder height, is strongly dependent on compressive behavior rather than tensile properties. Although not shown here, the post-yield behavior in tension also shows minimal effect on scratch depth and shoulder height formation, whereas, compressive post-yield behavior, in addition to the yield stress, affects the scratch-induced deformation.

It has been shown in the previous FEM parametric study (Section 2.1) that the yield stress, strain at stress recovery and strain hardening slope beyond the strain at stress recovery are the most important parameters that affect the scratch depth and shoulder height formation during the scratch process. The current FEM simulation work shows that these parameters in compression rather than tension strongly influence the scratch depth and shoulder height development. If these parameters in compression remain the same between ductile polymers, the scratch depth and shoulder height induced during the scratch will essentially be the same regardless of their tensile property differences. In other words, improvement in tensile properties alone has little influence on the enhancement of scratch resistance for ductile polymers. It should be noted that, if brittle fracture features, such as crazing, cracking, and chipping, occur along the scratch path, then the tensile properties could influence the scratch-induced deformation in polymers. The FEM model used in this study did not take into account crazing, cracking, or chipping during the scratch, and, thus, only relevant to ductile polymers.

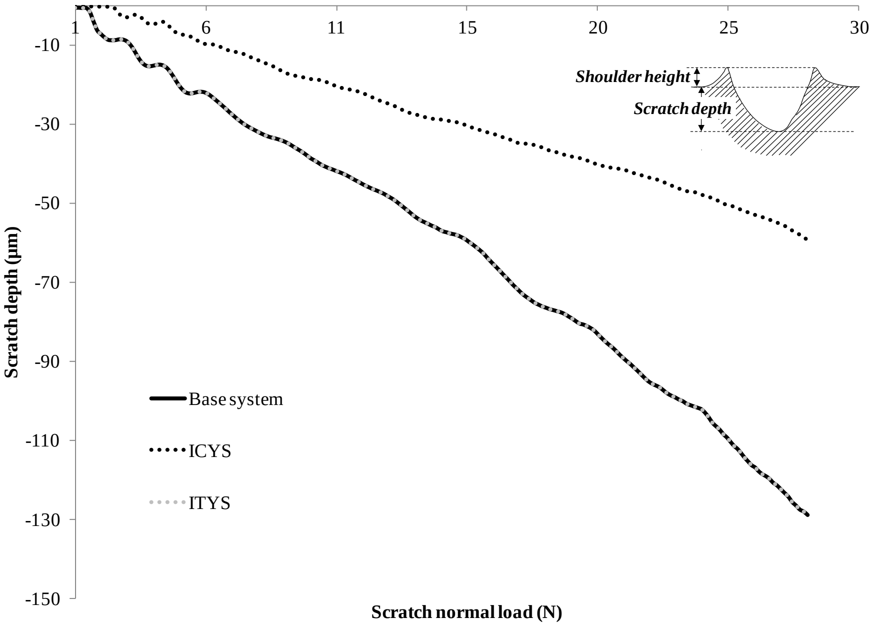

Figure 2.12. Scratch depth profile.

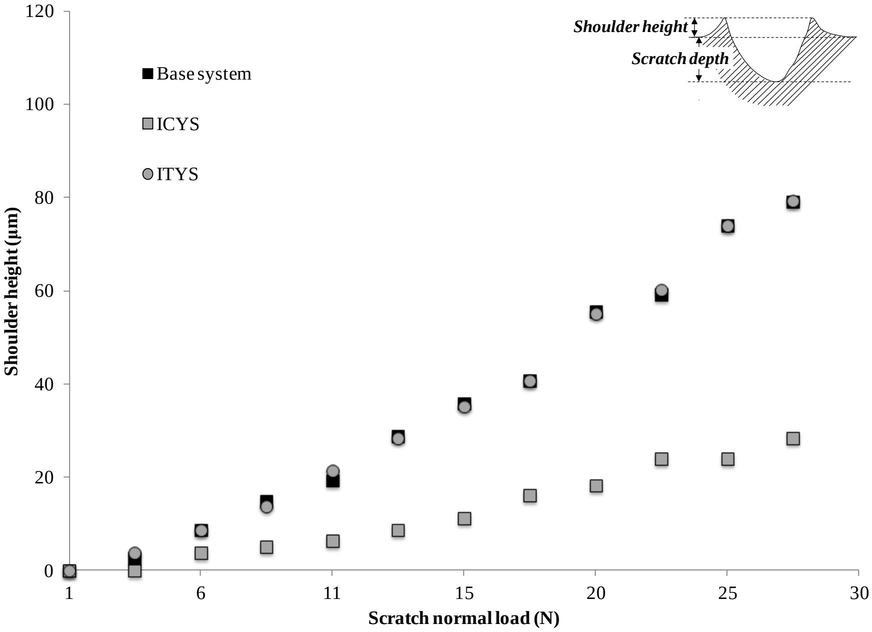

Figure 2.13. Plot of shoulder height as a function of scratch normal load.

2.2.3.2 Experimental Validation

The uniaxial tensile and compressive properties of the model systems are summarized in Table 2.3. All the model systems show ductile behavior under uniaxial compression. In uniaxial tension, all the SAN model systems show brittle behavior. Only PC shows ductile behavior, exhibiting strain softening and strain hardening phenomena under uniaxial tension.

Table 2.3. Uniaxial tension-compression properties of the model polymers.

	SAN 19	**SAN 27A**	**SAN 27B**	**SAN 27C**	**SAN 35**	**PC**
Tensile Modulus (GPa)	*3.4 ± 0.0*	*3.6 ± 0.1*	*3.7 ± 0.1*	*3.7 ± 0.1*	*3.7 ± 0.0*	*2.3 ± 0.0*
Tensile Strength (MPa)	*68.9 ± 1.5*	*63.7 ± 2.3*	*75.1 ± 3.0*	*79.0 ± 1.0*	*81.9 ± 0.7*	*65.2 ± 0.0*
Compressive Modulus (GPa)	*3.5 ± 0.1*	*3.6 ± 0.1*	*3.6 ± 0.3*	*3.5 ± 0.2*	*3.4 ± 0.2*	*2.1 ± 0.1*
Compressive Yield Strength (MPa)	*117.6 ± 0.8*	*115.2 ± 0.5*	*117.2 ± 0.4*	*117.2 ± 0.2*	*113.7 ± 1.4*	*75.3 ± 0.7*

To validate the FEM findings, scratch behavior of the model polymers are investigated. Figures 2.14 and 2.15 show the comparison of scratch depth and shoulder height as a function of scratch normal load for SAN 19, SAN 27B and SAN 27C, respectively. The compressive yield stress, modulus and post-yielding behavior of the model systems considered here are the same although their tensile strength values are different (Table 2.3). As shown, the scratch depth and shoulder height of the polymers remain essentially the same despite their differences in tensile strength. Similar finding is also observed when SAN 27A is compared with SAN 35. Thus, it can be concluded that the constitutive behavior in compression dictates the scratch depth and shoulder height formation during scratch.

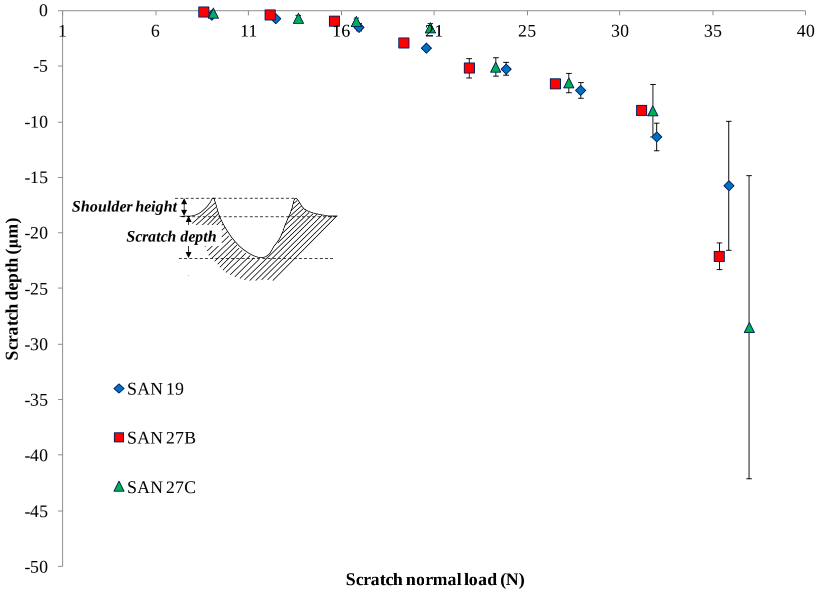

Figure 2.14. Comparison of scratch depth in SAN 19, SAN 27B and SAN 27C.

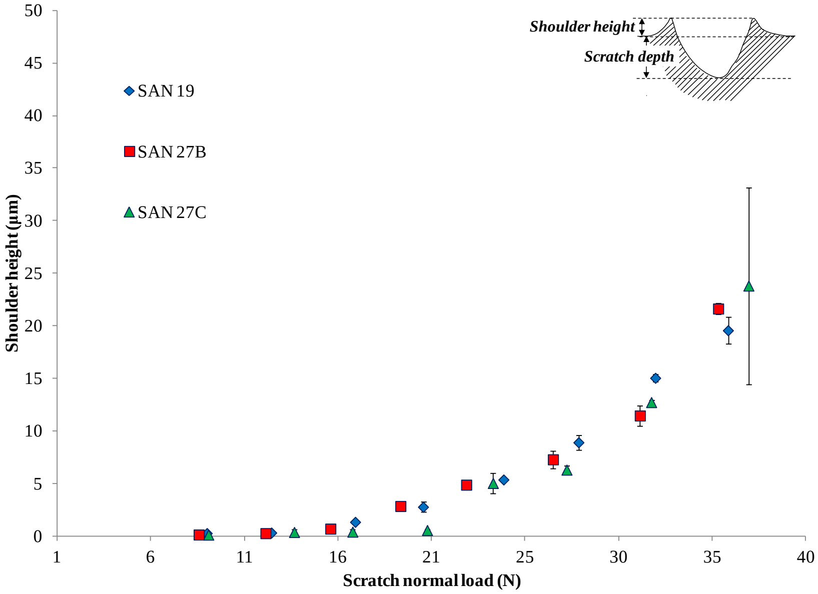

Figure 2.15. Comparison of shoulder height in SAN 19, SAN 27B and SAN 27C.

To further confirm the validity of the above claim, comparison in scratch depth and shoulder height between SAN 19 and PC is also made (Figures 2.16-2.17). Here, SAN 19 shows brittle behavior and PC shows ductile behavior under uniaxial tension. The yield stresses and post-yield behaviors under compression for the two systems are different (Table 2.3). As shown, due to lower compressive yield stress, deeper scratch depth and higher shoulder height is induced in PC compared to SAN 19. Similar result is also obtained when SAN 27A is compared with PC. It should be noted that even though the moduli of SAN 19 and SAN 27A systems are quite different from PC, previous studies [9, 31] have indicated that modulus exerts minimal effect on scratch depth if it is greater than 1.65 GPa under the ASTM scratch testing conditions. Hence, it can be concluded that the compressive yielding and post-yielding behavior strongly influence the scratch depth and shoulder height formed during the scratch process. Tensile behavior has little or no influence on shoulder height and scratch depth formation.

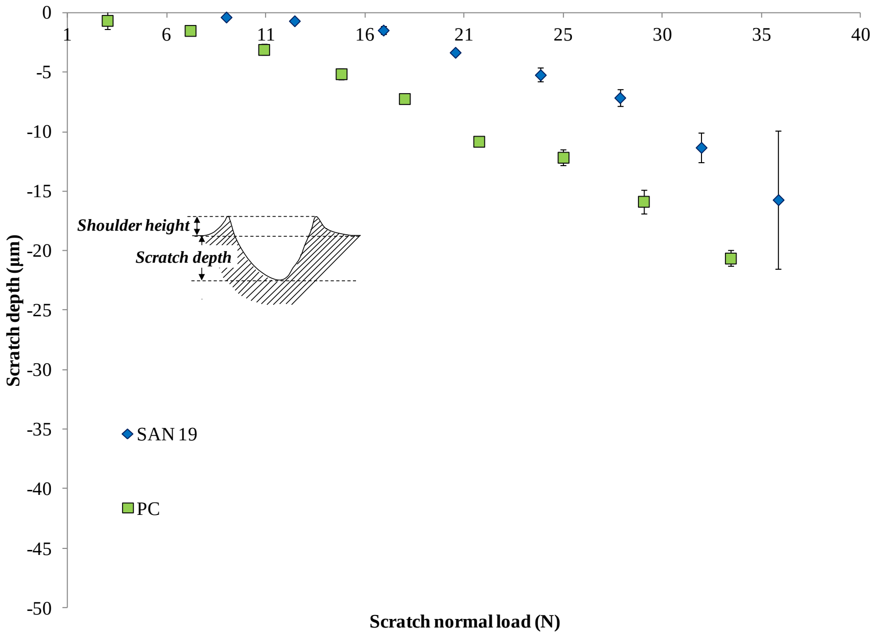

Figure 2.16. Comparison of scratch depth in SAN 19 and PC.

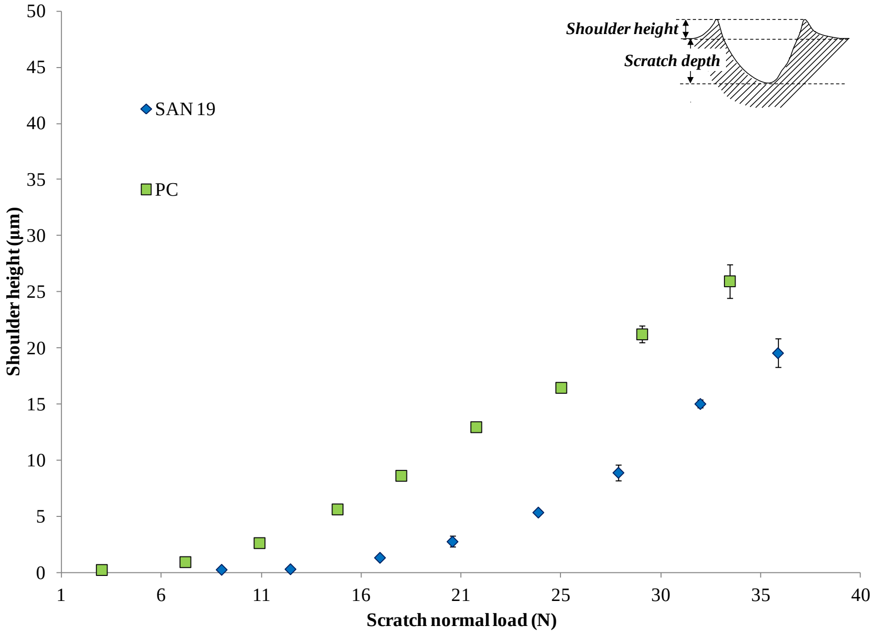

Figure 2.17. Comparison of shoulder height in SAN 19 and PC.

Finally, correlation between surface roughness inside the scratch groove and material constitutive behavior is sought using the model polymer systems. The increase in surface roughness along the scratch path with the increase in scratch normal load can be attributed to the formation of fish-scale, micro-cracks, parabolic cracks, chipping, etc., during the scratch process. Therefore, tensile constitutive behavior may become important. Hamilton and Goodman [32, 33] showed that the maximum tensile stress developed primarily on the rear edge of a circular scratch tip. Jiang et al. [7] also reported the same in their FEM simulation work. The exerted maximum tensile stress component is responsible for the formation of various kinds of damage features in brittle material. Thus, tensile behavior is important in this context as it influences the surface roughness inside the scratch groove. However, the formation of fish-scale involves stick-slip phenomena where both compressive and tensile constitutive behavior can play important roles in influencing the deformation mechanism [7]. It should be noted that, as the stick-slip/fish-scale and crack formation were not included in the model, the FEM simulation was unable to correlate surface roughness with the constitutive behavior directly. Thus, direct surface roughness measurement was carried out along the scratch path to correlate with the constitutive behavior of model polymers.

Figure 2.18 shows the micrographs of the scratch groove obtained *via* VLSCM for SAN and PC model systems to elucidate the deformation mechanisms responsible for the increase in surface roughness inside the scratch groove. The VLSCM micrographs for plowing/material removal during scratch are not shown to avoid redundancy. Formation of periodic micro-cracks/crazes can be seen in all the SAN systems (Figure

2.18a). Browning et al. [8] studied the relation between onset of micro-crack formation and tensile strength on the same model SAN systems using the ASTM scratch testing standard. According to their experimental work, since all the model SAN systems have similar compressive behavior, the onset of micro-crack formation can be correlated with the tensile strength. As increase in surface roughness inside the scratch groove is primarily due to the micro-cracks/crazes formed in case of SAN, similar relation between increase in surface roughness and tensile strength is found in this study.

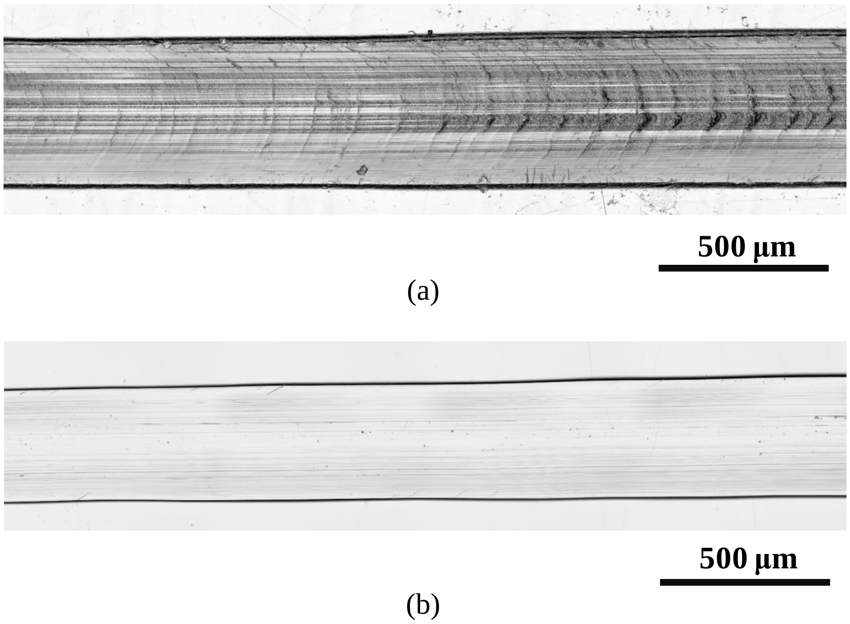

Figure 2.18. Micrographs of the scratch groove obtained *via* VLSCM in (a) SAN; (b) PC model systems.

Figure 2.19 compares the surface roughness for SAN 19 and PC. As shown, the surface roughness of SAN 19 increases abruptly at higher scratch normal load when compared to that of PC. Similar behavior is also observed when comparing other SAN systems with PC. Since the SAN systems are brittle and PC is ductile in tension, the variation in surface roughness at higher scratch normal load can be attributed to the difference in tensile ductility in the model systems as only smooth groove formation is observed in the scratch groove for PC (Figure 2.18b).

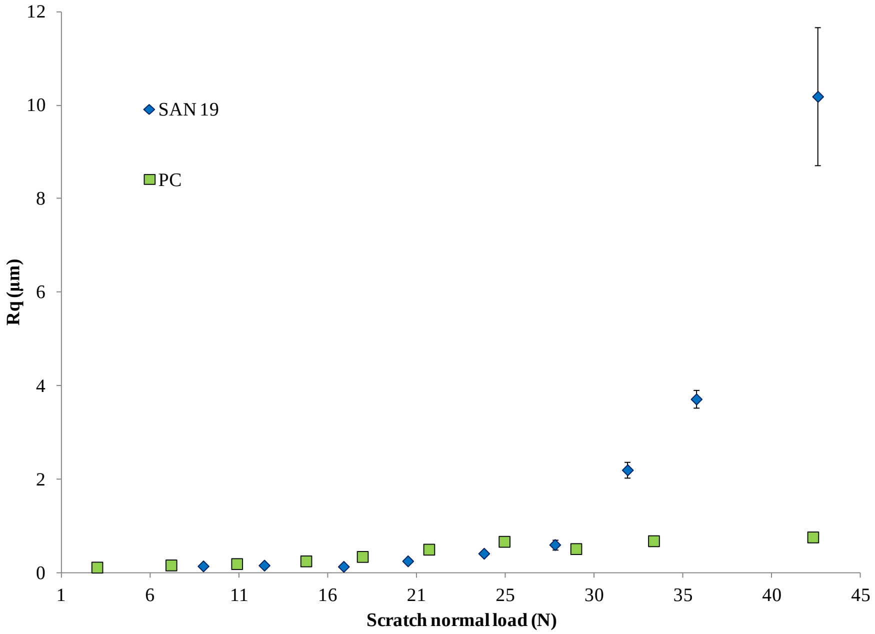

Figure 2.19. Comparison of surface roughness in SAN 19 and PC.

It should be noted that the standard deviation values for shoulder height, scratch depth, and surface roughness generally increase with increasing scratch normal load. As the scratch normal load increases, the material experiences more severe deformation and damage, especially when damage such as fish-scale and micro-cracking begin to form along the scratch path. When such damage forms, the scratch tip may no longer be able to maintain firm contact with the substrate surface. Skipping and jumping occur, causing increased standard deviation. Usually, standard deviation for shoulder heights, scratch depth, and surface roughness is rather low for ductile samples where the scratch-induced deformation is smooth and gradual, such as PC. On the other hand, for brittle samples, such as SAN, their standard deviations will dramatically increase once micro-cracking/crazing begin to form.

The FEM simulation findings and experimental results in this study show that the shoulder height and scratch depth formation are strongly influenced by compressive yielding and post-yield constitutive parameters. Tensile behavior has little influence on the shoulder height and scratch depth formation except for surface roughness along the scratch path. Thus, altering the compressive behavior, i.e., yield stress, strain at stress recovery and strain hardening slope beyond the strain at stress recovery in compression, is expected to alter the scratch resistance of ductile polymers. Again, the present findings suggest that the scratch-induced deformation, such as shoulder height and scratch depth formation, and surface roughness inside the scratch groove can be correlated with the constitutive behavior of polymers.

2.3 Influence of Surface Friction [13]

In this part of study, efforts are made to analyze the effect of surface friction on scratch-induced deformation and investigate how this effect can be altered by varying the polymer yield and post-yield behaviors, namely, yield stress, strain hardening slope and strain at stress recovery. The parameters chosen are consistent with the previous FEM parametric study (Section 2.1), where it has been shown that these constitutive parameters strongly influence the scratch-induced deformation mechanisms. The FEM simulation was carried out based on a set of hypothetical piece-wise linear true stress-strain plots taking into account the strain softening-strain hardening phenomena showing similar behavior in tension and compression. In addition to the FEM simulation, scratch tests on a set of model polymers were conducted according to the ASTM/ISO scratch test standard to validate the FEM findings.

2.3.1 FEM Modeling

A commercial finite element package ABAQUS® [40] (V. 6.9) was employed to perform the numerical analysis. The detailed description of the FEM model used in this study is provided in Section 2.1.1.

Table 2.4 shows the simulated piece-wise linear true stress-strain plots along with the material parameters used to describe the constitutive behavior of polymer substrate in the FEM parametric study. Four different categories of systems were considered with variations in yield stress and strain hardening slope; namely, Low Yield Stress System (LYSS), High Yield Stress System (HYSS), Low Strain Hardening System (LSHS) and High Strain Hardening System (HSHS). It should be noted that the strain at stress recovery is also changed when strain hardening slope is varied between the systems (e.g., LSHS *vs.* HSHS). The coefficient of adhesive friction, μ, based on the Coulomb's friction law, was varied from 0-0.9 with an increment of 0.3 in these systems to investigate the effect of surface friction on scratch depth and shoulder height along the scratch path.

Table 2.4. True Stress-strain plots used in the FEM simulation.

True stress-strain plot	Parameters
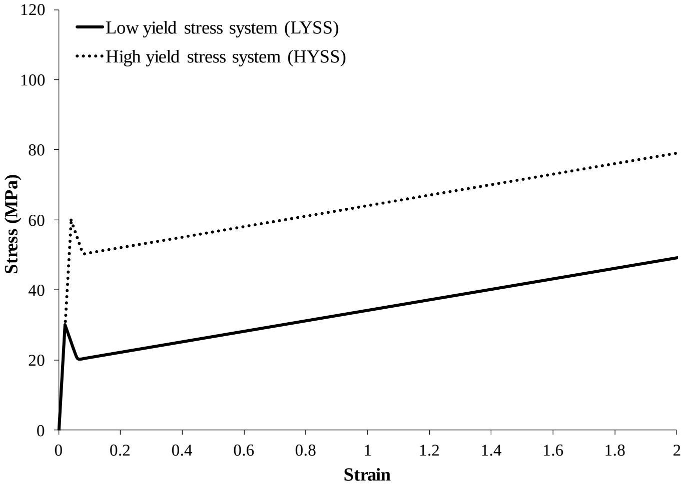	**Constants** Young's modulus, $\boldsymbol{E}$ = 1.5 GPa Poisson's ratio, $\boldsymbol{\nu}$ = 0.4 Strain softening slope, $\boldsymbol{s}$ = -250 MPa Strain hardening slope, $\boldsymbol{h}$ = 15 MPa Strain at stress recovery, $\boldsymbol{\varepsilon_r}$ = 0.73 **Variables** **LYSS:** Yield stress, $\boldsymbol{\sigma_y}$ = 30 MPa Strain before hardening, $\boldsymbol{\varepsilon_{ES}}$ = 0.06 **HYSS:** Yield stress, $\boldsymbol{\sigma_y}$ = 60 MPa Strain before hardening, $\boldsymbol{\varepsilon_{ES}}$ = 0.08
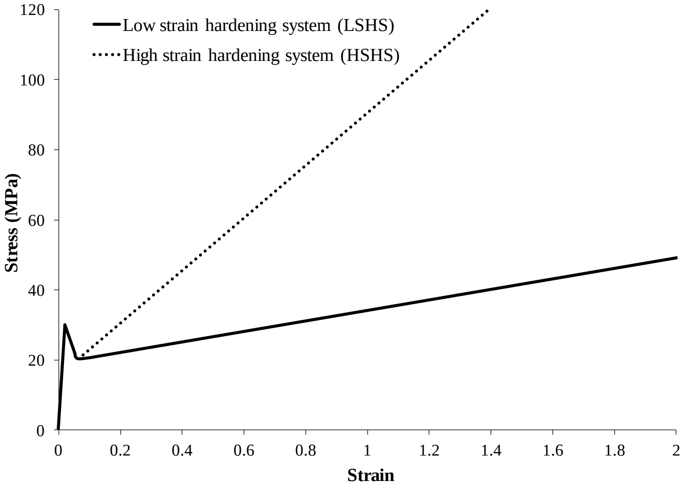	**Constants** Young's modulus, $\boldsymbol{E}$ = 1.5 GPa Yield stress, $\boldsymbol{\sigma_y}$ = 30 MPa Poisson's ratio, $\boldsymbol{\nu}$ = 0.4 Strain softening slope, $\boldsymbol{s}$ = -250 MPa Strain before hardening, $\boldsymbol{\varepsilon_{ES}}$ = 0.06 **Variables** **LSHS:** Strain hardening slope, $\boldsymbol{h}$ = 15 MPa Strain at stress recovery, $\boldsymbol{\varepsilon_r}$ = 0.73 **HSHS:** Strain hardening slope, $\boldsymbol{h}$ = 75 MPa Strain at stress recovery, $\boldsymbol{\varepsilon_r}$ = 0.19

2.3.2 Experimental

2.3.2.1 Model Systems

SAN, containing 19 percent AN by weight, and PC systems, discussed in Section 2.2.2.1 were chosen for this study. Molecular weight information of the model systems are provided in Table 2.2. The surface finish of the plaques was smooth (RMS Roughness = 37 nm).

2.3.2.2 Mechanical Property Characterization

Since the formation of scratch depth and shoulder height along the scratch path is greatly influenced by compressive behavior rather than tensile (Section 2.2), only uniaxial compression test was performed according to the procedure described in Section 2.2.2.2.

2.3.2.3 Scratch Tests

Scratch tests were carried out according to ASTM D7027-05/ISO 19252:08 [5] standard by employing a linearly progressive normal load of 1-70 N. A constant scratch speed of 100 mm/s was used for the scratch tests with a scratch length of 100 mm. A stainless steel spherical scratch tip of 1 mm diameter was used to conduct the tests. To reduce surface friction in SAN and PC, Teflon spray was applied on the surface of the plaques before conducting the scratch tests. Three scratch tests were performed on the same plaque. All tests were performed in such a way that the tip movement was in the direction of melt flow.

2.3.2.4 Measurement of surface friction coefficient

To determine the coefficient of surface friction, μ at the interface between the model systems (Neat and Teflon coated) and scratch tip, a flat smooth stainless steel tip with 10 mm × 10 mm square area was employed. The flat tip was installed on the scratch machine and tests were conducted under 5 N constant normal load for a distance of 40 mm at a velocity of 100 mm/s. Three tests were conducted for each system to obtain an average value of μ. This procedure to measure the coefficient of surface friction is comparable with the method described in literature [43].

2.3.2.5 Microscopic Observation

After completing the scratch tests, all the samples were stored for over 48 hours to allow for sufficient viscoelastic recovery of the scratch-induced deformation. Afterwards, the samples coated with Teflon were sonicated for 2 hours in a water bath, and, then, dried using compressed air. A Keyence® VK9700 violet laser scanning confocal microscope (VLSCM) was used for high-resolution analysis of the scratch-induced damage mechanisms according to the procedure described in Section 2.2.2.4.

2.3.3 Results and Discussion

2.3.3.1 FEM Analysis

Figures 2.20 and 2.21 show the plots of variation in scratch depth and shoulder height as a function of scratch normal load obtained *via* FEM simulation for low yield stress system (LYSS) and high yield stress system (HYSS), with and without friction, respectively. As shown, higher $\boldsymbol{\sigma_y}$ induces shallower scratch depth and lower shoulder height, which is consistent with the previous findings (Section 2.1). Increase in surface friction intensifies the stress field, thus induces deeper scratch depth and higher shoulder height in both systems. This finding is also consistent with the literature [9, 24].

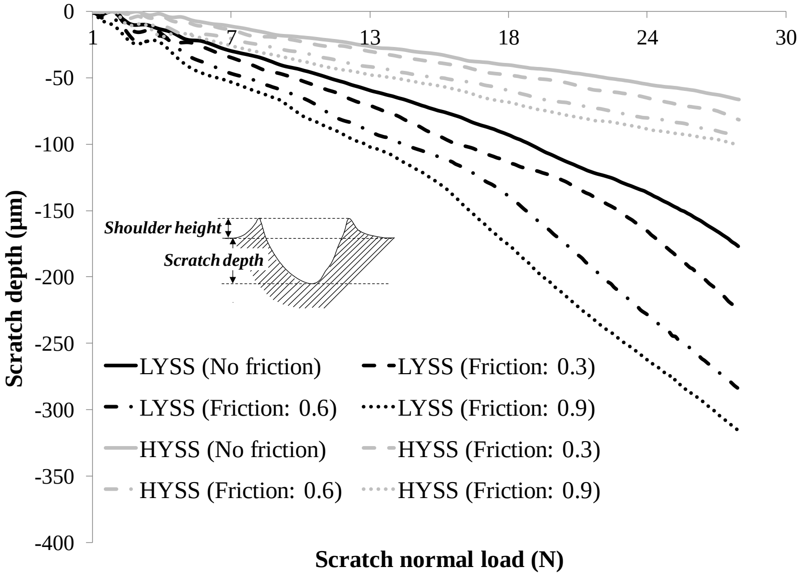

Figure 2.20. LYSS *vs.* HYSS scratch depth profiles obtained *via* FEM simulation.

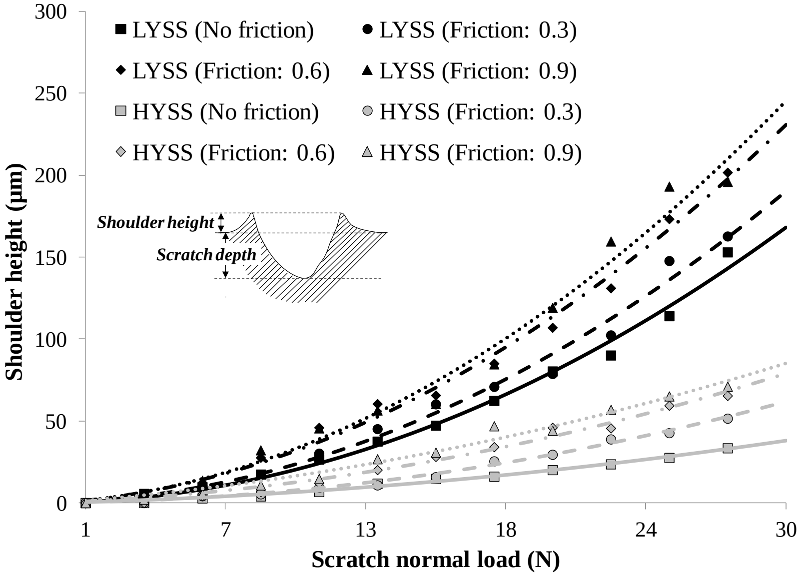

Figure 2.21. Plots of shoulder height of LYSS and HYSS as a function of scratch normal load obtained *via* FEM simulation.

To further elucidate the effect of surface friction on scratch-induced deformation, initial portion of the scratch depth is shown in Figure 2.22. As shown, the onset of groove formation is delayed in HYSS (Point A) compared to that of LYSS (Point B) without friction. Since σ_y is higher in HYSS, the plastic strain is lesser and elastic recovery is higher in HYSS compared to that of LYSS. As a result, the onset of groove formation is delayed in HYSS compared to LYSS. Since surface friction intensifies the stress gradient and magnitude, for a frictional value of 0.9, the onset of groove formation occurs at a lower load than that of the frictionless case for both systems. For HYSS, the onset of groove formation is near point B, whereas for LYSS the onset occurs at the very beginning of scratch. Thus, increase in surface friction can significantly affect the onset of groove formation.

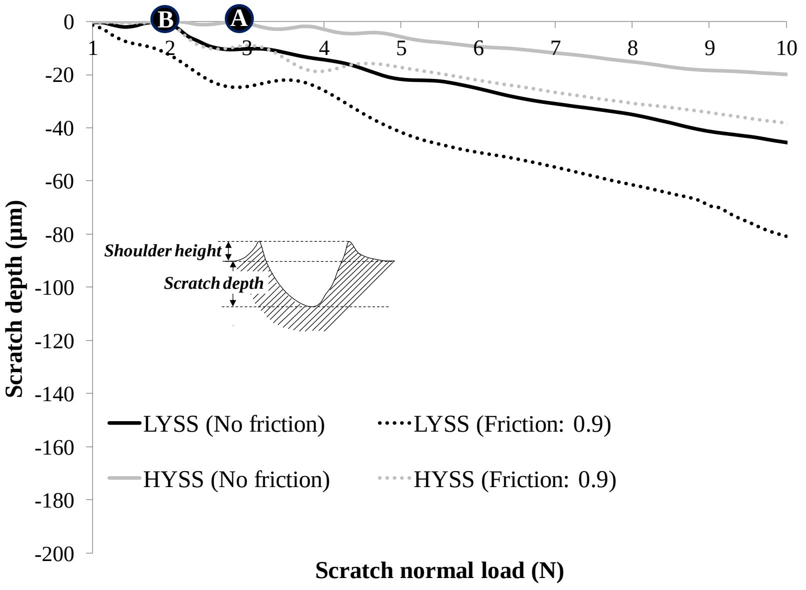

Figure 2.22. Effect of yield stress and surface friction on onset of groove formation obtained *via* FEM simulation.

To further our understanding, scratch depth profiles for cases with friction are divided by the corresponding no friction case within the scratch normal load of 8-24 N. This normalization allows for direct assessment of relative frictional effect on scratch depth. Since scratch depth denotes the nodal displacement along the scratch path whereas shoulder height is measured at different points on the scratch, it is more practical to evaluate the relative frictional effect based on scratch depth as it provides continuous data points throughout the scratch path for analysis. As shown in Figure 2.23, an increase in surface friction increases the relative frictional effect in both HYSS and LYSS systems. At lower coefficient of friction (μ = 0.3, 0.6), the relative frictional effect is similar for both high and low yield stress systems. When the frictional value is 0.9, the relative frictional effect is higher at the beginning in HYSS, which diminishes later on and falls below LYSS. This high relative frictional effect in HYSS at the beginning of scratch can be attributed to the high elastic recovery and low plastic strain in no friction case compared to that of high friction case. As the plastic strain continues to increase with the scratch normal load in no friction case, the relative frictional effect begins to diminish as the scratch progresses. This phenomenon is more pronounced in HYSS compared to LYSS. The relative frictional effect is higher in LYSS compared to that of HYSS towards the end of the scratch. Thus, yield stress has no significant impact on frictional effect along the scratch depth.

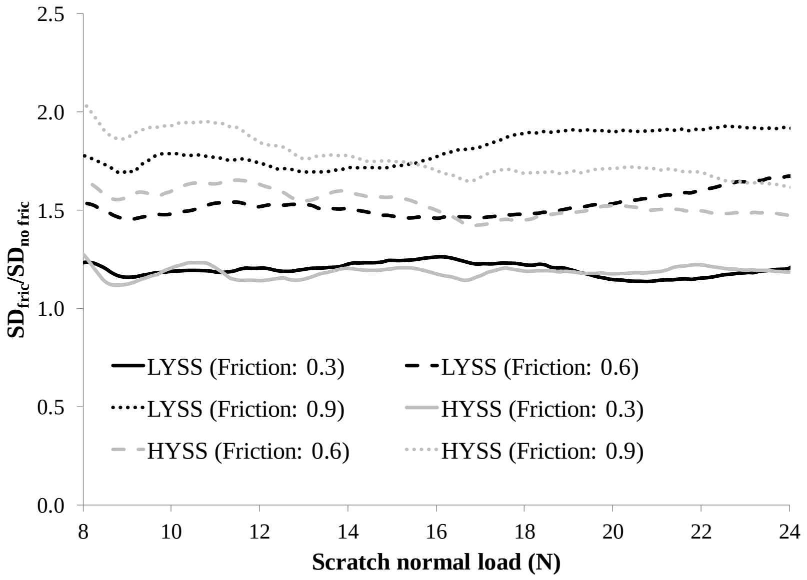

Figure 2.23. Relative frictional effect on scratch depth in LYSS and HYSS obtained *via* FEM simulation.

Figures 2.24 and 2.25 show the scratch depth profile and variation in shoulder height for low strain hardening system (LSHS) and high strain hardening system (HSHS), with and without friction, respectively. As shown, both smaller strain at stress recovery and higher strain hardening slope beyond the strain at stress recovery induce shallower scratch depth and lower shoulder height, which is again consistent with the previous findings (Section 2.1). Similar to the previous case, increase in surface friction induces deeper scratch depth and higher shoulder height in both systems.

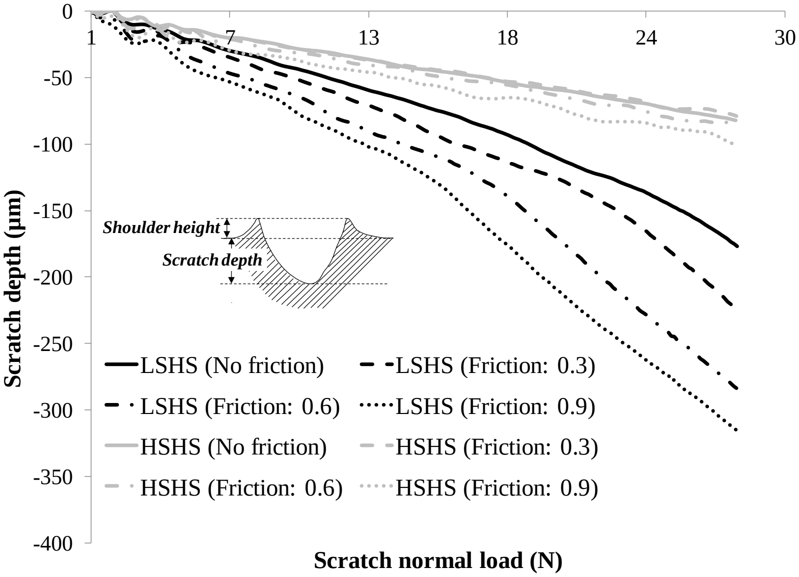

Figure 2.24. LSHS *vs.* HSHS scratch depth profiles obtained *via* FEM simulation.

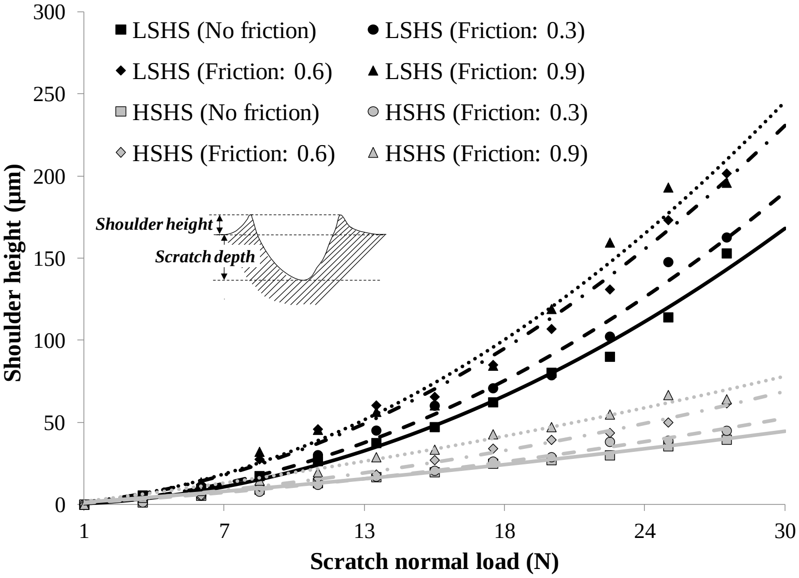

Figure 2.25. Plots of shoulder height of LSHS and HSHS as a function of scratch normal load obtained *via* FEM simulation.

Similar to the previous case, initial portion of the scratch depth is shown in Figure 2.26. As shown, the onset of groove formation is similar for both systems without friction (point A). This similarity in onset of groove formation can be attributed to the similarities in their Young's modulus and yield stress. Thus, post-yield behavior has no influence on onset of groove formation. Analogous to the previous case, increase in coefficient of surface friction induces an earlier onset of groove formation. For a frictional value of 0.9, the onset of groove formation is at the beginning of scratch for both systems (point B). Again, it shows that surface friction significantly affects the onset of groove formation.

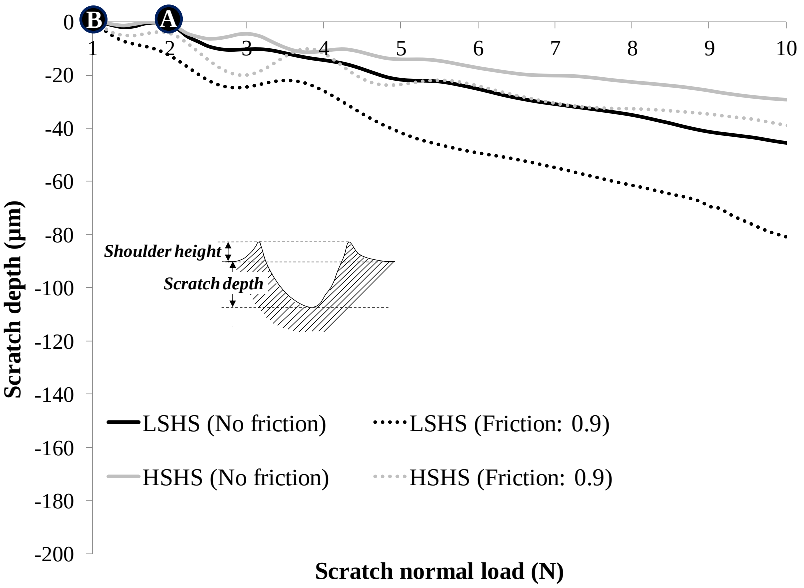

Figure 2.26. Effect of strain hardening slope and surface friction on onset of groove formation obtained *via* FEM simulation.

As described earlier, the scratch depth profiles with friction cases are divided by the corresponding no friction case within the scratch normal load of 8-24 N. As shown in Figure 2.27, increase in surface friction increases the relative frictional effect in both systems. Overall, the relative frictional effect is more severe in LSHS compared to HSHS. It is interesting to note that there is almost no relative frictional effect on scratch depth when coefficient of friction value is 0.3 for the HSHS. This reduction in relative frictional effect on scratch depth in the HSHS can be attributed to its higher resistance against further plastic deformation. Thus, although surface friction intensifies the stress gradient and magnitude for both systems, the relative frictional effect is less in HSHS.

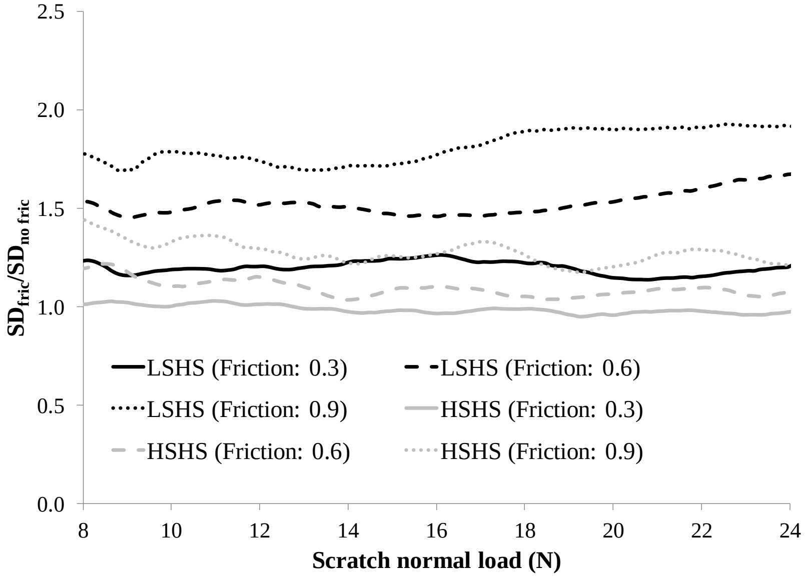

Figure 2.27. Relative frictional effect on scratch depth in LSHS and HSHS obtained *via* FEM simulation.

According to the FEM simulation results, effect of surface friction on scratch-induced deformation can be reduced by increasing the strain hardening slope. Increase in yield stress has no significant influence on relative frictional effect on scratch depth. It should be noted that, increasing the strain hardening slope will reduce the strain at stress recovery if all the other material parameters kept the same.

2.3.3.2 Experimental Validation

Figure 2.28 shows the stress-strain plot in uniaxial compression for SAN and PC model systems. As shown, the compressive yield stress of SAN is higher compared to that of PC. On the other hand, PC has higher strain hardening slope (lower strain at stress recovery) than SAN. Figure 2.29 shows the coefficient of friction (COF, μ) measurement for both SAN and PC, with and without Teflon sprayed. As shown, the system with Teflon sprayed on the surface (denoted as LCF) has lower coefficient of friction compared to their respective neat counterpart (denoted as HCF). The reduction in COF, μ is ~ 51% in SAN and ~ 48% in PC. Thus, similar reduction in COF for both systems is achieved. It should be noted that, the scratch coefficient of friction (SCOF), which is the ratio of tangential force to normal load during the scratch process, of both systems follow the same trend.

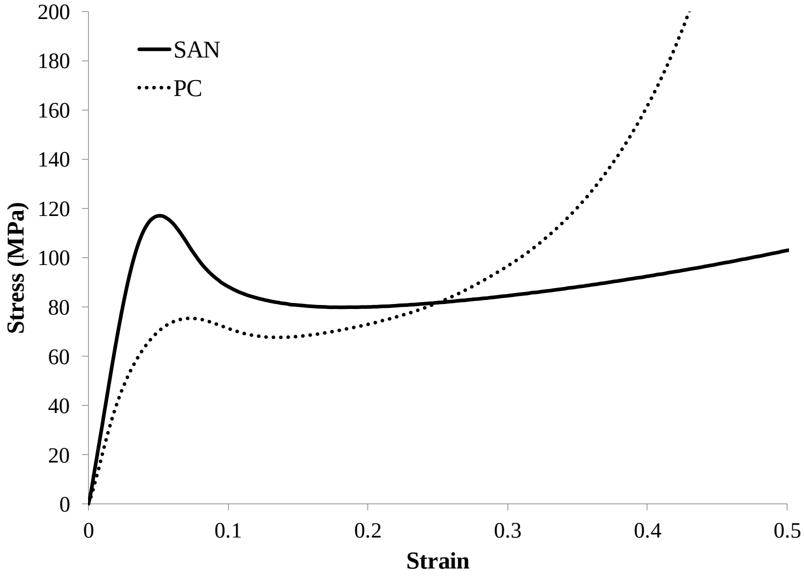

Figure 2.28. Uniaxial compression stress-strain curve for SAN and PC model systems.

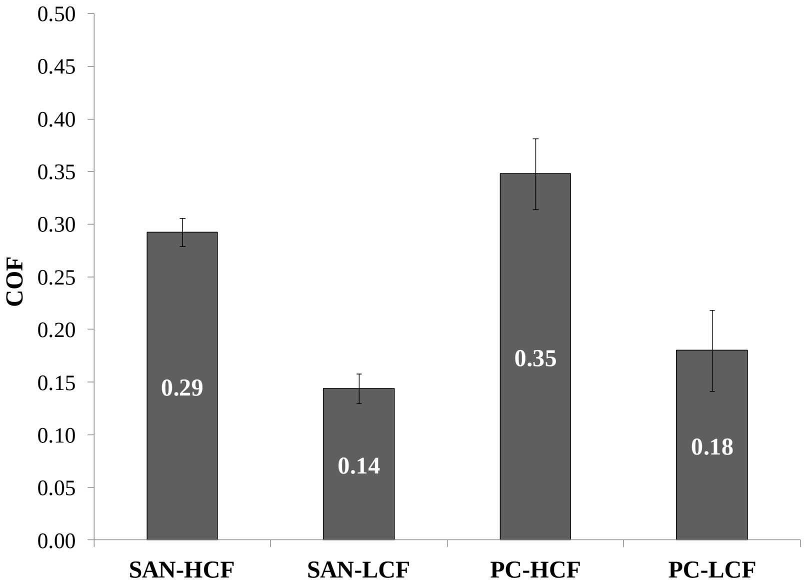

Figure 2.29. Coefficient of friction measured for the model polymers.

Figure 2.30 shows the plot of onset of groove formation for the model polymers obtained *via* VLSCM. The detailed procedure for the measurement of onset of groove formation can be found elsewhere [8]. The onset load for groove formation in SAN-HCF system is higher compared to PC-HCF system. As the compressive yield stress of SAN is higher than that of PC (Figure 2.28), the onset of groove formation is delayed in SAN, which matches well with the FEM findings. Also, for both systems, reduction in COF delays the onset of groove formation, which is also consistent with the FEM findings. Although not shown, onset of plowing in SAN is also delayed with the reduction in coefficient of surface friction.

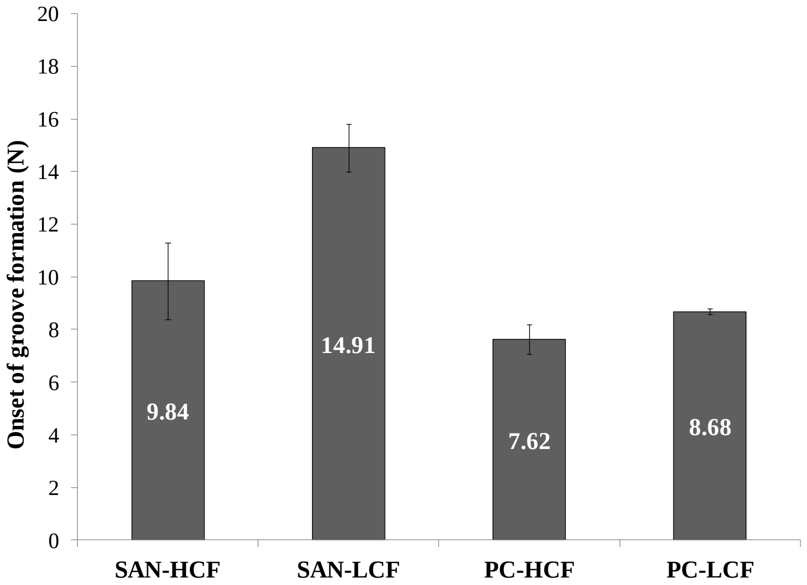

Figure 2.30. Onset load for scratch groove formation in the model systems.

Figures 2.31 and 2.32 show the plots of scratch depth and shoulder height as a function of scratch normal load obtained *via* VLSCM following the procedure described in Section 2.3.2.5, respectively. Since SAN has higher compressive yield stress compared to PC, it has lower shoulder height and shallower scratch depth, which is consistent with the previous findings (Section 2.1 and 2.2). Reduction in COF induces shallower scratch depth and lower shoulder height for both systems, but the percent reduction in scratch-induced deformation in SAN (dotted lines) is much higher compared to that of PC (solid lines). Although the reduction in COF for both systems is comparable, SAN shows higher relative frictional effect compared to that of PC. Since, according to the FEM simulation, increase in yield stress has negligible influence on relative frictional effect up to a COF value of 0.6, this higher relative frictional effect in SAN can be attributed to the lower strain hardening slope compared to that of PC.

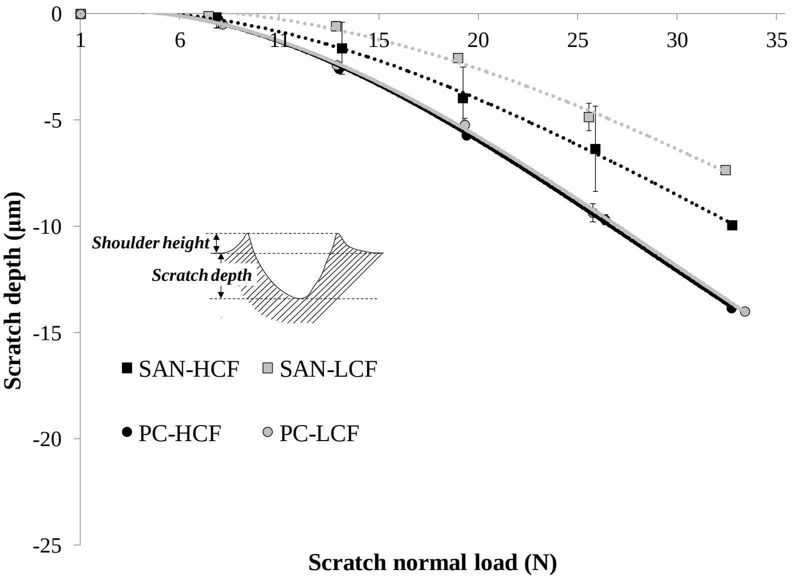

Figure 2.31. Comparison of scratch depth between SAN and PC. Dotted trend-line denotes SAN and solid trend-line denotes PC.

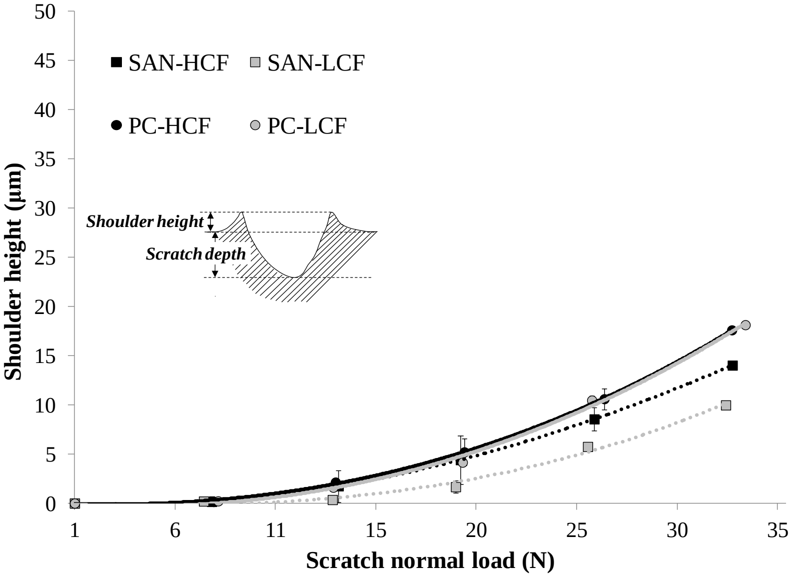

Figure 2.32. Comparison of shoulder height between SAN and PC. Dotted trend-line denotes SAN and solid trend-line denotes PC.

Although not presented here, Polypropylene (PP), with and without slip agent, which has lower yield stress and strain hardening slope compared to that of PC, also showed higher relative frictional effect compared to PC. Since fish-scales form at a very low load in PP, there were not enough consistent data points for scratch depth measurement. However, the shoulder height data were more reliable and showed higher relative frictional effect in PP compared to that of PC. Scratch tests at 1 mm/s scratching speed also showed similar behavior.

According to the FEM simulation and experimental results, the onset of groove formation is primarily affected by yield stress, which is influenced by coefficient of surface friction. Up to a certain value of COF, increase in yield stress alone has no significant influence on relative frictional effect on scratch-induced deformation. According to the study, relative frictional effect on scratch-induced deformation can be reduced by increasing the strain hardening slope. It should be noted that, strain at stress recovery is reduced when the strain hardening slope increases with all other parameters kept the same. The present findings suggest that the effect of COF on scratch-induced deformation can be altered by modifying the constitutive behavior of polymers. More importantly, if the strain hardening slope is high enough, there is no need to use slip agent or other surface treatment process to reduce the friction as the frictional effect on scratch-induced deformation would be minimal.

In all the experimental work discussed in this chapter, uniaxial compressive and tensile behavior of the model polymers at a constant crosshead speed has been used to draw the conclusion, which may be oversimplified as the stress state during scratch is generally multiaxial. Furthermore, polymer mechanical behavior is known to be rate sensitive and the uniaxial compressive and tensile tests were performed at rates much lower than that the polymer surface would experience during the scratch process. Thus, it was assumed that the difference in mechanical properties for the model polymers obtained at lower strain rates is maintained at higher strain rates, which may also be too simplistic. With respect to the FEM simulations discussed in this chapter; rate, time, temperature and pressure dependent behavior of polymers was not considered in addition to the simplistic contact model adopted to describe the contact between the rigid tip and polymer substrate. As a result, the comparisons made in this chapter are qualitative in nature. Nevertheless, the study provides useful insights on the effect of various material and surface properties on the evolution of scratch-induced deformation features in polymers.

CHAPTER III

FACTORS CONSIDERED FOR QUANTITATIVE MODELING

For quantitative modeling of polymer scratch behavior, some aspects of polymer mechanical behavior, such as, rate, time, temperature and pressure dependent yielding need careful consideration in addition to the strain softening-strain hardening phenomena and asymmetric tensile-compressive behavior discussed earlier. Furthermore, the contact between rigid spherical tip and polymer substrate has to be modeled appropriately. This chapter discusses the aforementioned and other aspects needed consideration for modeling polymer scratch behavior quantitatively with corresponding literature review.

3.1 Rate Dependent Mechanical Behavior of Amorphous Polymers

During the scratch process, the effective strain rate on or near the surface can be approximated by [28]:

$$\dot{\varepsilon} = \frac{v}{w} \tag{3.1}$$

Where, $\dot{\varepsilon}$ is the effective strain rate, v is the scratch speed and w is the scratch width. For a scratch speed of 100 mm/s and spherical scratch tip of 1 mm diameter, recommended by the ASTM standard [5], the effective strain rate on or near the surface can reach to a minimum of 100 /s to a maximum of thousands /s. The standard tension and compression tests generally conducted at a strain rate of ~ 10^{-2}-10^{-3} /s, which is decades lower than the strain rate experienced on or near the surface during scratch. Thus, to quantitatively predict the scratch behavior of polymers using FEM, high strain rate mechanical behavior of polymers is needed. It should be noted that, since the strain rate varies from one position to another during the scratch process, the mechanical behavior only at a particular strain rate is not sufficient for modeling the scratch behavior. The constitutive behavior of the polymer substrate from low strain rate to high strain rate is needed along with an interpolation scheme so that the material behavior can be simulated based on the strain rate it experienced.

The stress-strain response shown in Figure 3.1 is strongly dependent on the strain rate. Generally, the yield stress, which denotes the beginning of plastic flow, increases with strain rate. As shown in Figure 3.1, the yield stress of PC increases appreciably with strain rate. However, the post-yield behavior remains unchanged with the increase in strain rates. Similar post-yield behavior with increase in strain rate is also reported by others [44-47].

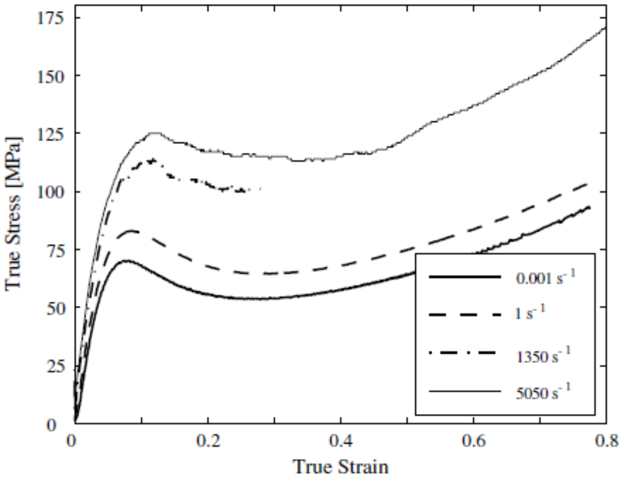

Figure 3.1. True compressive stress-strain curves of PC at various strain rates [48].
(Figure reprinted from International Journal of Solids and Structures, **43**, Mulliken, A.D., Boyce, M.C., *Mechanics of the rate dependent elastic–plastic deformation of glassy polymers from low to high strain rates*, 1331-1356, Copyright (2006), with permission from Elsevier)

To describe the rate dependent yield or flow stress for glassy, amorphous polymers, several theoretical models are available. Although based on specific molecular mechanisms involved in the yield behavior of polymers, Robertson [49] and Argon [50] models found limited success, specifically from low to moderate strain rate, to describe the rate dependent plasticity in amorphous polymers. Perhaps the most widely-accepted model to describe the rate dependent plasticity in amorphous polymers is the Ree-Eyring model [51], a modification of the original Eyring model [52]. Eyring's theory, which can be considered as a "transition state" theory, makes no assumption on specific molecular motion behind the rate dependent plasticity of amorphous polymers [53]. The Ree-Eyring model for rate dependent plasticity of amorphous polymers matches quite well with the experimental data from low to high strain rates and temperatures (Figure 3.2). The major difference among the Ree-Eyring, Robertson, and Argon models is their prediction of yield behavior at high strain rates (Figure 3.3). As can be seen in both Figures 3.2 and 3.3, the ability to change the slope at an intermediate strain rate distinguishes the Ree-Eyring model from the other two models, and, thus, allows better prediction of the rate dependent plasticity in amorphous polymers from moderate to high strain rates.

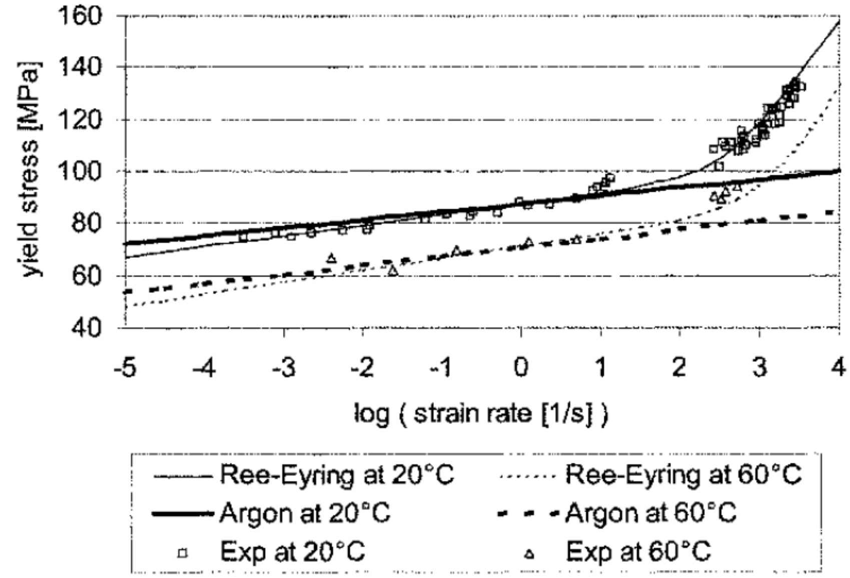

Figure 3.2. Comparison of Ree-Eyring and Argon model with compressive experimental data of PC [54].

(Figure reprinted from Journal of Physics IV France (http://jp4.journaldephysique.org/), **110**, Richeton, J., Ahzi, S., Daridon, L., Rémond, Y., *Modeling of strain rates and temperature effects on the yield behavior of amorphous polymers*, 39-44, Copyright (2003), with permission from EDP Sciences)

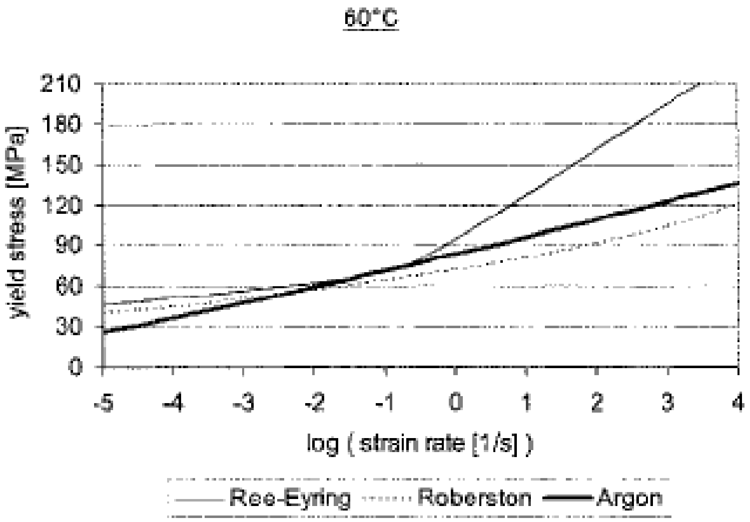

Figure 3.3. Theoretical compressive yield stress *vs.* logarithm of strain rate at 60 ºC for an amorphous polymer to compare the three models [54].

(Figure reprinted from Journal of Physics IV France (http://jp4.journaldephysique.org/), **110**, Richeton, J., Ahzi, S., Daridon, L., Rémond, Y., *Modeling of strain rates and temperature effects on the yield behavior of amorphous polymers*, 39-44, Copyright (2003), with permission from EDP Sciences)

Bauwens, Bauwens-Crowet and Homès [55-59] have done extensive experimental work on amorphous polymers to investigate the validity of the Ree-Eyring model. If the deformation is assumed as a single rate process or α process, which consists of the jump of a segment of macromolecule from one equilibrium position to another over a potential barrier, according to the Eyring viscosity model, which is valid in simple shear experiments [58]:

$$\dot{\gamma} = 2\gamma_{0\alpha} J_{0\alpha} \exp\left(-\frac{Q_\alpha}{RT}\right) Sinh\left(\frac{w_\alpha}{2kT}\right) \tag{3.2}$$

Where, $\dot{\gamma}$ is the shear rate, Q_α is the activation energy of the α process, $J_{0\alpha}$ is a rate constant, R is the universal gas constant, k is the Boltzmann's constant, T is temperature in °K, w_α is the mechanical energy a segment of macromolecule requires to overcome the potential barrier and to produce the permanent elementary shear $\gamma_{0\alpha}$. In the medium to high temperature range or low to medium strain rate range, using the approximation: $Sinh(X) \approx \frac{1}{2}\exp(X)$, due to stress level being sufficiently high, we get [58],

$$\frac{\sigma_{t\alpha}}{T} = A_{t\alpha}\left(ln2C_\alpha\dot{\varepsilon} + \frac{Q_\alpha}{RT}\right) \tag{3.3}$$

$$\frac{|\sigma_{c\alpha}|}{T} = A_{c\alpha}\left(ln2C_\alpha\dot{\varepsilon} + \frac{Q_\alpha}{RT}\right) \tag{3.4}$$

Where, σ_α is the yield stress related to α process, the subscript "t" and "c" denotes tension and compression, respectively, A_α and C_α are constants and $\dot{\varepsilon}$ is the strain rate. According to the Ree-Eyring theory, multiple rate activated process can act in parallel rather than just a single activated process as in the Eyring model. From the Ree-Eyring model for polymer yield stress:

$$\frac{\sigma}{T} = \sum_i \frac{1}{A_i} Sinh^{-1}\left(\frac{C_i\dot{\varepsilon}}{T} exp\frac{Q_i}{RT}\right) \tag{3.5}$$

As can be seen from Equation 3.5, for single activated process or the so-called α process, by assuming, $Sinh(X) \approx \frac{1}{2}\exp(X)$, Equations 3.3 and 3.4 can be retrieved from Equation 3.5.

According to the formalism of the Ree-Eyring theory, yielding of amorphous polymers can be considered dependent on particular degrees of freedom in polymer chain, whose relaxation or activation depends on the applied strain rates and temperatures. For high strain rates and/or low temperatures, the yield behavior of an amorphous polymer, e.g., PC, can be assumed of involving two rate processes, α and β, and the plastic flow due to these processes can be considered additive. The yield stresses in this range can be written as [58],

$$\frac{\sigma_t}{T} = \frac{\sigma_{t\alpha}}{T} + \frac{\sigma_{t\beta}}{T} = A_{t\alpha}\left(ln2C_\alpha\dot{\varepsilon} + \frac{Q_\alpha}{RT}\right) + A_{t\beta}Sinh^{-1}\left(C_\beta\dot{\varepsilon}exp\frac{Q_\beta}{RT}\right) \tag{3.6}$$

$$\frac{|\sigma_c|}{T} = \frac{|\sigma_{c\alpha}|}{T} + \frac{|\sigma_{c\beta}|}{T} = A_{c\alpha}\left(ln2C_\alpha\dot{\varepsilon} + \frac{Q_\alpha}{RT}\right) + A_{c\beta}Sinh^{-1}\left(C_\beta\dot{\varepsilon}exp\frac{Q_\beta}{RT}\right) \tag{3.7}$$

At high strain rates and/or low temperatures, pure viscous flow also takes place at the yielding due to jumps of segments of backbone chain of the macromolecule from one equilibrium position to another similar to the single activated α process. But, the α process is hindered as the molecular movements are partially frozen even when the yield stress is applied. To release these movements, it is necessary to supply an additional energy by applying additional stress. Thus, at high strain rates and/or low temperatures, the observed yield stress can be considered as the sum of two stresses with respect to the α and β processes. Although the transition from single activated process to two rate activated process is smooth and does not occur strictly at a point, it can be approximated by [58]:

$$T_\beta = -\frac{Q_\beta}{Rln2C_\beta\dot{\varepsilon}} \tag{3.8}$$

Using the commercially available PC samples (Makrolon Bayer), Bauwens-Crowet et al. [58] described the yield behavior by assuming the involvement of two different flow processes. Figure 3.4 shows the engineering compressive and tensile yield stress experimental data (Points) in comparison with the curve-fitting using the Ree-Eyring model for multiple rate processes. The constants value used for the curve fitting is given in Table 3.1 [58]. To calculate the constants, a set of straight lines were drawn as in Figure 3.5 which best agrees with the data. The mean slope was taken as A**;** from the mean displacement of these lines Q was calculated**,** and from the mean extrapolated value of the abscissas for $\sigma = 0$, C was calculated [56]. As can be seen in the figures, the experimental data can be well-described by the Ree-Eyring model for PC.

Table 3.1. Constants calculated for fitting the curve in Figure 3.4 [58].

α process	β process
Q_α = 75.5 kcal/mole	Q_β = 9.6 kcal/mole
C_α = 2.40×10^{-31} sec	C_β = 2.76×10^{-9} sec
$A_{t\alpha}$ = 4.35×10^{-4} kg/mm^2 °K	$A_{t\beta}$ = 1.33×10^{-3} kg/mm^2 °K
$A_{c\alpha}$ = 5.7×10^{-4} kg/mm^2 °K	$A_{c\beta}$ = 5.57×10^{-3} kg/mm^2 °K

(Table adopted from Springer and the Journal of Materials Science, **7**, 1972, 176-183, *The temperature dependence of yield of polycarbonate in uniaxial compression and tensile tests*, Bauwens-Crowet, C., Bauwens, J.C., Homès, G., original copyright notice is given to the publication in which the material was originally published; with kind permission from Springer Science and Business Media)

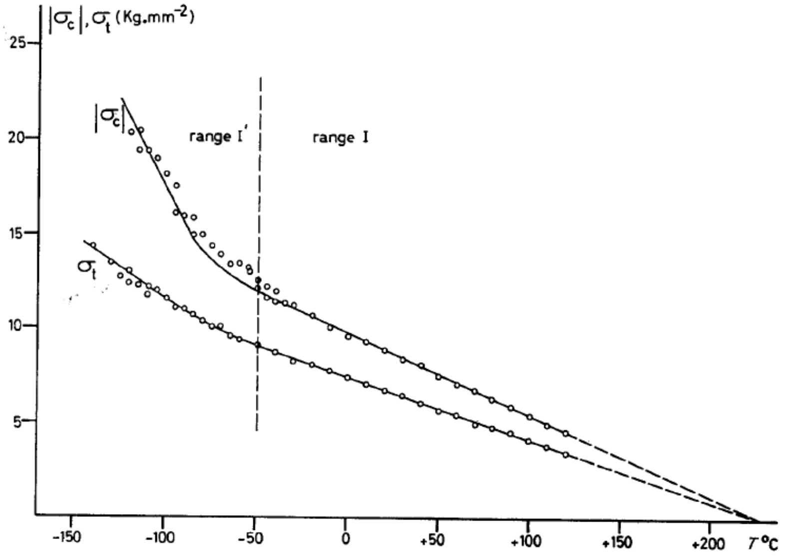

Figure 3.4. Comparison of experimental compressive and tensile yield stresses with the Ree-Eyring model with constants value listed in Table 3.1 at a constant strain rate, $\dot{\boldsymbol{\varepsilon}} = 4.16\times10^{-3}$ /s [58].

(Figure reprinted from Springer and the Journal of Materials Science, **7**, 1972, 176-183, *The temperature dependence of yield of polycarbonate in uniaxial compression and tensile tests*, Bauwens-Crowet, C., Bauwens, J.C., Homès, G., Figure 1, original copyright notice is given to the publication in which the material was originally published; with kind permission from Springer Science and Business Media)

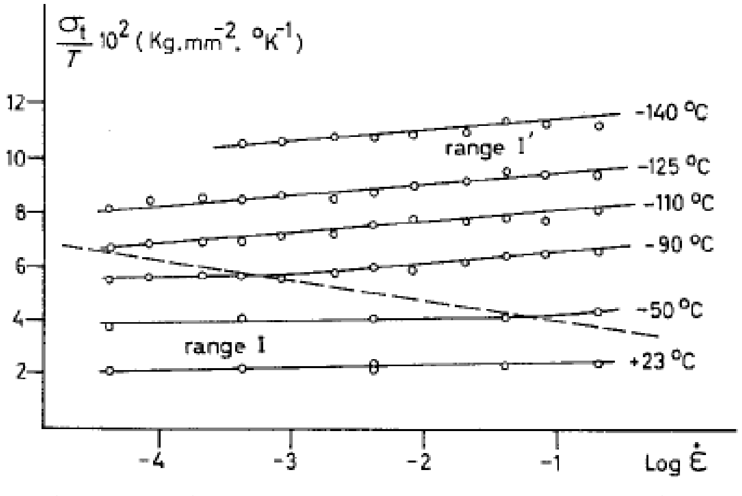

Figure 3.5. Plot of the ratio of tensile yield stress to temperature as a function of logarithm of strain rate (Range I denotes the region of single activated process and range I′ denotes the region of two rate activated process) [58].

(Figure reprinted from Springer and the Journal of Materials Science, **7**, 1972, 176-183, *The temperature dependence of yield of polycarbonate in uniaxial compression and tensile tests*, Bauwens-Crowet, C., Bauwens, J.C., Homès, G., Figure 3, original copyright notice is given to the publication in which the material was originally published; with kind permission from Springer Science and Business Media)

Since, the Ree-Eyring model is based on multiple rate activated processes working simultaneously, it is able to account for the yield behavior even if an amorphous polymer undergoes γ or other relaxation processes. Bauwens-Crowet et al. [58] suggested that the β flow process observed at yield is the same process observed in damping tests and can be correlated with the mechanical loss peak (loss tangent *vs.* temperature at a given frequency). They reported that the value of the activation energy Q_β for PC was in agreement with the value reported from dielectric measurements [58]. They found similar results for PVC, too [56]. According to Bauwens et al. [55], unlike Q_β, Q_α may not be compared with the activation energy related to the primary transition observed in dielectric or mechanical damping tests. Using PC, Bauwens [57] showed that the β yield process and β peak revealed by the oscillatory damping tests are from the same molecular movements, and, thus, the activation energies associated with the respective processes should be equal. Using the area under the curve of the loss tangent peak in the damping test and the translation of this peak with strain rates, Bauwens [57] was able to describe the yield behavior of PC as shown in Figure 3.6, where the points denote the experimental data and the line denotes the modeling.

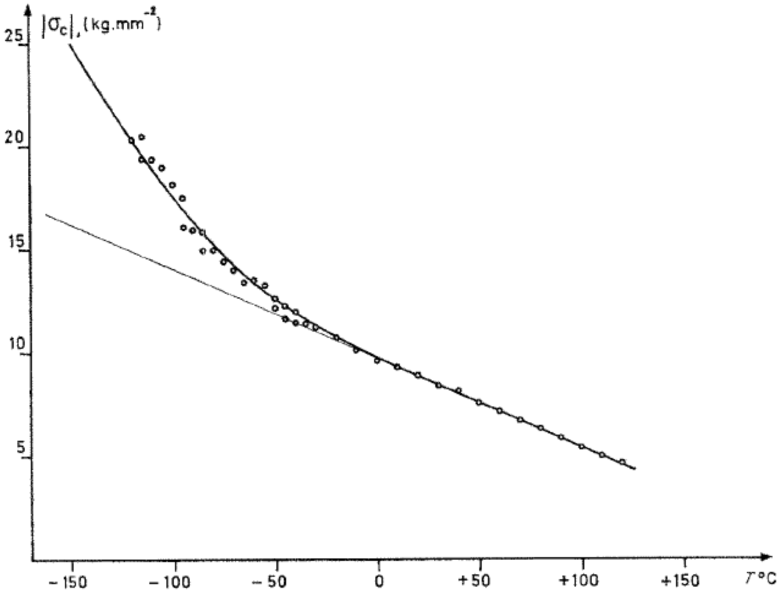

Figure 3.6. Plot of the compressive yield stress *vs.* temperature at constant strain rate [57]. (Figure reprinted from Springer and the Journal of Materials Science, **7**, 1972, 577-584, *Relation between the compression yield stress and the mechanical loss peak of bisphenol-A-polycarbonate in the β transition range*, Bauwens, J.C., Figure 5, original copyright notice is given to the publication in which the material was originally published; with kind permission from Springer Science and Business Media)

Similar yielding behavior has been described by the Ree-Eyring model for PVC [56], as shown in Figure 3.7. As shown in the figure, similar to PC, there is a transition strain rate depending on the temperature and vice versa where the slope changes in the plot of ratio of yield stress to temperature *vs.* logarithm of strain rate. Similar modeling has also been done to describe the yielding behavior of PMMA in compression [59]. Roetling [60, 61] conducted an identical study at the similar time to describe the yield behavior of Poly(ethylmethacrylate) (PEMA) and PMMA. The plot for PMMA is shown in Figure 3.8. The constants were calculated for fitting the data by assuming that the contribution of the lower energy activation process or β process is negligible at the lower strain rates and/or higher temperatures, whereas both α and β processes are important at higher strain rates and/or lower temperatures. Similar study was also done by Rietsch et al. [62] using PC. Experimentally, similar yielding behavior based on the transition of slope depending on the strain rate at a particular temperature (showing two distinct slope) has been reported in literature for PC [44, 45, 47, 48, 63], PMMA [44, 63], Polypropylene (PP) [64, 65], Thermoplastic Olefin (TPO) [66], Polyamideimide (PAI) [63] and Polyvinylidene difluoride (PVDF) [45]. Similar behavior has also been reported for Young's modulus [44, 66, 67].

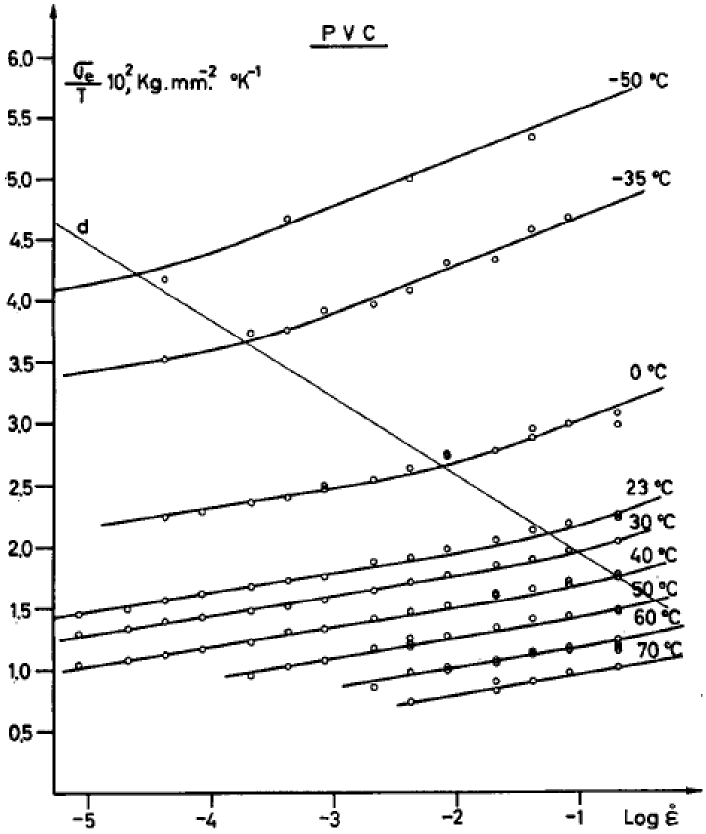

Figure 3.7. Plot of yield stress to temperature as a function of logarithm of strain rate for PVC [56].

(Figure reprinted from Journal of Polymer Science Part A-2: Polymer Physics, **7**, Bauwens-Crowet, C., Bauwens, J.C., Homès,G., *Tensile yield-stress behavior of glassy polymers*, 735-742, Copyright © 1969 John Wiley & Sons, Inc., with permission from John Wiley & Sons, Inc.)

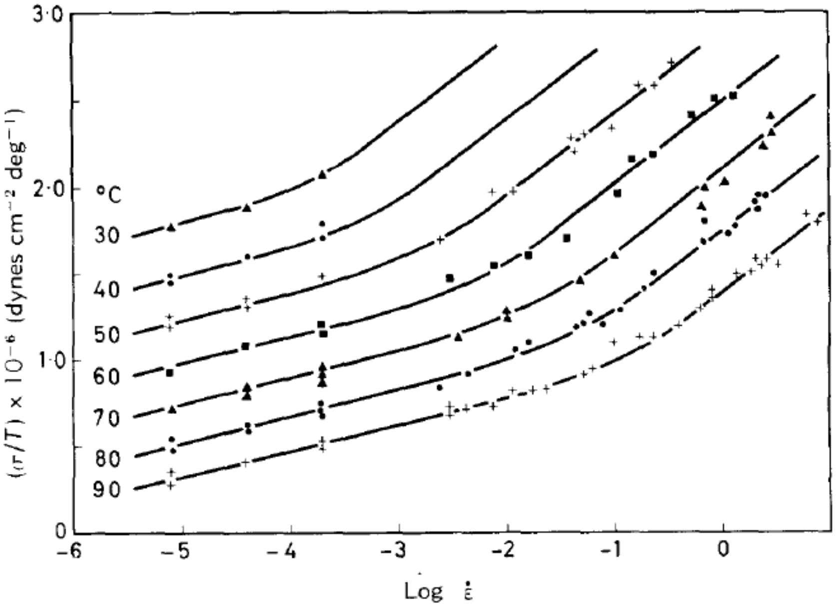

Figure 3.8. Plot of yield stress to temperature as a function of logarithm of strain rate for PMMA [61].

(Figure reprinted from Polymer, **6**, Roetling, J.A., *Yield stress behaviour of polymethylmethacrylate*, 311-317, Copyright (1965), with permission from Elsevier)

Mulliken and Boyce [48] performed dynamic mechanical analysis (DMA) on PC samples to correlate the strain rate dependent β transition peak with the transitional strain rate where the single activated process in amorphous polymers changed into two rate process. Figure 3.9 shows the representative PC loss tangent curves in the region of α-transition as a function of temperature and strain rate. As shown in the figure, the glass (α) transition shifted to higher temperatures with increasing strain rate. By tracing the temperature location of the α-peak with increasing strain rate, the PC glass transition was observed to shift approximately 4.7 ºC per decade increase in strain rate. For β transition, the shift factor for PC was 15.3 ºC per decade increase in strain rate. These DMA data were utilized together with a time-temperature shift that takes into account the different rate dependencies of α and β transitions to predict the elastic behavior at all strain rates and temperatures. Analytical expressions for the elastic moduli of PC were developed by first decomposing the storage modulus reference curves obtained from DMA into their respective α and β components. As the curve was traced with decreasing temperature, a significant upturn was observed at around -25 ºC, which can be correlated with the onset of restriction of the β-process. Using this analysis, the PC storage modulus reference curve was divided into α and β components as shown in Figure 3.10. These α and β components were then considered to shift with strain rates by the amounts determined using the shift calculated in peak transition. The entire modulus curve was then reconstructed for any strain rate by first shifting the components of the reference curve by the appropriate amounts, and then adding the components at every temperature. This decompose/shift/reconstruct (DSR) method enabled prediction of the elastic modulus of PC at temperatures and strain rates well beyond the capabilities of the DMA instrument, as shown in Figure 3.11. As can be seen in the figure, the DSR method can be used to predict the strain rate at which a significant transition in material behavior can be expected. By assuming that this significant material transition is due to the restriction of the same molecular mechanism associated with the β-transition, the shift in β-transition can be used to predict the strain rate at which the yield behavior of amorphous polymer undergoes a transition. The transition strain rate predicted by the DSR method was consistent with the compressive yield stress data obtained through experimentation *via* Instron and split-Hopkinson bar tests. Although not as straight forward as PC, similar method was applied to PMMA which showed a very low transition strain rate (10^{-5} /s to 10^{-4} /s).

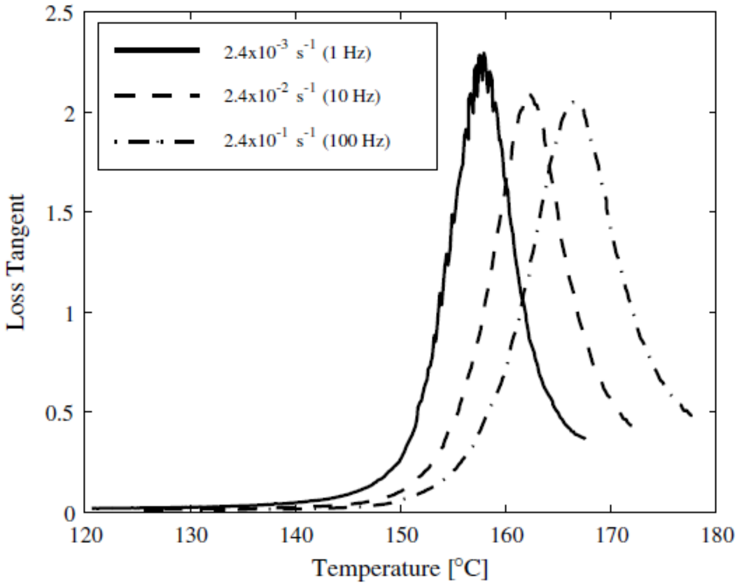

Figure 3.9. PC loss tangent peak for α-transition as a function of temperature and strain rate [48].

(Figure reprinted from International Journal of Solids and Structures, **43**, Mulliken, A.D., Boyce, M.C., *Mechanics of the rate dependent elastic–plastic deformation of glassy polymers from low to high strain rates*, 1331-1356, Copyright (2006), with permission from Elsevier)

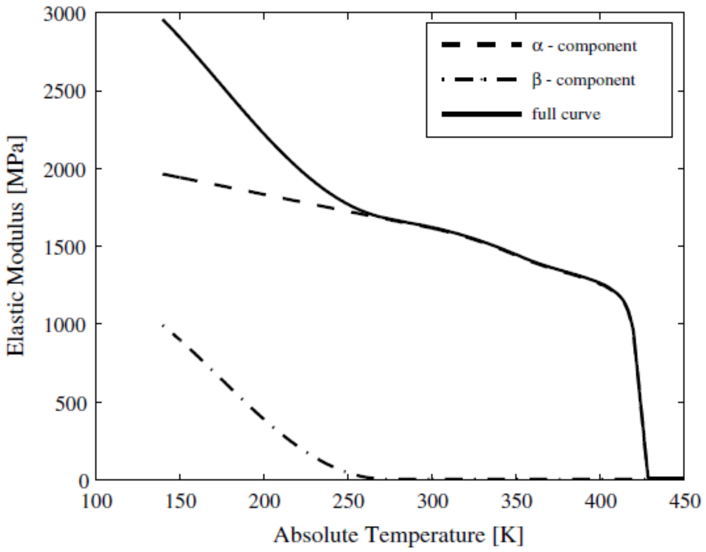

Figure 3.10. Decomposition of α and β components of PC storage modulus curve at 3.2×10^{-3} /s [48].

(Figure reprinted from International Journal of Solids and Structures, **43**, Mulliken, A.D., Boyce, M.C., *Mechanics of the rate dependent elastic–plastic deformation of glassy polymers from low to high strain rates*, 1331-1356, Copyright (2006), with permission from Elsevier)

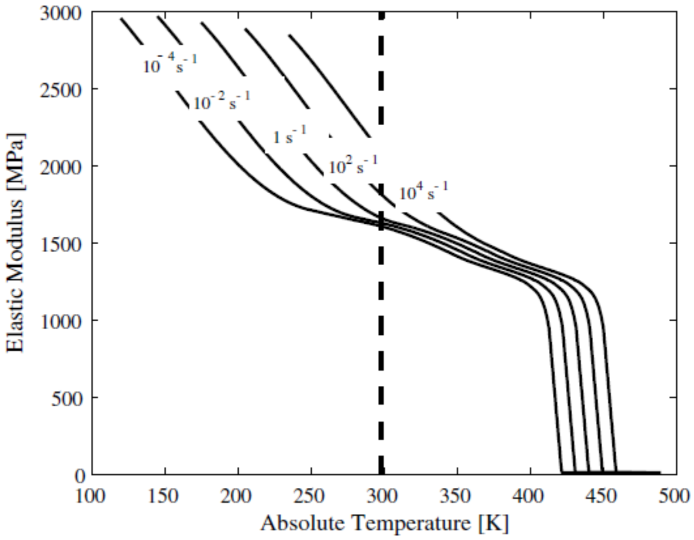

Figure 3.11. DSR model prediction of PC elastic modulus at different strain rates (The vertical dash line denotes room temperature: 298 ºK) [48].

(Figure reprinted from International Journal of Solids and Structures, **43**, Mulliken, A.D., Boyce, M.C., *Mechanics of the rate dependent elastic–plastic deformation of glassy polymers from low to high strain rates*, 1331-1356, Copyright (2006), with permission from Elsevier)

3.2 Pressure Dependent Mechanical Behavior of Polymers

The pressure dependent mechanical behavior of polymers and volume change under deformation is another area of concern when modeling scratch behavior of polymers. Spitzig and Richmond [68] studied the stress-strain response of high density polyethylene (HDPE) and PC in tension and compression at imposed pressures up to 1104 MPa to study the effect of hydrostatic pressure. They found that the strength differential between tension and compression was due to the pressure-dependent yielding in case of HDPE. In case of PC, the effect is due to the third stress invariant or to anisotropy. They suggested that the flow stress is linearly dependent on mean pressure and inelastic volume change is negligible, based on the polymers investigated. Their results also showed that the pressure dependence of yield stress in polymers is the same as that of the initial modulus. Figure 3.12 shows the effect of hydrostatic pressure on the initial moduli of the polymers investigated. As shown in the figure, a linear relationship can be established in case of initial moduli, and, thus, for yield stress too. The linear relationship between yield stress and hydrostatic pressure was also reported by Sauer et al. [69], as shown in Figure 3.13. Using the uniaxial tensile testing up to the point of necking, Powers and Caddell [70] have reported a maximum volume change of about 0.6% for PMMA and PC, which can be considered negligible. Similar negligible inelastic volume change in compression for PC and PVC was also reported by Kitagawa and Yoneyama [71].

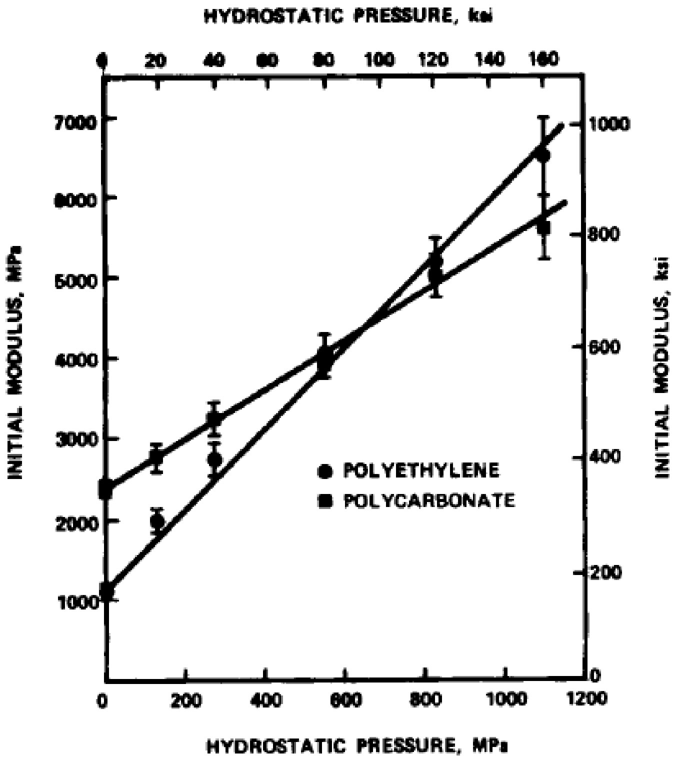

Figure 3.12. Effect of hydrostatic pressure on the initial moduli of HDPE and PC [68].
(Figure reprinted from Polymer Engineering & Science, **19**, Spitzig, W.A., Richmond, O., *Effect of hydrostatic pressure on the deformation behavior of polyethylene and polycarbonate in tension and in compression*, 1129-1139, Copyright © 1979 Society of Plastics Engineers, Inc., with permission from John Wiley & Sons, Inc.)

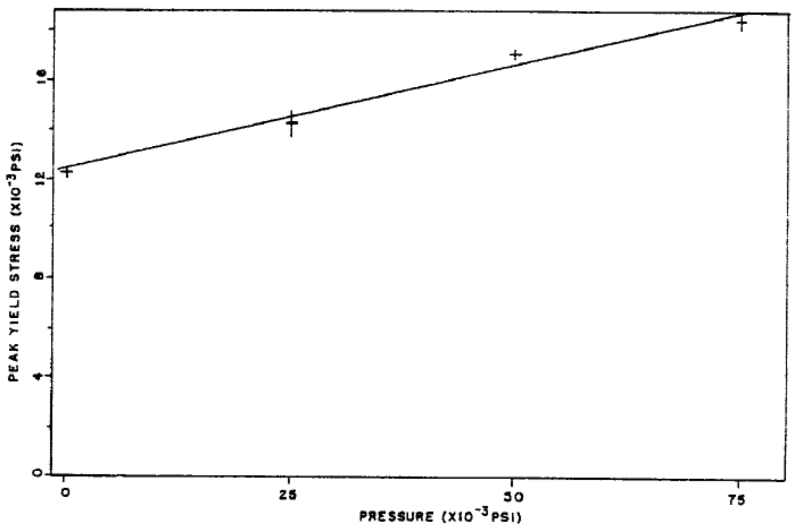

Figure 3.13. Plot of tensile yield stress as a function of pressure in PC [69].
(Figure reprinted from European Polymer Journal, **6**, Sauer, J.A., Mears, D.R., Pae, K.D., *Effects of hydrostatic pressure on the mechanical behaviour of polytetrafluoroethylene and polycarbonate*, 1015-1032, Copyright (1970), with permission from Elsevier)

3.3 Frictional Behavior during Sliding Contact involving Polymers

Since scratch-induced deformation involves sliding indentation of a rigid asperity over the surface of polymers, the contact between the tip and the substrate, the surface roughness of the contacting bodies, the evolution of friction and the dissipation of frictional energy needs careful consideration for quantitative modeling *via* FEM. the most straightforward treatment of the frictional issue is to assign a coefficient of friction, μ, to the interacting surfaces and obtain the frictional force, F_t, based on the Coulomb's or Amonton's law of friction [72]:

$$F_t = \mu F_n \tag{3.9}$$

Where F_n is the normal force and μ is the coefficient of surface friction. As shown in Figure 2.2, as the scratch tip pushes into the substrate by means of a controlled F_n or displacement/depth, and traverses across the substrate, the tip no longer just interacts with the surface of the polymer substrate. It also interacts with the sub-surface, which adds another level of complexity. As a result, a constant μ may no longer be appropriate to account for the sub-surface deformation. Due to this interaction with the sub-surface, a resistance force arises against the tip movement from the material pile-up in front of scratch tip, which gives rise to the so-called “scratch coefficient of friction (μ_s)”. The μ_s can be divided into two parts: a traditional surface coefficient of friction, μ, and an additional coefficient term resulting from the resistance due to material pile-up in front of the moving scratch tip. The scratch tip geometry also plays an important role during this evolution of scratch coefficient of friction.

The Coulomb’s or Amonton’s law of friction is based on the assumptions that the friction coefficient is independent of: the normal load applied, the apparent area of contact between the contacting bodies, the sliding velocity when motion starts [73]. The coefficient of friction or scratch coefficient of friction has been shown to increase with increasing normal load for PC [74], PP [74], surface treated TPOs [36], different grades of SANs [8]; to remain almost constant for TPOs with various level of surface roughness [43]; with 1 mm spherical tip. The coefficient of friction may not remain constant with apparent area of contact for polymers [73]. The coefficient of kinetic friction generally has a negative slope with sliding velocity [73]. Thus, the simple Coulomb’s or Amonton’s law of friction may not be sufficient to describe the complex frictional behavior involved in the scratch process.

Bowden and Tabor [72] first proposed that for two metals in sliding contact, local welding spots form at individual contact points due to high pressure and these contact spots are subsequently sheared by the relative sliding of the surfaces. Later, it was proposed that the asperities during sliding contact do not have to weld, but only the interfacial adhesion between asperities is sufficient to account for the friction in metals and ceramics. In addition to the frictional energy to overcome the adhesion developed at the real areas of contact between the contacting surfaces, energy is also required for deformation due to grooving and plowing. Although very simplistic, based on the assumption that there is negligible interaction between adhesion and deformation process during sliding, the total intrinsic coefficient of friction (μ_i) can be considered as the summation of friction due to adhesion (μ_a) and friction due to deformation (μ_d) [75].

$$\mu_i = \mu_a + \mu_d \tag{3.10}$$

For ductile materials, the coefficient of friction due to adhesion (μ_a) for dry contact can be written as [72]:

$$\mu_a = \frac{A_r \tau_a}{F_n} = \frac{\tau_a}{P_r} \tag{3.11}$$

Where, A_r is the real area of contact, τ_a is the shear strength and P_r is the mean real pressure. Again, for polymers, due to the rate dependent response, τ_a is also dependent on strain rate. However, it has been shown that, τ_a generally remains almost unchanged or, in some cases, decreases at room temperature with an increase in sliding velocity [73, 76].

For polymers, the shear strength, τ_a can be considered as a linear function of mean contact pressure, P_r [73]:

$$\tau_a = \tau_0 + \alpha P_r \tag{3.12}$$

From Equation 3.11,

$$\mu_a = \frac{\tau_0}{P_r} + \alpha \tag{3.13}$$

Where, τ_0 is the intrinsic characteristic shear strength and α is the pressure coefficient. Bowers [77] showed that the values of coefficient of friction as a function of pressure in sliding contact can be determined from shear strength as a function of pressure using friction measurement of thin polymeric films and bulk shear data. Briscoe and Tabor [78] studied the effect of pressure on the shear properties of thin polymeric films (HDPE and PMMA) by conducting frictional experiments with varying tip geometry and contact loading. During the sliding experiments, the frictional force measured was divided by the calculated area of contact (From Hertz elastic deformation analysis) to give the critical shear stress for the polymer film. They found that increase in pressure increases the shear yield stress linearly following Equation 3.12. They compared their data with those obtained for torsional shear of bulk polymers under various hydrostatic pressure. They found that the value of pressure coefficient, α, remains almost same in both type of experiments while τ_0 differs by a large factor. They explained that the low value of τ_0 in the films is due to the shear process being constrained in a very narrow zone in thin films, and, thus, changing the molecular orientation in the polymer. Also, the strain experienced by the thin film was much higher compared to the bulk systems [78]. Similar findings was also reported in literature [76, 79]. Duckett et al. [80] studied the torsional behavior of PC (Makrolon 2800) under superposed hydrostatic pressures. It was found that the shear yield stress increases linearly with pressure (Figure 3.14). At room temperature, for $\dot{\gamma}_{\mathrm{oct}}$=$1.86\times10^{-2}$ /s, the value of pressure coefficient, α, was found to be 0.07 and τ_0 was calculated to be 41 MPa (Calculated from the stress-strain plot in

Figure 3.14). Using the torsion tests, similar behavior has also been observed in PMMA (Figure 3.15) [81].

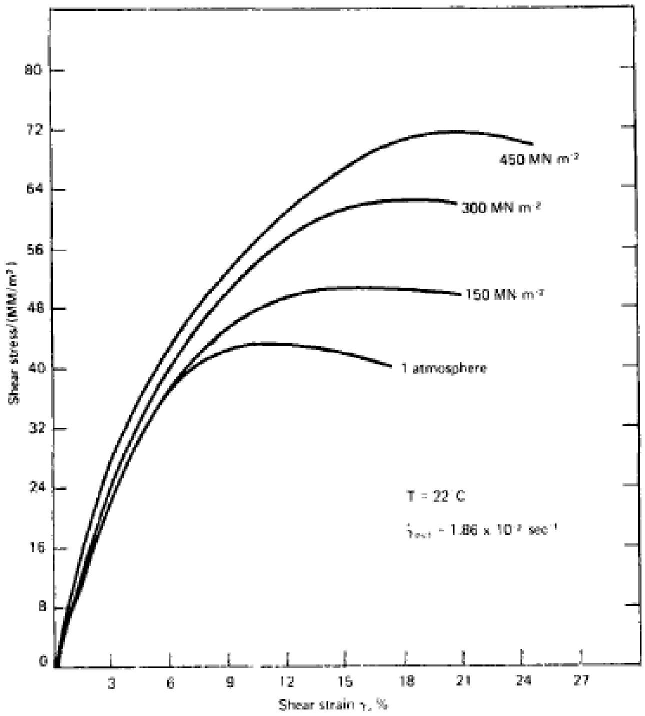

Figure 3.14. Pressure dependent shear stress-strain response in PC [80].
(Figure reprinted from British Polymer Journal, **10**, Duckett, R.A., Goswami, B.C., Smith, L.S.A., Ward, I.M., Zihlif, A.M., *The yielding and crazing behaviour of polycarbonate in torsion under superposed hydrostatic pressure*, 11-16, Copyright © 1978 Society of Chemical Industry, with permission from John Wiley & Sons, Inc.)

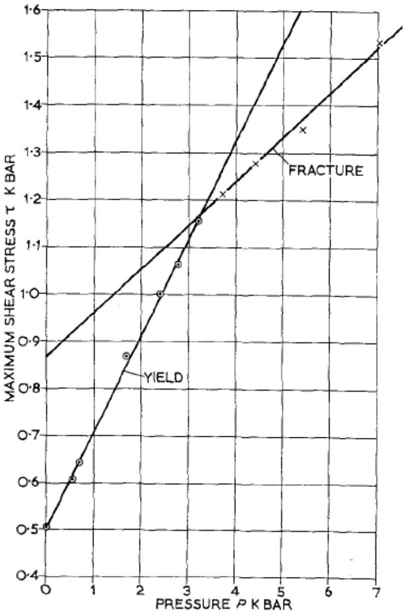

Figure 3.15. Maximum shear stress as a function of pressure in PMMA (Θ: yield, ×: fracture) [81].

(Figure reprinted from Springer and the Journal of Materials Science, **5**, 1970, 29-39, *The effect of hydrostatic pressure on the shear yield behaviour of polymers*, Rabinowitz, S., Ward, I.M., Parry, J.S.C., Figure 6, original copyright notice is given to the publication in which the material was originally published; with kind permission from Springer Science and Business Media)

For ductile materials, the coefficient of friction due to deformation (μ_d) for a spherical rigid asperity of radius R in contact with a softer body can be written as [73]:

$$\mu_d = \frac{4}{3\pi}\frac{a}{R} \tag{3.14}$$

Where, a is the contact radius. For a relatively large width of the groove compared to radius of sphere [82]:

$$\mu_d = \frac{2}{\pi}\left\{\left(\frac{R}{a}\right)^2 Sin^{-1}\left(\frac{a}{R}\right) - \left[\left(\frac{R}{a}\right)^2 - 1\right]^{1/2}\right\} \tag{3.15}$$

As can be deduced from the equations, μ_d increases as the tip goes deeper. Although the material piles up in front of the tip in many cases during the scratch process, the model of rigid spherical asperity to calculate μ_d neglected the pile-up of material in front of the tip. However, the contribution from material pile-up in front of the tip can be significant in some cases, specifically, at high normal load.

The effect of chain orientation on the frictional development during sliding contact also has to be considered in case of polymer scratch. Tabor and Williams [38] studied the evolution of friction during sliding of the Polytetrafluoroethylene (PTFE) samples using hemispherical slider. They concluded that, since the shear strength across the chains was higher than the shear strength along the chains, the friction is higher across the molecular chains (Figure 3.16). They also found that the deformation component of friction is independent of the direction of sliding. Bely et al. [39] showed that the frictional value is higher in the unoriented polymer compared to the oriented one. Since the coefficient of friction due to adhesion can be correlated with the bulk shear strength, as described earlier, the effect of chain orientation in polymers can be included by taking into account orientation dependent shear strength.

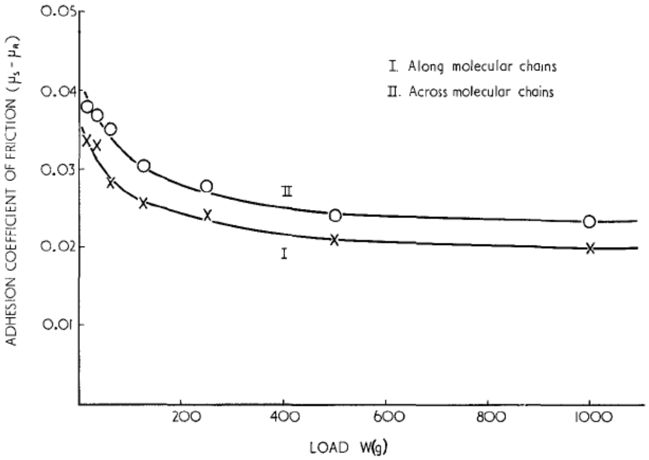

Figure 3.16. Variation of coefficient of friction due to adhesion as a function of applied normal load using 5 mm spherical steel tip on PTFE [38].

(Figure reprinted from Wear, **4**, Tabor, D., Williams, D.E.W., *The effect of orientation on the friction of polytetrafluoroethylene*, 391-400, Copyright (1961), with permission from Elsevier)

Surface roughness of the contacting bodies is also important, specifically in multi-asperity contacts as it determines the real area of contact, and, thus, evolution of friction. But, for scratching using 1 mm diameter spherical tip, the normal load required to induce plastic contact is comparatively low. For plastic contacts, the coefficient of friction due to adhesion is independent of surface roughness [73]. Thus, for 1 mm diameter spherical tip scratching with increasing normal load, for a fairly smooth surface (roughness in nm level), the surface roughness effect can be considered negligible.

In any sliding interaction, most of the input frictional energy is generally spent in plastic deformation which is directly converted to heat in the material close to interface [73]. In dry contact, this heat is conducted into two sliding members through contact spots with a high temperature gradient. Since the mechanical and frictional properties of polymers depend on operating temperature, the temperature rise due to frictional heat dissipation is really important. As the temperature rise at the contacts is very transient in nature and consequently very difficult to measure accurately, a number of theoretical models have been developed [72, 83-87] to predict the temperature at the asperity contacts. Based on the concept of partition of heat by Blok [83], the interface temperature can be calculated which may be adequate for a high contact stress situation. However, if most of the heat is generated in the softer body (Polymers, in case of steel ball sliding over polymers), the basic assumption of the partition of heat, i.e., same temperature on both surfaces at the interface, may not be very accurate [73]. Also, in these theoretical models, heat transfer due to conduction is considered only. A number of techniques have also been used to measure the transient temperature rise in a sliding contact with limited success. Of them, Infrared measurement is considered to give most accurate measurement of the flash temperature. It has been shown that, in case of polymers, the temperature rise is small due to reduction in heat generation per unit area as a consequence of comparatively very large area of contact in polymers [88, 89]. Using a Polyether-ether-ketone (PEEK) ball of 19 mm diameter sliding on Sapphire disc, Wong et al. [90] recently measured the maximum temperature rise at the contact by employing a Infrared camera. They found negligible increase in temperature for 40 N load at a speed of 100 mm/s which is also the scratching speed recommended by ASTM standard for scratch testing [5]. A minimal increase in temperature is reported up to a speed of ~1 m/s (For loading up to 40 N); beyond that the temperature increases sharply.

CHAPTER IV

EXPERIMENTAL OBSERVATION OF MODEL SYSTEMS

This chapter discusses the experimental work undertaken to quantitatively predict the scratch behavior of polymers *via* FEM simulation. Uniaxial tension and compression tests at different strain rates, DMA study, coefficient of friction measurement, scratch testing was performed on two amorphous model polymeric systems and results are summarized and discussed. In addition to that, percent relaxation during the scratch process is measured for the model polymers in order to study the viscoelastic recovery.

4.1 Model Systems

SAN, in the form of reactor-grade random copolymers polymerized by free-radical reactions, and PC (Makrolon 2800 from Bayer MaterialScience) systems were provided by BASF SE (Ludwigshafen, Germany). The SAN model system contained 19 percent AN by weight. Molecular weight information of the model systems was provided by BASF SE and is summarized in Table 4.1.

Table 4.1. Molecular weight information of the model polymers.

	SAN	**PC**
Acrylontrile content (wt%)	*19*	-
Weight average molecular weight, M_W (kg/mol)	*134*	*67*
Polydispersity	*4.1*	*2.6*

The resins were produced into injection-molded plaques with dimensions of 150 mm × 150 mm × 6 mm and 150 mm × 150 mm × 3 mm. Upon receipt, all the injection-molded plaques were first dried in an oven in between two smooth glass plates at 80 ºC for 6 hours in vacuum. Then the samples were annealed at ~10 °C above their respective glass transition temperature (T_g) for 1 hour in vacuum (T_g for PC is ~148 °C and for SAN is ~120 °C). Finally, the samples were slow cooled to room temperature at 1.8 ºC/min. This heat treatment procedure is expected to minimize any residual surface stresses and eliminate any chain orientation induced during the injection molding process. The surface finish of the plaques was very smooth with RMS Roughness values of 26 nm and 45 nm for PC and SAN samples, respectively. The roughness value was measured on an area of 525 µm × 700 µm.

4.2 Mechanical Property Characterization

4.2.1 Testing Procedure

Uniaxial tension and compression tests were performed following the ASTM D638 [41] and D695 [42] standard, respectively. A screw-driven MTS® Insight load frame equipped with a 30 kN capacity load cell was used for all tests. MTS® Testworks 4 was used as the software interface for data collection.

For uniaxial tensile testing, injection-molded plaques of 150 mm × 150 mm × 3 mm were cut to dog-bone shape specimens with a nominal thickness of 3 mm and width of 6 mm. The samples were polished to make sure that no marking or stress concentration sites were present. Actual dimensions were measured with a digital micrometer caliper. The tensile testing was conducted at four nominal strain rates ~ 1.6×10^{-3} /s, 3.3×10^{-3} /s, 1.6×10^{-2} /s and 1.6×10^{-1} /s. An MTS® extensometer with a gauge length of 25.4 mm was used to monitor the displacement for strain calculations. At least three samples were tested at each strain rate.

Prismatic uniaxial compression specimens (12.7 mm × 6 mm × 6 mm) were prepared from the 150 mm × 150 mm × 6 mm injection molded plaques by precision-cutting using a diamond saw. After cutting the samples, the surfaces were polished using P2400 first, and, then P4000 grit silicone-carbide abrasive paper. Care was taken to ensure that all the edges were flat and square. The compression test was conducted at three nominal strain rates ~ 3.1×10^{-4} /s, 3.1×10^{-3} /s and 3.1×10^{-2} /s. An MTS® laser extensometer was used to monitor the displacement and strain. White lithium grease was used to provide sufficient lubrication to minimize contact friction between the fixture and the sample surfaces under compression. At least three samples were tested at each strain rate.

4.2.2 Results and Discussion

4.2.2.1 Mechanical Properties of PC

Figure 4.1 shows the representative plot of compressive true stress-strain behavior of PC and true yield stress values obtained in uniaxial compression testing as a function of strain rate, respectively. The engineering stress-strain data obtained during the test was converted to true stress-strain by considering volume preservation during plastic deformation. As shown in Figure 4.1b, compressive yield stress increases with strain rate for PC. Also, the post-yield behavior remains almost unchanged with increase in strain rate for PC in compression (Figure 4.1a).

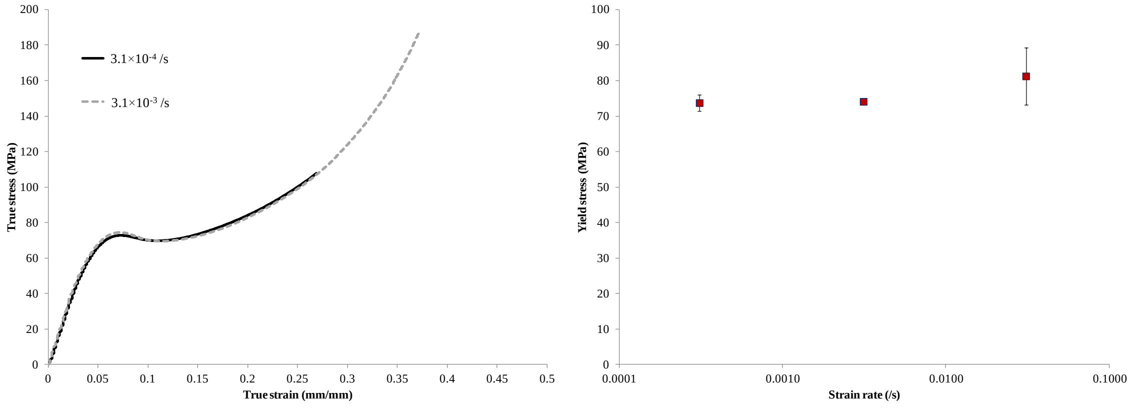

(a) (b)

Figure 4.1. PC - (a) Representative stress-strain plot in compression; (b) True compressive yield stress as a function of strain rate.

Figure 4.2 shows the modulus and yield strain values of PC in compression as a function of strain rate, respectively. A slight increase in compressive modulus and yield strain in compression can be observed for PC with increase in strain rate.

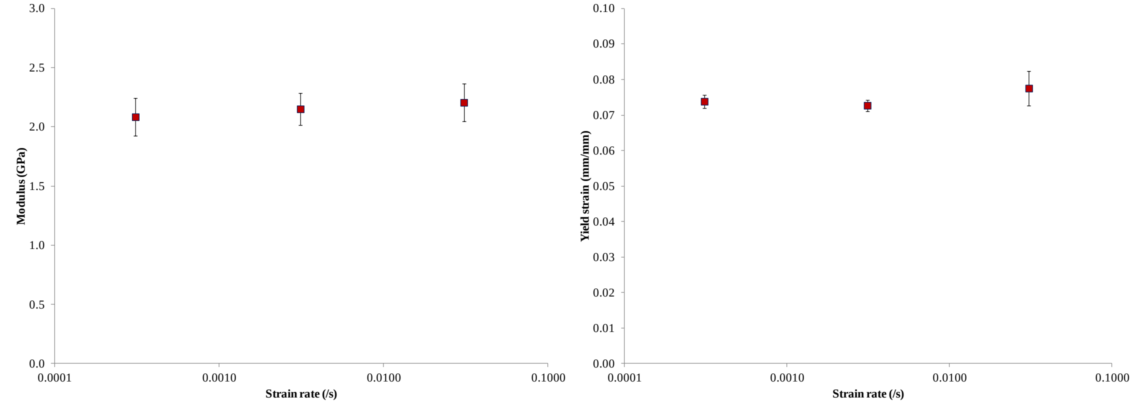

(a) (b)

Figure 4.2. PC - (a) Compressive modulus; (b) Yield strain in compression; as a function of strain rate.

Figure 4.3 shows the true tensile yield stress, modulus and yield strain of PC as a function of strain rate, respectively. A slight increase in yield stress in tension can be observed for PC, whereas modulus and yield strain in tension remains essentially the same.

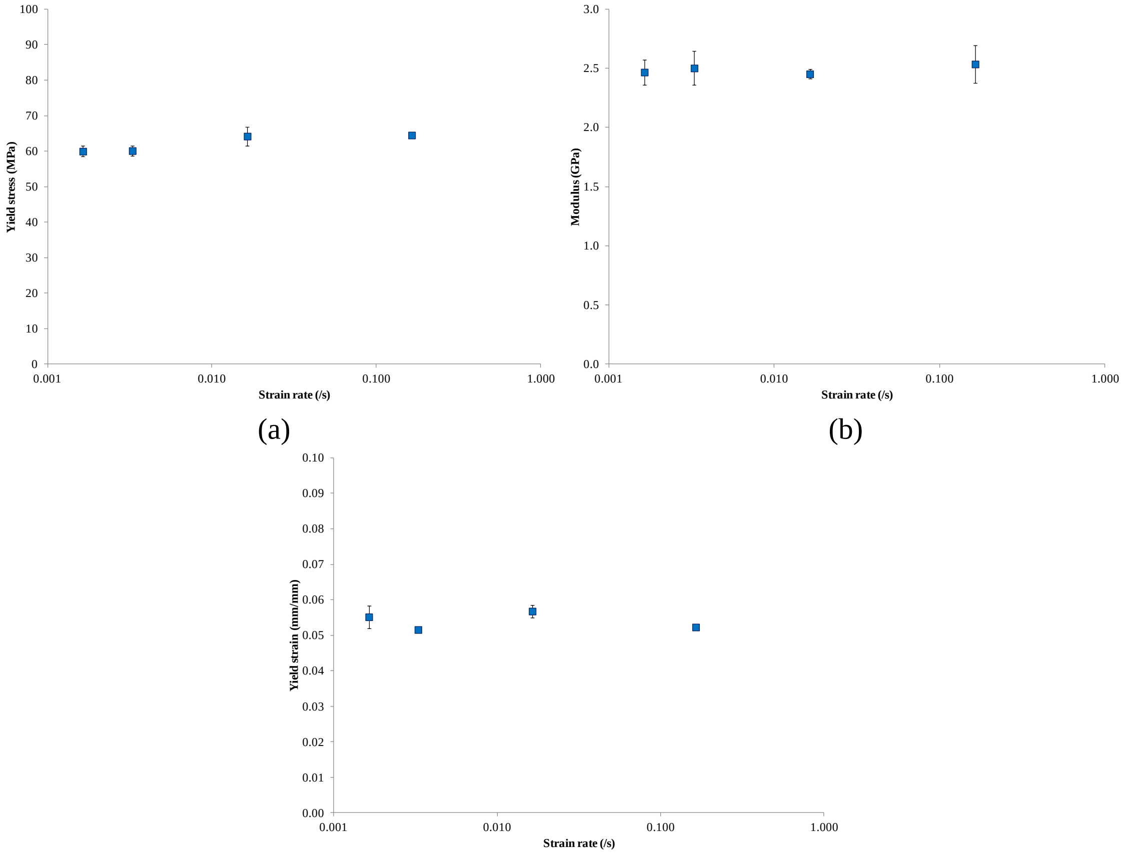

(a)

(b)

(c)

Figure 4.3. PC - (a) Yield stress; (b) Modulus; (c) Yield strain; in tension as a function of strain rate.

4.2.2.2 Mechanical Properties of SAN

Figure 4.4 shows the representative plot of compressive true stress-strain relationship and true yield stress values in compression for SAN as a function of strain rate, respectively. Similar to PC, the engineering stress-strain data obtained during the test was converted to true stress-strain by considering that the volume is preserved during plastic deformation. As shown in Figure 4.4b, compressive yield stress increases with strain rate for SAN. Also, compressive post-yield behavior remains almost similar with increase in strain rate for SAN (Figure 4.4a).

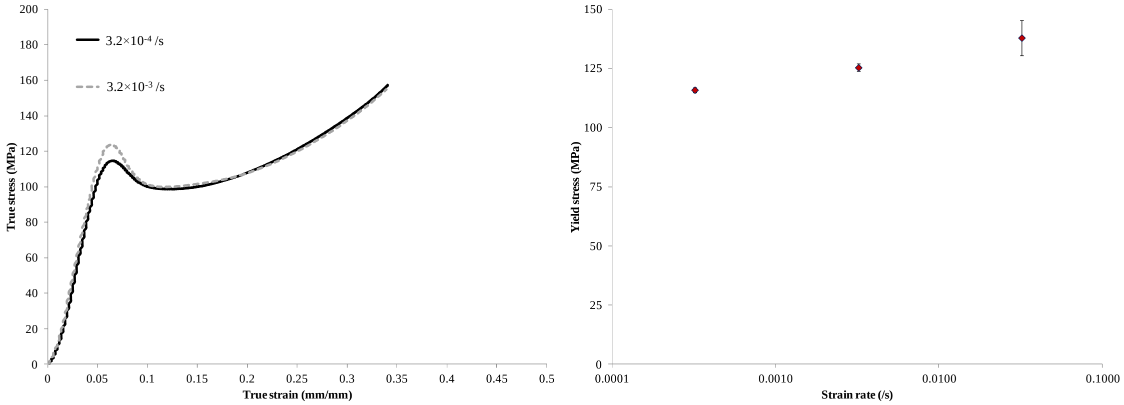

(a) (b)

Figure 4.4. SAN - (a) Representative stress-strain plot in compression; (b) True compressive yield stress as a function of strain rate.

Figure 4.5 shows the modulus and yield strain values of SAN in compression as a function of strain rate, respectively. An increase in compressive modulus with strain rate can be observed for SAN whereas the yield strain value in compression increases slightly with strain rate.

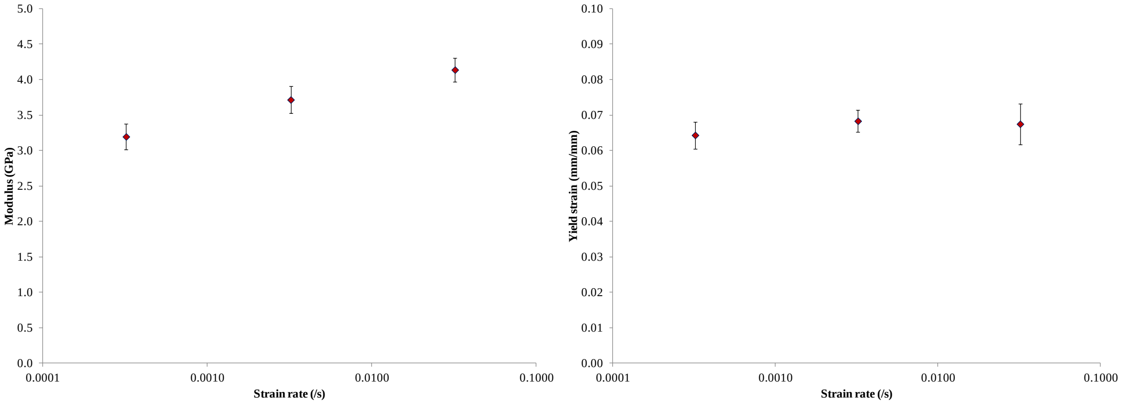

(a) (b)

Figure 4.5. SAN - (a) Compressive modulus; (b) Yield strain in compression; as a function of strain rate.

SAN shows brittle behavior in tension, and, consequently, only tensile strength values can be obtained during the test. Figure 4.6 shows the tensile strength and modulus of SAN as a function of strain rate, respectively. The tensile strength remains almost constant despite the increase in strain rate whereas the tensile modulus shows an increase with strain rate.

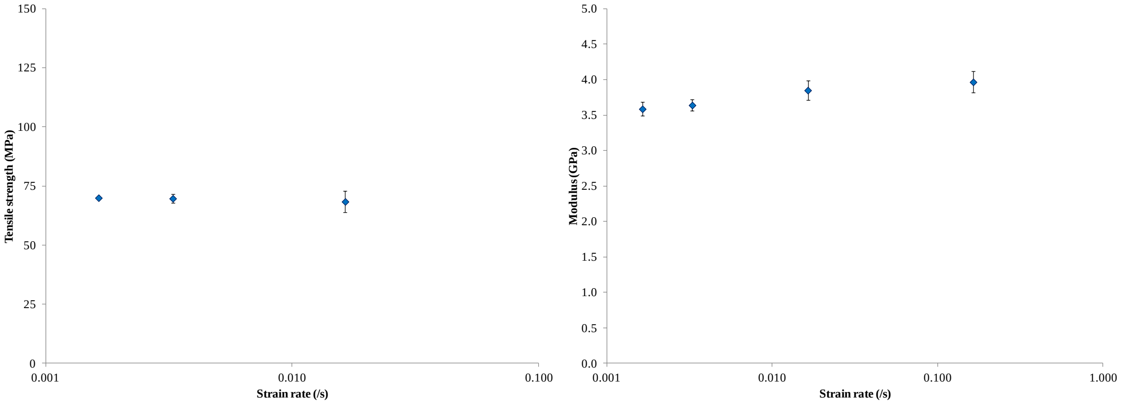

(a) (b)

Figure 4.6. SAN - (a) Strength; (b) Modulus; in tension as a function of strain rate.

4.3 Dynamic Mechanical Analysis

4.3.1 Analysis Procedure

Dynamic mechanical analysis (DMA) was performed on a TA Instruments ARES G2 Rheometer using a torsional fixture. Samples with nominal dimension of 30 mm × 9 mm × 3 mm were used for the DMA tests. The specimens were given a pre-tension of ~200 gm and a strain level of 0.05% was used. The samples were tested from -140 ºC to 200 ºC for PC and -140 ºC to 160 ºC for SAN. A step process was used from -140 ºC to 30 ºC at 3 ºC/min and a ramp process at 2 ºC/min was used afterwards. The samples were tested at frequencies of 0.1 Hz, 0.5 Hz, 1 Hz, 5 Hz and 10 Hz which correspond to strain rates of 2×10^{-4} /s, 1×10^{-3} /s, 2×10^{-3} /s, 1×10^{-2} /s, 2×10^{-2} /s, respectively, according to the relation provided in the literature [48]. Storage modulus and loss modulus information was recorded during the test and corresponding loss tangent value was calculated.

4.3.2 Results and Discussion

4.3.2.1 Dynamic Mechanical Analysis of PC

Representative storage moduli and loss tangent plots in logarithmic scale obtained in DMA test for PC is shown in Figure 4.7. A distinctive α and β transition peak can be observed at ~ 150 °C and ~ -96 °C at 1 Hz, respectively. The shape of the curves and the location of the transitions matches well with the data provided in the literature for PC [57, 91]. Figure 4.8 shows the plot of loss tangent as a function of temperature near the β transition zone for the five frequencies tested. The β transition shifted to higher temperature with increase in frequency. Similar behavior is also observed for α transition. Using the shift in β transition, the activation energy for β transition is calculated to be 9.31 kcal/mole which matches well with the activation energy parameter used for modeling strain rate dependent yield behavior of PC using the Ree-Eyring theory (Table 3.1). As discussed by Bauwens [57], using PC (Makrolon Bayer), the β yield process and β transition observed in DMA test are due to the same molecular movements, and, thus, the respective activation energies associated with the processes should be equal, which is shown to be the case.

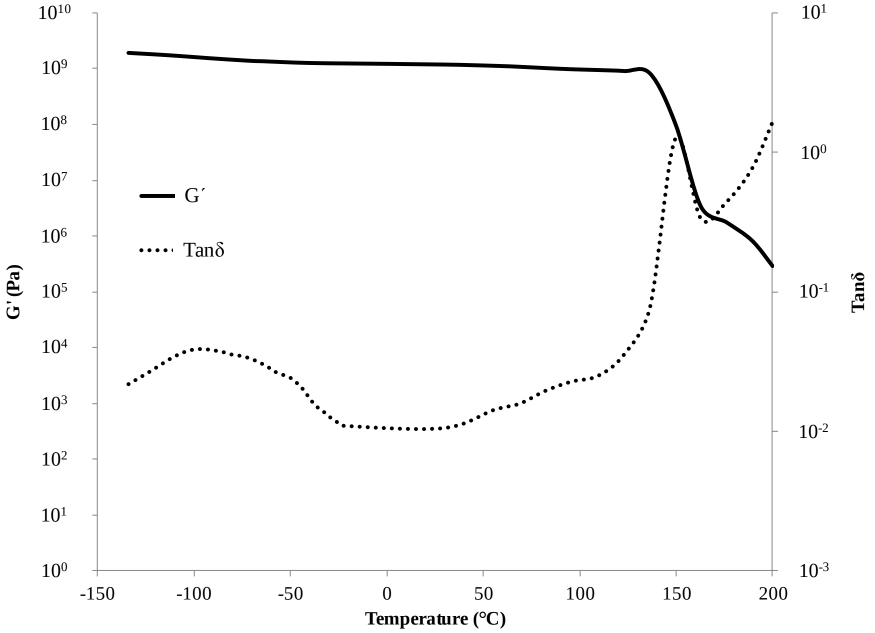

Figure 4.7. PC storage modulus and loss tangent as a function of temperature at 1 Hz.

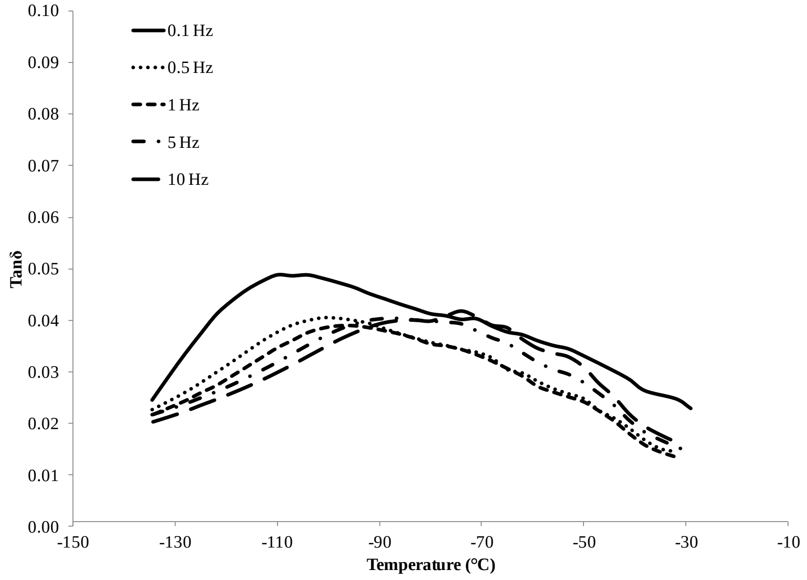

Figure 4.8. Shift in β transition with increasing frequency in PC.

Figure 4.9 shows the dependence of storage modulus on strain rate as a function of temperature (°K) in PC obtained *via* DMA test. As shown in the figure, similar to loss tangent plots shown in Figure 4.8, the α and β transition temperatures increase with increasing strain rate. To find the onset of β restriction, not the peak, the storage modulus plot is decomposed into α and β component according to the DSR procedure described by Mulliken and Boyce [48], discussed in Section 3.1. Figure 4.10 shows the plot of storage modulus separated into their respective α and β components at a particular strain rate. Analytical expression was used to decompose the storage modulus plot into α and β components. From the plot, the onset of β restriction can be easily observed (Onset of β component plot). Now, from Figure 4.8, a shift in β transition of 15.1 °C/decade of strain rate is calculated, which matches well with Mulliken and Boyce [48] (15.3 °C/decade of strain rate for PC). This shift is used to find the range of strain rates in between which the β restriction is activated at room temperature (296 °K). By shifting the plot of onset of β restriction according to the procedure described earlier, the prediction of transition can be found as shown in Figure 4.11. According to the figure, the onset of β restriction can be predicted to occur between strain rates of 2 /s and 20 /s at room temperature for PC.

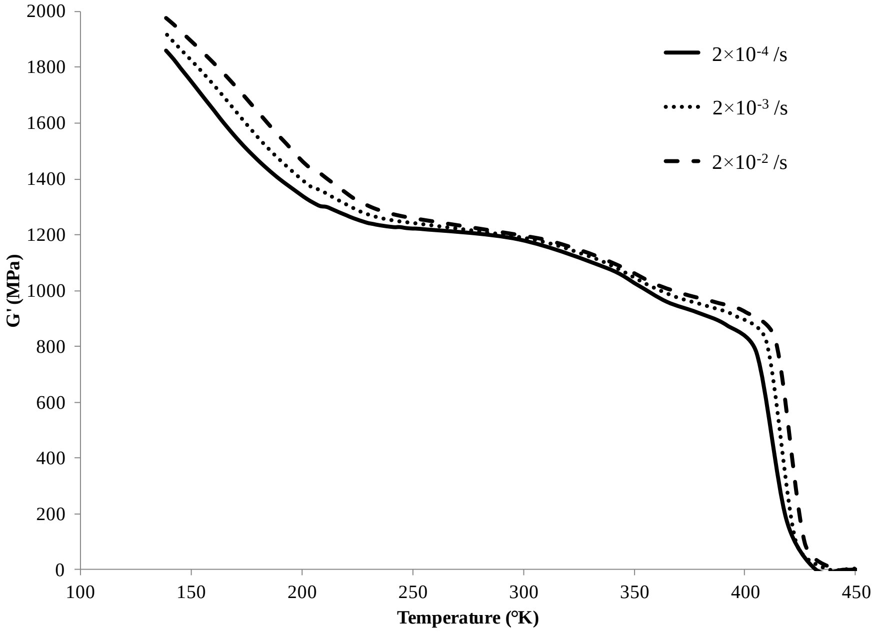

Figure 4.9. Dependence of PC storage modulus on strain rate as a function of temperature (°K).

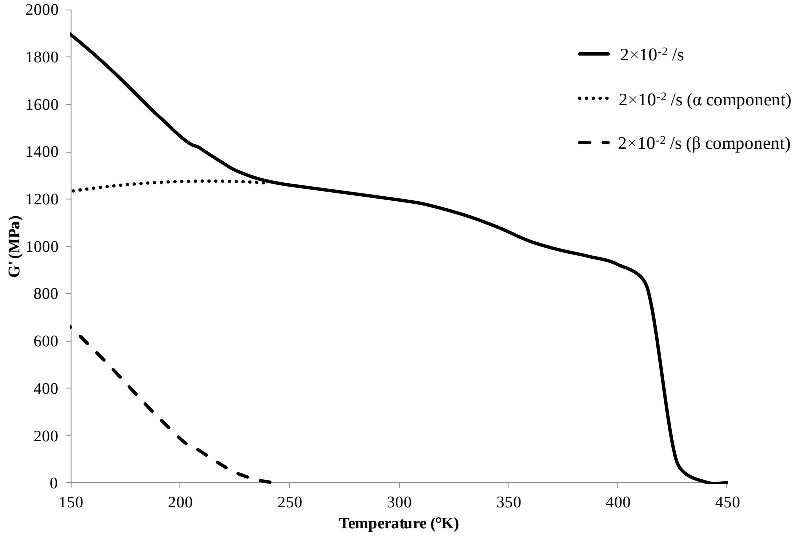

Figure 4.10. Decomposition of PC storage modulus into α and β components at a strain rate of 2×10^{-2} /s.

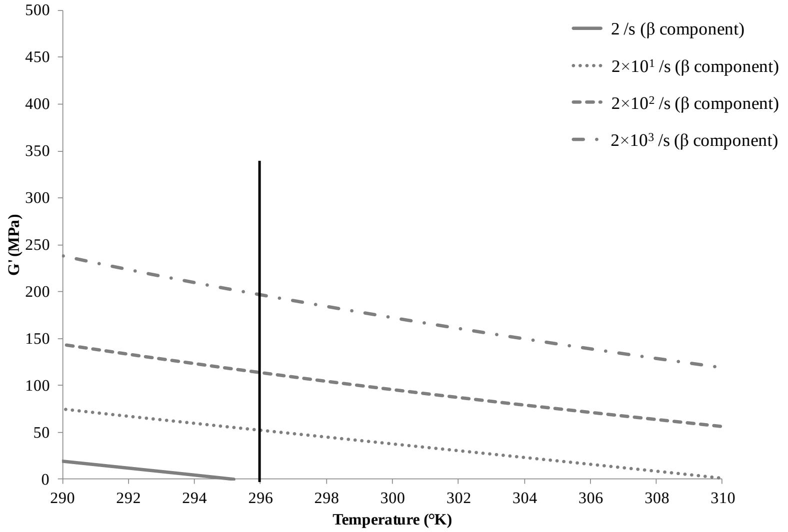

Figure 4.11. Prediction of onset of β restriction in PC (The vertical line denotes room temperature).

From the work done by Bauwens, Bauwens-Crowet and Homès [55-59] on Makrolon PC to describe the rate dependent behavior of amorphous polymer using the multiple rate activated process, the strain rate for activation of β yield process at room temperature can be calculated using Equation 3.8. Using the equation and data provided by Bauwens-Crowet et al. [58] for Makrolon PC, the critical strain rate at room temperature (296 °K) is calculated to be 14.5 /s, which falls within the range calculated in this study. It should be noted that, the PC sample used by Bauwens-Crowet et al. [58] is Makrolon from Bayer as in this study, although the grade is not known in their case (Makrolon 2800, in this study). Even though a smooth rather than sharp transition from single activated process to multiple rate activated process occurs in polymers, the fact that the same Makrlon PC is used in this study and by Bauwens-Crowet et al. [58], the similarities in activation energies for β transition and β yield process and in the critical strain rate for onset of β restriction in both cases suggest that the high strain rate behavior of PC can be extrapolated from the plots obtained using Equations 3.3, 3.4, 3.6, 3.7 and constants value provided by Bauwens-Crowet et al. [58] listed in Table 3.1.

4.3.2.2 Dynamic Mechanical Analysis of SAN

Representative storage moduli and loss tangent plots in logarithmic scale obtained in DMA test for SAN is shown in Figure 4.12. A broad secondary transition or a combination of multiple secondary transitions can be observed in SAN according to the loss tangent plot. Although a distinctive shift in α transition can be observed with increasing frequency or strain rate, no such shift can be observed with increase in strain rate in the broad secondary peak. Figure 4.13 shows the dependence of storage modulus on strain rate as a function of temperature (°K) in SAN obtained *via* DMA test. As shown in the plot, the storage modulus decreases almost linearly with increasing temperature at all three strain rates. No appreciable effect of secondary transition on the storage modulus can be observed in case of SAN by comparing Figure 4.13 (SAN) with Figure 4.9 (PC).

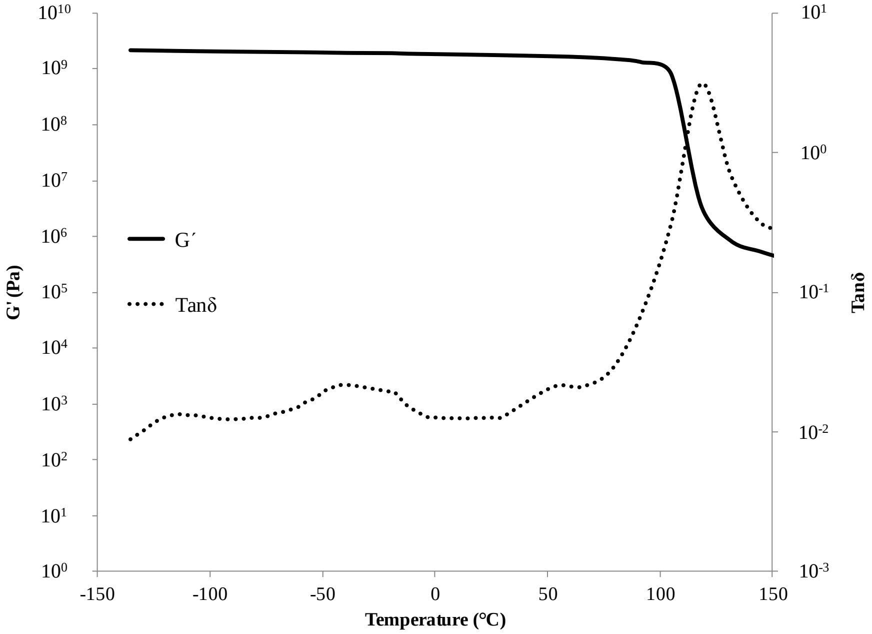

Figure 4.12. SAN storage modulus and loss tangent as a function of temperature at 1 Hz.

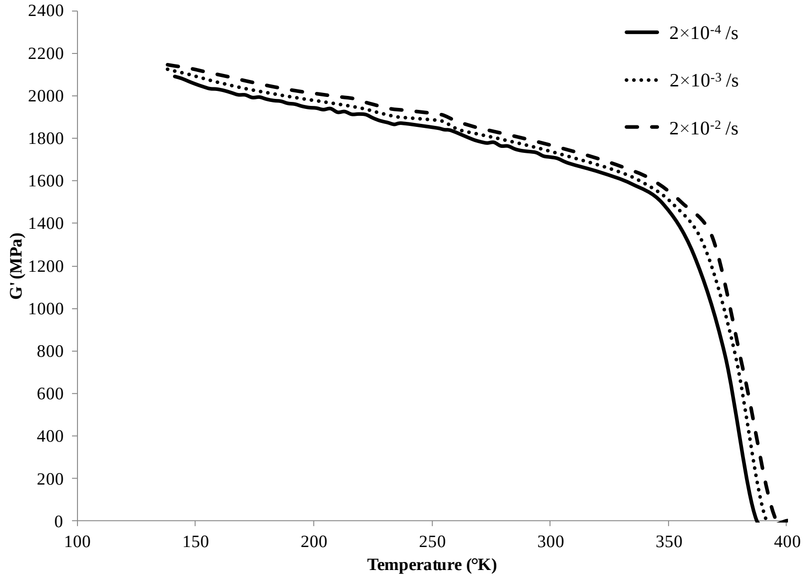

Figure 4.13. Dependence of SAN storage modulus on strain rate as a function of temperature (°K).

Similar storage modulus behavior has been reported in the literature in case of PMMA [48] (Figure 4.14). It was hypothesized that the onset of β restriction occurs at a very low strain rate (10^{-4} /s - 10^{-5} /s) at room temperature. The plot of compressive yield stress as a function of strain rate (Figure 4.15) revealed that indeed the β yield process for PMMA started at a very low strain rate. Thus, a linear dependence of compressive yield stress on logarithm of strain rate from a low strain rate (~ 10^{-2} /s) to a high strain rate can be considered, as shown in Figure 4.15. A similar observation can also be made based on the storage modulus and loss tangent data obtained from DMA tests for SAN in this study. As a result, the linear dependence of yield stress on logarithm of strain rate at low strain rates obtained by plotting the experimental data discussed in Section 4.2.2.2 can be used to predict the behavior at high strain rate in case of SAN.

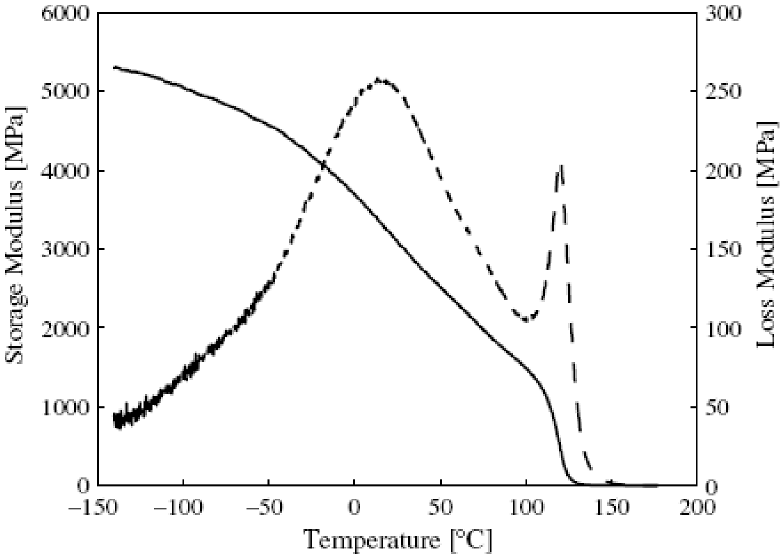

Figure 4.14. Storage modulus (solid line) and loss modulus (dashed line) of PMMA as a function of temperature at 1 Hz [48].

(Figure reprinted from International Journal of Solids and Structures, **43**, Mulliken, A.D., Boyce, M.C., *Mechanics of the rate dependent elastic–plastic deformation of glassy polymers from low to high strain rates*, 1331-1356, Copyright (2006), with permission from Elsevier)

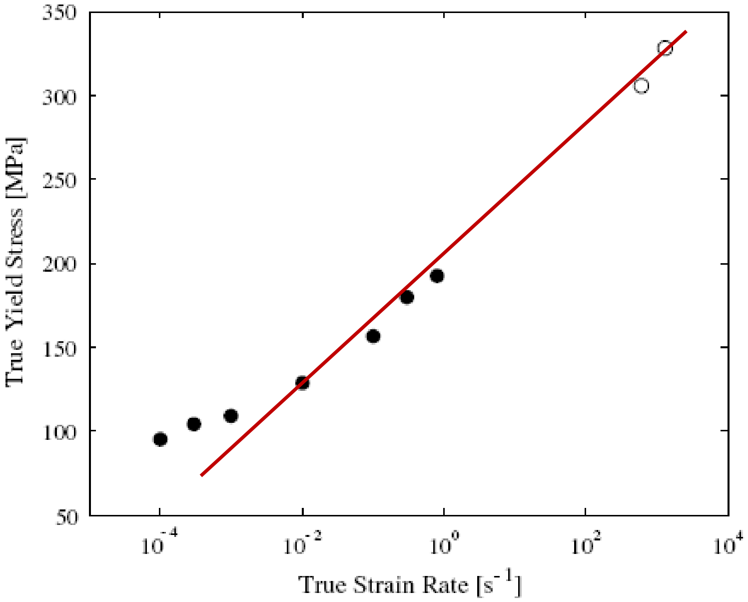

Figure 4.15. True compressive yield stress of PMMA as a function of true strain rate (logarithmic scale) [48].

(Figure reprinted from International Journal of Solids and Structures, **43**, Mulliken, A.D., Boyce, M.C., *Mechanics of the rate dependent elastic–plastic deformation of glassy polymers from low to high strain rates*, 1331-1356, Copyright (2006), with permission from Elsevier)

4.4 Measurement of Surface Friction Coefficient

4.4.1 Measurement Procedure

To determine the coefficient of surface friction, μ at the interface between the model systems and scratch tip, a flat smooth stainless steel tip with 10 mm × 10 mm square area was employed. The RMS Roughness value of the stainless steel flat tip was 225 nm on an area of 525 µm × 700 µm. The flat tip was installed on the scratch machine and tests were conducted under 5 N constant normal load for a distance of 40 mm at a velocity of 100 mm/s. Five tests were conducted for each model polymers to obtain an average value of μ. As discussed earlier, this procedure to measure the coefficient of surface friction is comparable with the method described in literature [43].

4.4.2 Results and Discussion

Figure 4.16 shows the coefficient of friction (COF, μ) measured using the 10 mm × 10 mm stainless steel flat tip for both PC and SAN. An average COF value of 0.6 for PC and 0.45 for SAN system is calculated. It should be noted that, this COF values are higher than the values reported in Section 2.3.3.2. The higher values of COF in this part of study can be attributed to the heat treatment process employed as it eliminates chain orientation, and, thus, producing unoriented surface compared to the oriented surface due to injection molding process discussed in Section 2.3. Since, the surface of both PC and SAN samples can be considered very smooth according to the roughness value reported in Section 4.1, this COF value can be used to describe the frictional behavior at a low pressure in the pressure-dependent frictional model for FEM simulation, to be described later.

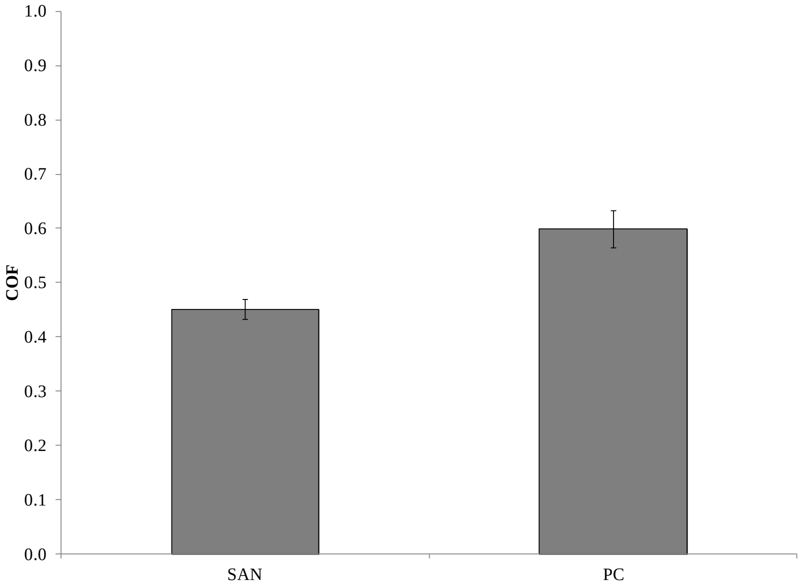

Figure 4.16. Coefficient of friction measured using 10 mm × 10 mm flat tip for the model systems.

4.5 Scratch-induced Deformation

4.5.1 Scratch Test

Scratch tests were carried out according to the ASTM D7027-05/ISO 19252:08 standard [5] by employing a linearly progressive normal load of 1-70 N. A constant scratch speed of 100 mm/s was used for the scratch tests with a scratch length of 100 mm. A stainless steel spherical scratch tip of 1 mm diameter was used to conduct the tests. Five scratch tests were performed on the same plaque.

4.5.2 Microscopic Observation

Immediately after completing the scratch tests, all the samples were scanned using a Keyence® VK9700 violet laser scanning confocal microscope (VLSCM) for high-resolution analysis of the scratch-induced damage mechanisms, as described in Section 2.2.2.4. The scratch depth, shoulder height and scratch width at different locations on the scratch path were measured using the VK Analyzer software. The samples were scanned again after full relaxation (~ 8 months after the scratch test) to measure the percent relaxation or viscoelastic recovery.

4.5.3 Results and Discussion

4.5.3.1 Scratch-induced Deformation in the Model Polymers

Figures 4.17-4.19 show the plots of evolution of residual scratch depth, shoulder height and scratch width of PC as a function of scratch normal load obtained *via* VLSCM. As discussed, the scratches were scanned for the measurement of scratch-induced deformation immediately after the scratch tests, and, consequently, can be considered to involve mostly elastic recovery. The viscoelastic recovery and relaxation behavior during scratch will be discussed later on.

The measurement of scratch-induced deformation in PC was done by scanning at specific points along the scratch path using 20X magnification. The area of analysis using this magnification is ~ 525 μm × 700 μm corresponding to a point. Since the scratch-induced deformation also varies in this area, three measurements at the beginning, in the middle and at the end have been conducted to give an average value and standard deviation (vertical error bar in the figures) of scratch-induced deformation corresponding to a point. Although linearly increasing with scratch length, the scratch normal load has some fluctuation at a particular point. These points are averaged out to give an average value and standard deviation (horizontal error bar in the figures) of normal load corresponding to a point along the scratch path.

As can be seen in the figures, all five scratches show similar scratch-induced deformation highlighting the repeatability and consistency of the scratch testing procedure. Although, the scratch testing was carried out up to scratch normal load of 70 N, the measurement was done in 1-35 N load range since this is the load range quantitative prediction on scratch-induced deformation using FEM is performed.

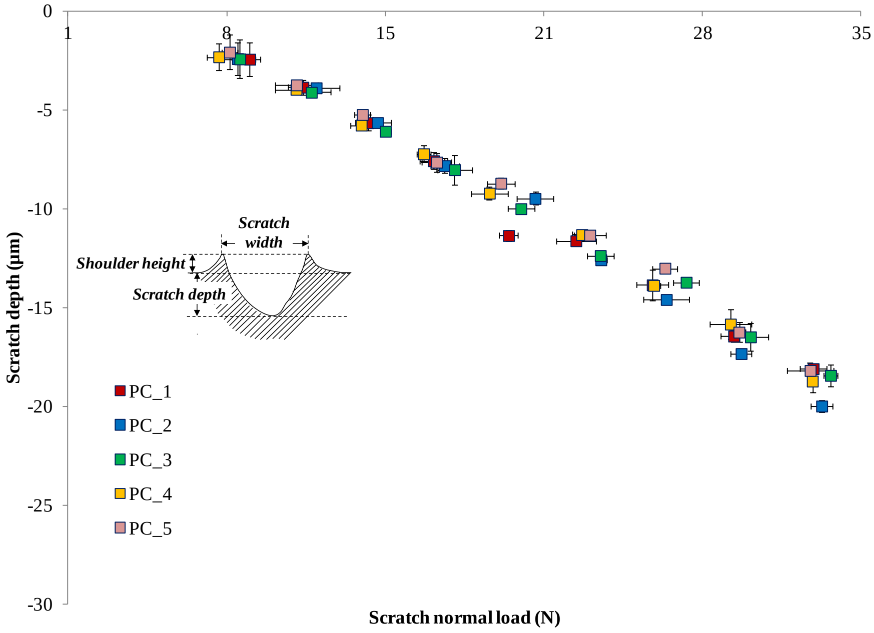

Figure 4.17. Plot of scratch depth as a function of scratch normal load in PC.

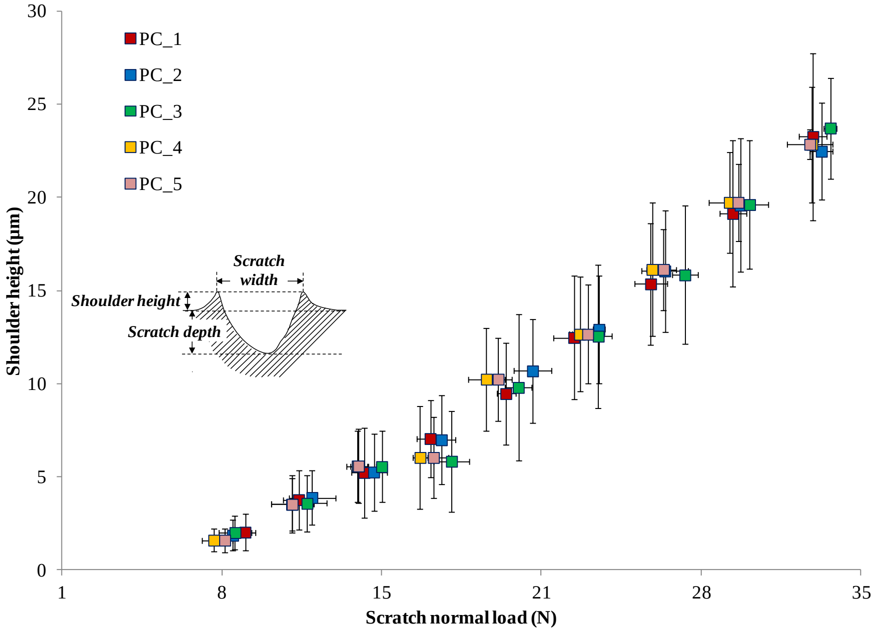

Figure 4.18. Plot of shoulder height as a function of scratch normal load in PC.

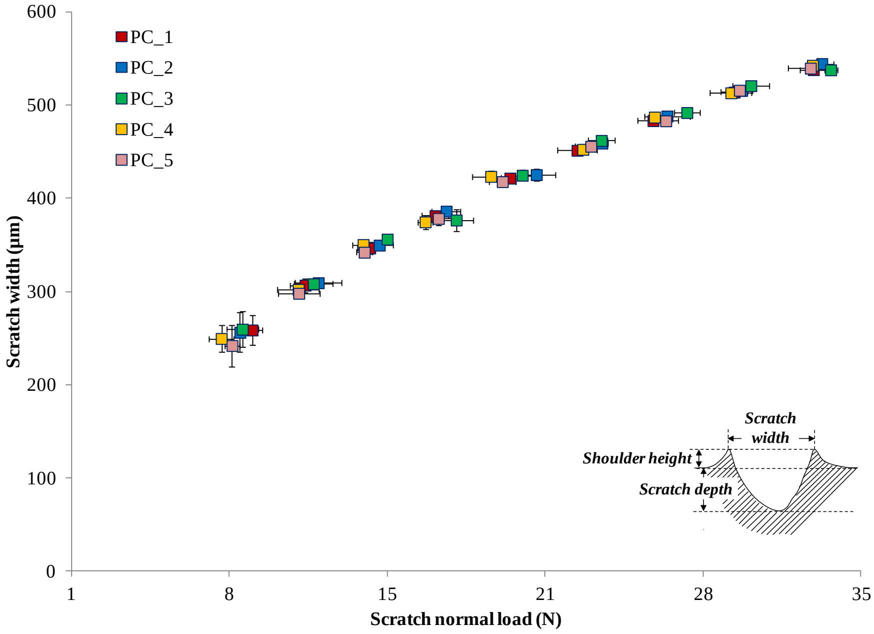

Figure 4.19. Plot of scratch width as a function of scratch normal load in PC.

Figures 4.20-4.22 show the plots of evolution of residual scratch depth, shoulder height and scratch width of SAN as a function of scratch normal load obtained *via* VLSCM. Similar to PC, the scratches were scanned for the measurement of scratch-induced deformation immediately after the scratch tests and, thus, can be considered to involve mostly elastic recovery. Similar procedure as described for PC has been carried out to obtain the average value and standard deviation of scratch-induced deformation and scratch normal load.

As can be seen in the figures, all five scratches show similar scratch-induced deformation highlighting the repeatability and consistency of the scratch testing procedure. For SAN, micro-cracks/crazes formed in the scratch groove along the scratch path at higher loads. Thus, measurement of scratch-induced deformation was done only up to the point of onset of micro-cracking/crazing for all the scratches, and plotted accordingly.

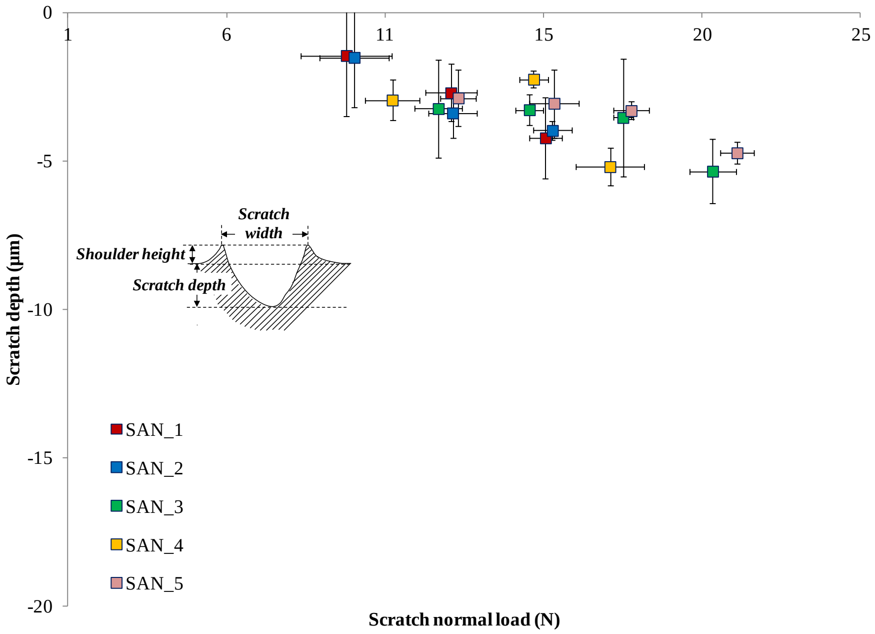

Figure 4.20. Plot of scratch depth as a function of scratch normal load in SAN.

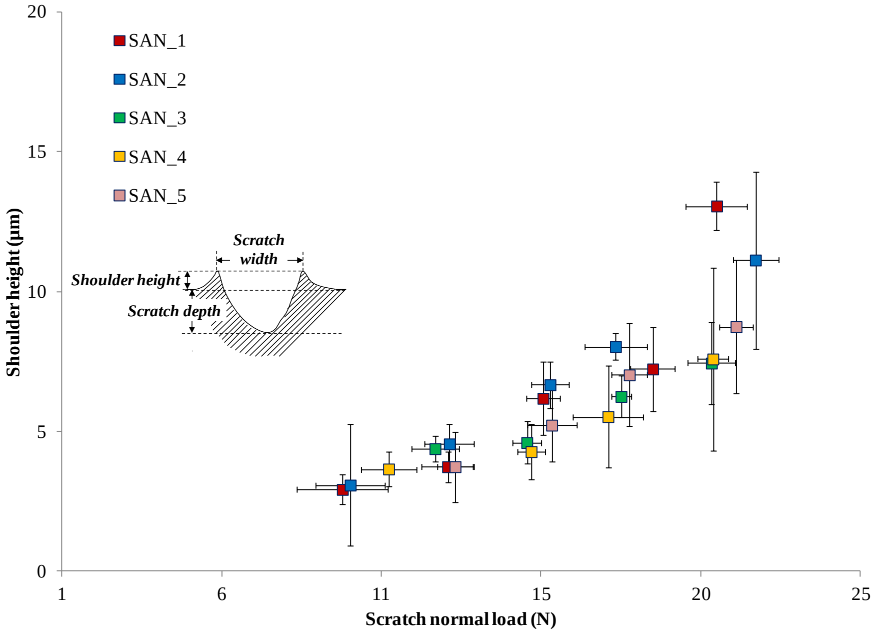

Figure 4.21. Plot of shoulder height as a function of scratch normal load in SAN.

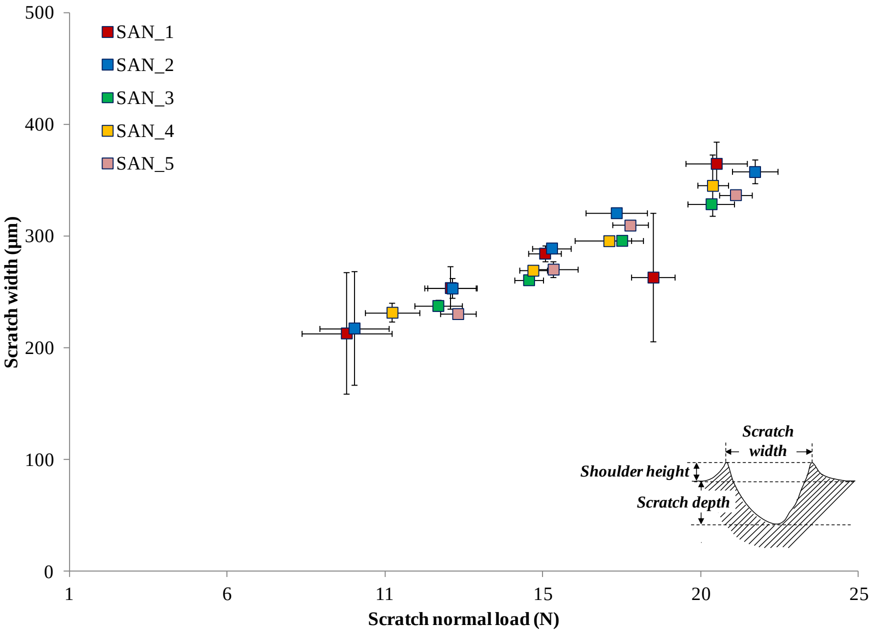

Figure 4.22. Plot of scratch width as a function of scratch normal load in SAN.

It should be noted that a deeper scratch depth and higher shoulder height for both PC and SAN model systems is observed in this part of study compared to the same systems investigated earlier (Section 2.3). In that particular study, no heat treatment was done on the samples and scratch testing and frictional measurement was done along the molding direction. Since the injection-molded specimen has preferred chain orientation along the mold direction, a lower value of coefficient of friction is expected along the chain orientation compared to the unoriented structure due to heat treatment, according to the literature [38, 39]. As a result, a deeper scratch depth and higher shoulder height is observed in this particular work compared to the earlier study.

4.5.3.2 Viscoelastic Recovery

The viscoelastic recovery or percent relaxation of PC and SAN scratch has been investigated by comparing the scratch depth and shoulder height measured right after the scratch test (Figures 4.17, 4.18, 4.20, 4.21) with that measured 8 months after the scratch test. The samples were put in a dessicator after the scratch test and considered to be fully relaxed after this time period. The percent relaxation is calculated using the following equation:

$$\% \, Relaxation = \frac{SD_{residual} - SD_{relaxed}}{SD_{residual}} \times 100 \qquad (4.1)$$

Where, $SD_{residual}$ is the residual scratch-induced deformation (Scratch depth, shoulder height) measured right after the scratch test and $SD_{relaxed}$ is the scratch-induced deformation (Scratch depth, shoulder height) measured after 8 months of the scratch test. Same points along the scratch path were taken for the measurement of viscoelastic recovery. For PC, more than one point at a particular location (~525 µm × 700 µm window) is compared to give an average value and standard deviation. For SAN, only one point at a particular location is considered.

Figures 4.23 and 4.24 show the percent relaxation in scratch depth and shoulder height for PC and SAN, respectively. As can be seen in the figures, in general, the viscoelastic recovery is less than 10% for PC and less than 7% for SAN, which can be considered minor in view of the time required to relax. Also, the percent relaxation in shoulder height is less than that of scratch depth. Furthermore, since both shoulder height and scratch depth show positive percent relaxation, the scratch groove can be considered to flatten with time for both PC and SAN.

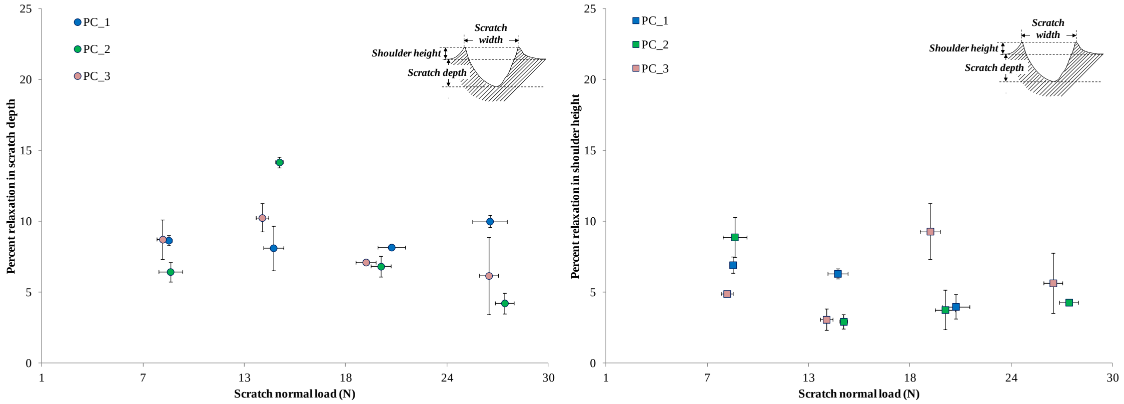

(a) (b)

Figure 4.23. Percent viscoelastic recovery in - (a) Scratch depth; (b) Shoulder height; in PC.

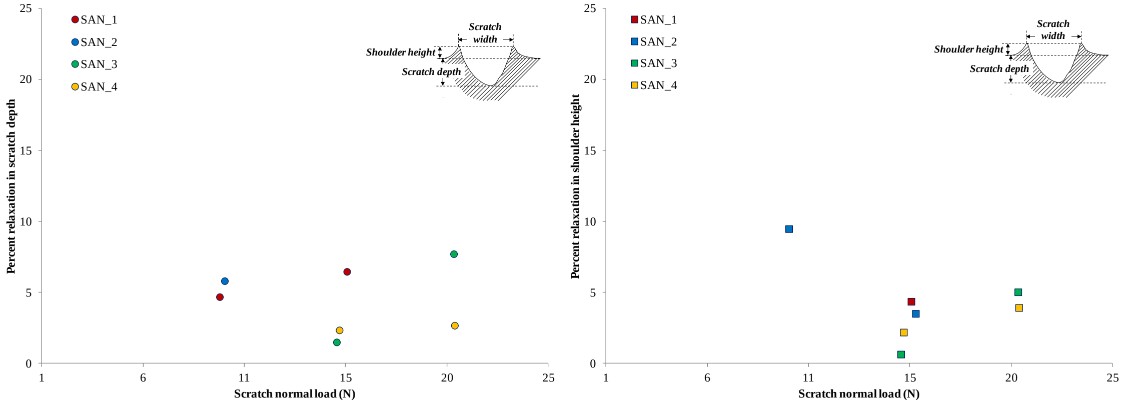

(a) (b)

Figure 4.24. Percent viscoelastic recovery in - (a) Scratch depth; (b) Shoulder height; in SAN.

According to the experimental results, the viscoelastic recovery or percent viscoelastic relaxation can be considered insignificant for both PC and SAN scratch. It should be noted that the percent viscoelastic relaxation calculated in this study is based on the residual scratch depth and shoulder height, which is measured after the polymer recovered elastically. Since polymers in general have considerable amount of elastic recovery, the viscoelastic relaxation/recovery can be considered far more insignificant during the scratch process if instantaneous scratch-induced deformation is considered. Thus, the viscoelastic contribution is neglected in the constitutive model used for quantitative prediction of scratch-induced deformation *via* FEM.

CHAPTER V

FEM MODEL FOR QUANTITATIVE ANALYSIS

This chapter discusses the constitutive behavior, frictional relation, model geometry and loading conditions employed in the FEM simulation for quantitative prediction of scratch behavior in the model polymers.

A commercial finite element package ABAQUS® [40] (V. 6.9) was employed to conduct 3-D FEM simulation of scratch behavior of PC and SAN model polymers, using the supercomputing facility at Texas A&M University. The study focuses on simulating the development of residual shoulder height, scratch depth and scratch width along the scratch path due to the application of linearly increasing normal load according to the ASTM standard for scratch testing [5]. It should be noted that, the development of micro-cracking, crazing and fish-scale formation in the scratch groove during the scratch process was not included in the FEM simulation in this study. Also, as discussed earlier, since there is negligible thermal effect on scratch behavior of polymers at the scratch speed employed in the experiment and load range selected for FEM simulation, the temperature dependent constitutive behavior was not considered in this simulation. Furthermore, as the viscoelastic effect on scratch behavior of SAN and PC model systems has shown to be insignificant (Section 4.5.3.2); viscoelasticity was not considered in this numerical modeling. Since the scratch process is essentially dynamic in nature, dynamic stress analysis with explicit scheme was employed in the FEM simulation. The default automatic stable time increment in ABAQUS®, which has shown to ensure good accuracy of the numerical analysis [2], was employed. Double precision calculation was used in the FEM simulation to alleviate any truncation error introduced in the analysis.

5.1 Constitutive Model

To perform a realistic and accurate FEM simulation of polymer scratch, it is required that an appropriate constitutive relation is prescribed, which takes into account the rate and pressure dependent yielding of polymers. Some of the most common yield criteria used for elasto-plastic materials are Tresca, von Mises, Mohr-Coulomb and Drucker-Prager. By definition, the Tresca criterion is pressure insensitive, and, thus, particularly relevant to the modeling of metals in which the influence of hydrostatic pressure on yielding is considered to be negligible. Similar to the Tresca criterion, the von Mises criterion is also pressure-insensitive and both Tresca and von Mises criteria are applicable to the materials that essentially have same behavior in tension and compression. Consequently, both Tresca and von Mises yielding criteria are not suitable to describe the yielding behavior of polymers.

For materials whose yield behavior is strongly dependent on hydrostatic pressure (e.g., soils, rocks, concrete, etc.), a classical example of pressure-sensitive law is given by the Mohr-Coulomb. The Mohr-Coulomb criterion is based on the assumption that the macroscopic plastic yielding is essentially the result of frictional sliding between material particles [92]. According to the Mohr-Coulomb yield criterion, plastic yielding begins when, on a plane in the body, the shearing stress, τ, and the normal stress, σ_n, reach the critical combination [92]:

$$\tau = c - \sigma_n Tan\varphi \tag{5.1}$$

Where c is the cohesion and φ is the angle of internal friction or frictional angle. σ_n is assumed positive in tension. Both Tresca and Mohr-Coulomb yield criteria coincide when $\varphi = 0$, i.e., in the absence of internal friction. Drucker and Prager [93] proposes a criterion based on smooth approximation to the Mohr-Coulomb law by modifying the von Mises criterion to included pressure-sensitive yield behavior. According to the Drucker-Prager criterion, plastic yielding begins when the J_2 invariant of the deviatoric stress tensor and the hydrostatic pressure, p, reach a critical combination [92]:

$$\sqrt{J_2(s)} + \eta p = c \tag{5.2}$$

Where η and c are material parameters. The von Mises cylinder is recovered from the Drucker-Prager criterion when $\eta = 0$. Figure 5.1 shows the yield surface in principal stress space for the Drucker-Prager criterion.

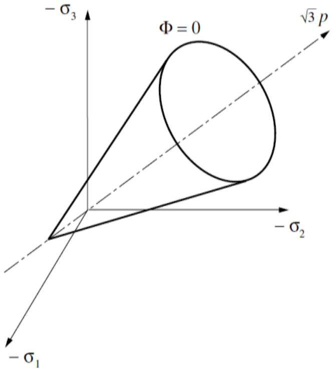

Figure 5.1. Yield surface in principal stress space for Drucker-Prager criterion [92].
(Figure reprinted from Computational Methods for Plasticity: Theory and Applications, Neto, E.A.d.S., Peri´c, D., Owen, D.R.J., *The mathematical theory of plasticity*, 139-190, Copyright © 2008 John Wiley and Sons, with permission from John Wiley & Sons, Inc.)

The Mohr-Coulomb model assumes that yielding/failure is independent of the intermediate principal stress, but the Drucker-Prager model does not [40]. The Drucker-Prager yield surface is smooth compared to that of Mohr-Coulomb, which makes it more suitable for computer implementation [94]. As a result, the Drucker-Prager criterion has long been employed to predict and analyze the deformation of polymers in different scenarios with moderate success [95-100].

Along with the yield criterion, a plastic flow rule has to be chosen. A plasticity model can be classified as “associative” if the yield function is taken as the flow potential. Any other choice of flow potential is considered “non-associative”. Associative plastic model simply implies that the plastic strain rate is a tensor normal to the yield surface in the space of stresses. In non-associative models, the plastic strain rate is not normal to the yield surface in general. As discussed earlier, experimental studies have shown that the plastic flow of polymers is pressure sensitive and plastic dilatancy is generally insignificant [68-71], and, thus, the flow in polymers is generally non-associative [99].

In this study, Extended Drucker-Prager model [40], a built-in inelastic material model in ABAQUS®, was employed to describe the constitutive relationship of the PC and SAN model systems. The extended Drucker-Prager model in ABAQUS® allows isotropic hardening and/or softening of the material. As discussed in Section 3.2, since polymers in general show linear dependency on hydrostatic pressure, the built-in linear Drucker-Prager model was chosen. Figure 5.2 shows the yield surface of the linear Drucker-Prager model in the meridional plane [40].

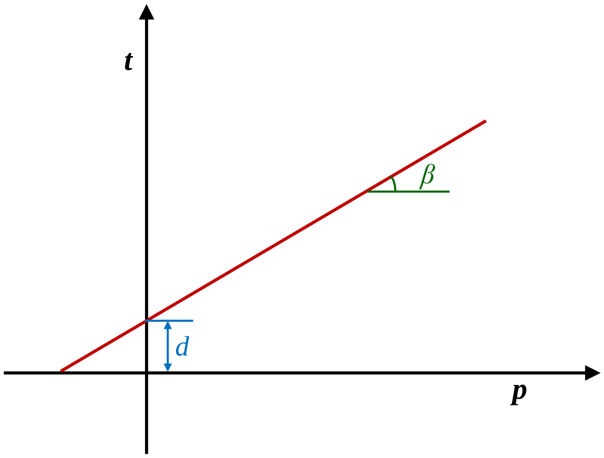

Figure 5.2. Yield surface in meridional plane for linear Drucker-Prager model [40].
(Figure adopted from *ABAQUS® Analysis User's Manual, Version 6.9*, available from: www.simulia.com)

The yield criterion for the linear Drucker-Prager model can be written as [40]:

$$F = t - pTan\beta - d = 0 \tag{5.3}$$

Where, $t = \frac{1}{2}q\left[1 + \frac{1}{K} - \left(1 - \frac{1}{K}\right)\left(\frac{r}{q}\right)^3\right]$, β is the slope of the linear yield surface in the meridional plane and is known as friction angle of the material, d is the intercept and known as the cohesion of the material, K is the ratio of the yield stress in triaxial tension to the yield stress in triaxial compression, p is the equivalent pressure stress ($p = -\frac{1}{3}trace(\boldsymbol{\sigma})$), q is the Mises equivalent stress ($q = \sqrt{\frac{3}{2}(\boldsymbol{S}:\boldsymbol{S})}$), $\boldsymbol{S}$ is the deviatoric stress ($\boldsymbol{S} = \boldsymbol{\sigma} + p\boldsymbol{I}$), and r is the third invariant of deviatoric stress ($r = \left(\frac{9}{2}\boldsymbol{S} \cdot \boldsymbol{S}:\boldsymbol{S}\right)^{\frac{1}{3}}$). When hardening is defined in uniaxial compression, the linear yield criterion precludes friction angle, $\beta > 71.5°$. If K=1, the yield stress in triaxial tension and compression is same and the von Mises circle in deviatoric principal stress plane is recovered. For convexity of yield surface, $0.778 \leq K \leq 1$ [40]. When triaxial experimental data is not directly available, ABAQUS® provides an option to match Mohr-Coulomb and linear Drucker-Prager model parameters for materials with low frictional angle so that both models provide the same failure definition in triaxial compression and tension. In that case:

$$K = \frac{1}{1+\frac{1}{3}Tan\beta} \tag{5.4}$$

The flow potential is defined as [40]: $G = t - pTan\psi$, where ψ is the dilation angle in the $p - t$ plane.

The rate and pressure sensitive mechanical behavior of PC and SAN model systems was described using the linear Drucker-Prager model provided in ABAQUS®. The yield stress and hardening behavior in uniaxial compression at different strain rates using piece-wise linear true stress-strain plot was used for that purpose. ABAQUS® uses linear interpolation for the values between the data given. For yield stress of PC, as discussed earlier, at low strain rate, experimental data obtained in uniaxial compression test was provided. To provide medium to high strain rate behavior in uniaxial compression, extrapolation of Bauwens-Crowet et al. [58] data was used as shown in Figure 5.3a. The post-yield/hardening behavior of PC in uniaxial compression, reported in the literature and also in this study, showed to be independent of strain rate. Thus, the post-yield behavior at different strain rates were given by increasing the stress and strain similar to the increment in yield stress and yield strain with strain rates as shown in Figure 5.3b. For SAN, as discussed in Section 4.3.2.2, the high strain rate behavior was predicted using the linear dependency of compressive yield stress on logarithm of strain rate obtained experimentally for low strain rates (Figure 5.4a). The post-yield behavior of SAN at different strain rates was given following the similar procedure described for

PC as shown in Figure 5.4b. In both PC and SAN, yield strain was assumed to follow the experimental data obtained at lower strain rates (Figure 4.2b and 4.5b).

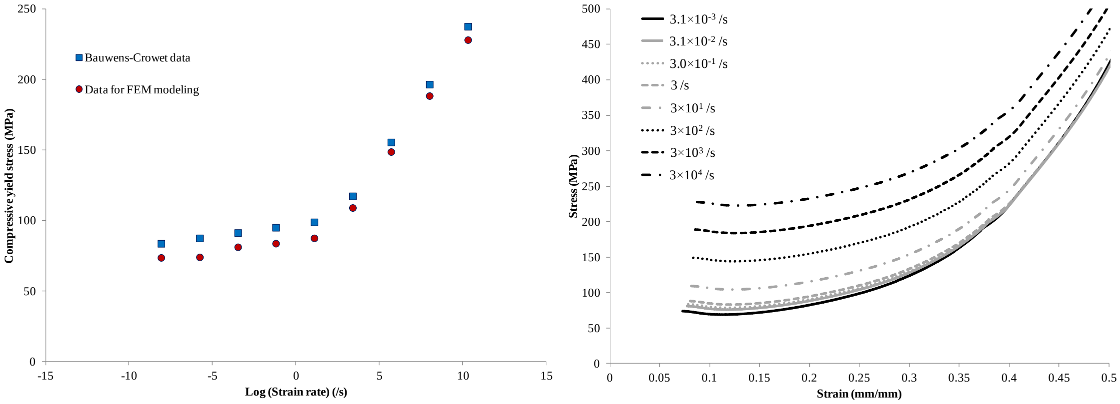

(a) (b)

Figure 5.3. PC - (a) Yield stress; and (b) Post-yield behavior; in uniaxial compression used for FEM modeling.

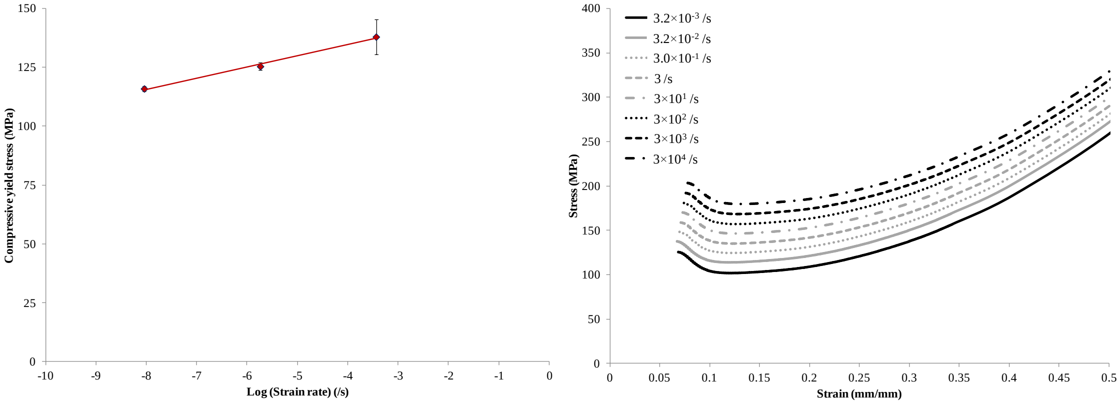

(a) (b)

Figure 5.4. SAN - (a) Yield stress; and (b) Post-yield behavior; in uniaxial compression used for FEM modeling.

There are three parameters to be defined in order to describe the pressure dependency using the linear Drucker-Prager model in ABAQUS®, namely, the slope of the linear yield surface in the meridional plane or material friction angle, β; ratio of the yield stress in triaxial tension to the yield stress in triaxial compression, K; and the dilation angle, ψ [40]. To calculate β, uniaxial tension test data is required. For yield stress of PC, experimental data obtained in uniaxial tension test at low strain rates was used, and, extrapolation of Bauwens-Crowet et al. [58] data was used to obtain medium to high strain rate data. The yield stress data in uniaxial compression and tension was used to calculate the value of β. Using the value of β, K was calculated using Equation 5.4. The dilation angle, ψ was assumed to be zero since, as discussed in Section 3.2, polymers have shown insignificant plastic dilation. Since $\beta \neq \psi$, non-associative flow is considered in this study following the general behavior of polymers. Now, since β and K are obtained from yield stress values in tension and compression, which are rate dependent, these values also vary with strain rate. But the built-in ABAQUS® linear Drucker-Prager model has the option for defining only one value for β and K. As a result, the values of β and K were provided at an average strain rate which the polymer surface would experience during scratch using Equation 3.1 (For PC ~ 480 /s, for SAN ~ 550 /s). Since the uniaxial compression data was used to describe the mechanical behavior and it has been shown, in Section 2.2, that tensile behavior has little influence on scratch depth and shoulder height formation during scratch process, this assumption is considered reasonable. For SAN, the calculation is more complicated since it shows brittle behavior in tension and the tensile strength remains almost unchanged with increasing strain rate. Thus, for SAN, the tensile strength value was used along with compressive yield stress to calculate β and K. In this process, the calculated value of K

went below the requirement of convexity of yield surface ($0.778 \leq K \leq 1$). So, the value of K was assumed to be 0.78 to meet the requirement and β was adjusted accordingly as prescribed [40]. Table 5.1 lists the values of the parameters of linear Drucker-Prager model used in the FEM simulation in this study.

Table 5.1. Values of linear Drucker-Prager model used in the FEM simulation.

Parameter	PC	SAN
β	27.13º	40.24º
K	0.85	0.78
ψ	0	0

Linear elasticity is considered to describe the elastic behavior of PC and SAN model systems. The secant modulus, calculated based on the yield stress and yield strain in unixial compression, was used to describe the elastic behavior. Since the difference in tensile and compressive modulus can be considered minimal according to the experimental observation (Section 4.2.2), same uniaxial tensile and compressive modulus was considered at all strain rates. The built-in ABAQUS® linear Drucker-Prager model provides the option to describe rate independent modulus only. As a result, the secant modulus at an average rate which the polymer surface is expected to experience during scratch using Equation 3.1 (For PC ~ 480 /s, for SAN ~ 550 /s) is used for both PC and SAN. As has been pointed out in the literature [9, 31] that the modulus in the range of 1.65 GPa - 4 GPa has negligible effect on scratch depth, this assumption is deemed reasonable since the rate dependent secant moduli at the strain rates considered in this study fall within that range for both PC and SAN. Table 5.2 lists the secant modulus and Poisson's ratio values used in this study for FEM modeling.

Table 5.2. Modulus and Poisson's ratio values used in the FEM simulation.

	PC	SAN
Modulus, GPa	1.86	2.45
Poisson's ratio	0.37	0.35

5.2 Contact Model

To define the contact between the rigid spherical tip and polymer substrate during the scratch process, finite sliding contact pair algorithm in ABAQUS® was used. Pure master-slave contact algorithm was employed where the tip is considered to be rigid and the polymer substrate is considered to be deformable.

To define the frictional behavior of the interacting surfaces, isotropic Coulomb friction model provided by ABAQUS® was used. This friction model allows defining friction coefficient as a function of contact pressure. The coefficient of adhesive friction was included in the FEM model based on Equation 3.13. As discussed in Section 3.3, the shear yield stress can be considered independent of strain rate, and, thus, the shear yield stress at low strain rate can be used to calculate coefficient of adhesive friction. To calculate the shear yield stress, the pressure dependent yielding plot constructed based on the uniaxial tension and compression data (Section 4.2.2) at a strain rate of ~ 3.1×10^{-3} /s was used. A pressure dependent shear yield stress plot was generated using the relation: $\tau_y = \frac{\sigma_y}{\sqrt{3}}$. Since this plot is essentially shear yield stress *vs.* hydrostatic pressure and the input in friction model is contact pressure dependent, the slope of this pressure dependent shear stress plot was divided by 3 and is taken as the pressure coefficient, α. The shear stress value when pressure is zero is taken as τ_0. Although, SAN shows brittle behavior in tension and Equation 3.13 is generally applicable for ductile polymers, similar procedure was applied to obtain coefficient of adhesive friction data to include in the FEM model for SAN. Table 5.3 lists the values of the parameters calculated from pressure dependent uniaxial data.

Table 5.3. Values used for calculating coefficient of adhesive friction using Equation 3.13.

	PC	SAN
τ_0, MPa	38.32	51.73
α	0.06	0.16

Using the pressure dependent coefficient of adhesive friction values obtained from Equation 3.13 and Table 5.3, the friction model for FEM simulation was described. Figure 5.5 shows the pressure dependent friction model used in the simulation of PC and SAN. The coefficient of friction values obtained experimentally for PC and SAN using the flat stainless steel tip (Section 4.4) were used as an upper limit for coefficient of adhesive friction in the friction model by assuming that the values obtained were at low pressure as discussed in Section 4.4.

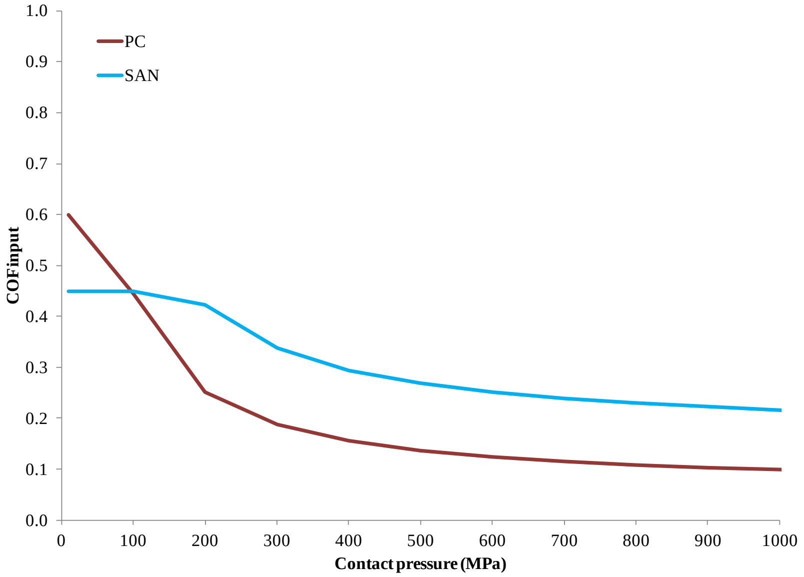

Figure 5.5. Friction model used in the FEM simulation.

5.3 FEM Model Geometry, Boundary and Loading Conditions

The FEM computational domain used in this study to perform numerical analysis was the same as Figure 2.1 except finer meshing was used in this study. A mesh with 512 elements along the critical length (A-B) was chosen in this study rendering an element dimension of 22.8 µm × 28.1 µm × 33.3 µm. This particular meshing was chosen based on the investigation on effect of meshing on scratch-induced deformation to find an optimum meshing that would provide sufficient accuracy with less computation time required, discussed in Appendix A. The model geometry and boundary conditions applied were the same as described in Section 2.1.1.

The FEM simulation of scratch deformation was divided into three steps as shown in Figure 2.2 and discussed in Section 2.1.1. The difference between instantaneous scratch depth and the amount of scratch depth recovered due to elastic recovery is denoted as scratch depth (Residual scratch depth) in this simulation work. As the half model was used in this simulation due to symmetry condition, the normal load applied on the scratch tip during the simulation was half the actual value of the normal load. To save computation time of the numerical simulation, the tip moves over a length of 12 mm at a constant scratch speed of 10 m/s was specified in the numerical simulation. The rate dependent constitutive relationship was scaled accordingly (e.g., data corresponding to a strain rate of 3 /s was given as 300 /s) to simulate the scratch behavior at 100 mm/s scratch speed. The validity of the usage of this method was checked and confirmed, and is presented in the appendices.

CHAPTER VI

RESULTS AND DISCUSSION ON QUANTITATIVE MODELING

This chapter compares the numerical results based on the FEM model discussed in Chapter V with the experimental findings. The results on quantitative prediction of PC and SAN scratch behavior using the FEM model is summarized and discussed. Some of the simulation aspects such as effect of meshing, scratch speed and corresponding scaling of the constitutive relationship, difference in load gradient in the FEM analysis has been studied and the findings are summarized in the appendices.

6.1 Comparison of FEM Simulation and Experiment for Scratch Behavior of PC

Figures 6.1-6.3 show the comparison of FEM simulation and experiment on residual scratch depth, shoulder height and scratch width formed during the scratch process in PC. As shown in the figures, the scratch depth prediction using FEM matches well with the experiment. For shoulder height and scratch width, the FEM simulation predicts well until around 21 N. Beyond that, the FEM under-predicts the shoulder height and scratch width formation during scratching of PC. It should be noted that, in an earlier study [2] it has been shown that at higher loads the formation of scratch groove is not only from the elastic recovery of the scratch groove but has an augmented effect because of the material displacement from the front of scratch tip towards the side. This displaced material added on to the shoulder height formed due to elastic recovery of the scratch groove, which may be the primary reason for discrepancy between FEM simulation and experiment in shoulder height and scratch width at higher loads. The topographical images of the side of scratch groove obtained *via* VLSCM for PC showed increase in surface roughness with increasing normal load, which also corroborates the fact that material in front of scratch tip is indeed moved towards the side. Since, the Lagrangian analysis used in the FEM simulation is unable to simulate the bulk material movement, the discrepancy at higher load in case of shoulder height and scratch width is expected. Nevertheless, FEM simulation of scratch behavior of PC shows reasonable success in predicting the real life scenario.

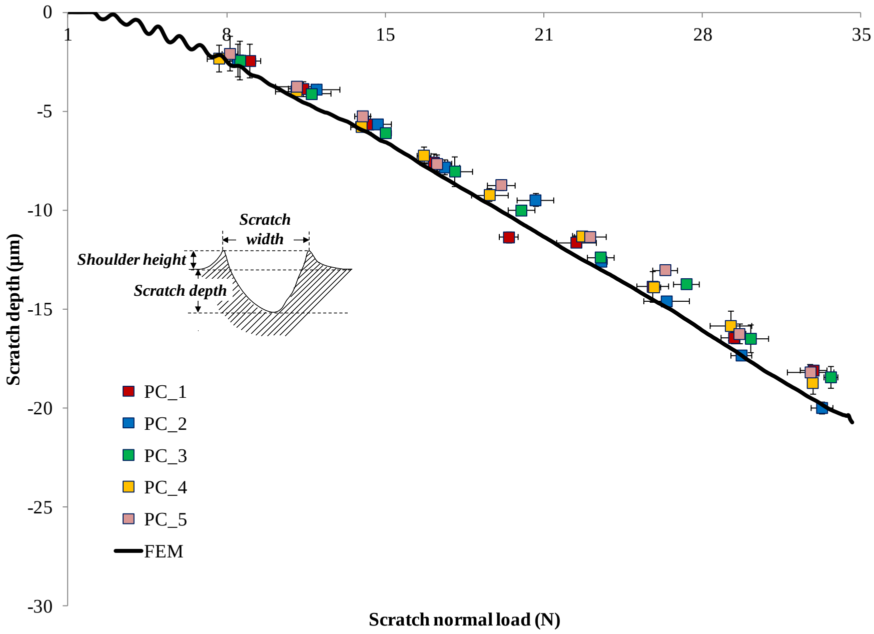

Figure 6.1. Comparison of FEM simulation and experiments on scratch depth evolution as a function of scratch normal load for PC.

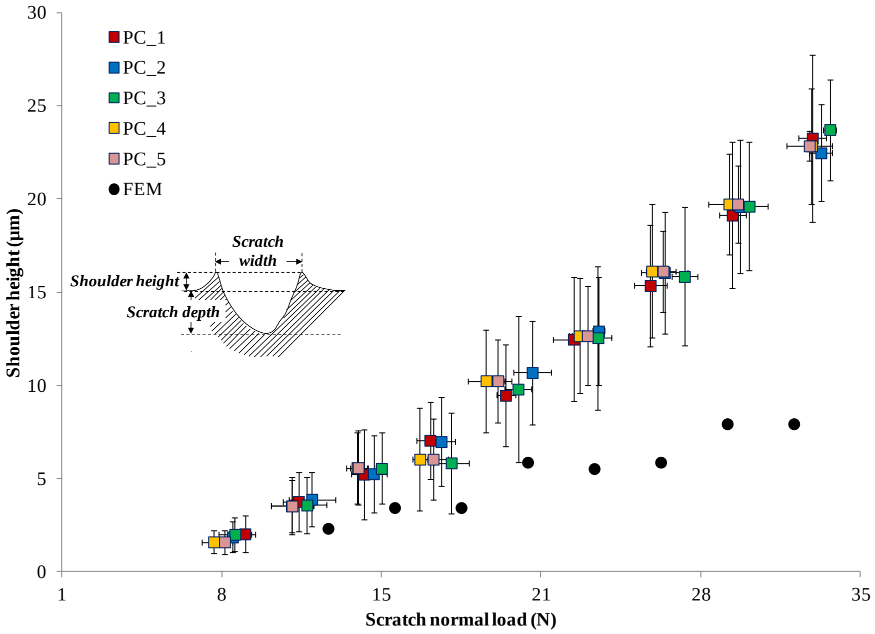

Figure 6.2. Comparison of FEM simulation and experiments on development of shoulder height as a function of scratch normal load for PC.

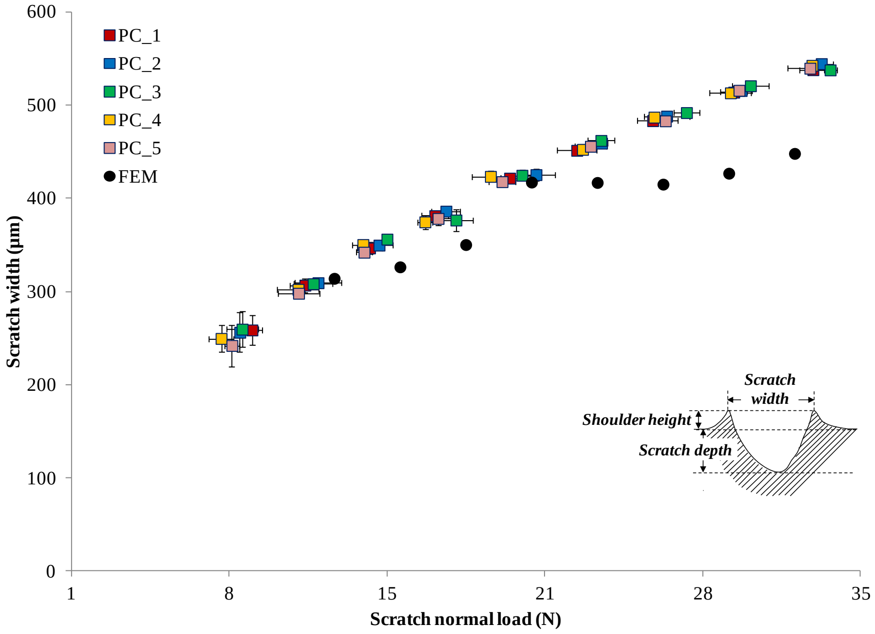

Figure 6.3. Comparison of FEM simulation and experiments on development of scratch width as a function of scratch normal load for PC.

Figure 6.4 shows the comparison of scratch coefficient of friction (SCOF) obtained during experiment ($SCOF = \frac{F_t}{F_n}$) for PC with the friction value obtained from FEM simulation by adding the coefficient of adhesive friction and coefficient of friction due to deformation using Equation 3.10. The coefficient of friction due to deformation is calculated using both Equations 3.14 and 3.15. The contact radius, a, required for the equations is calculated using the following relation:

$$a = \sqrt{2dR - d^2} \tag{6.1}$$

Where, R is the radius of the scratch tip and d is the instantaneous scratch depth obtained *via* FEM simulation.

As pointed out earlier, this method of dividing the friction coefficient is generally applicable for ductile polymers, which is in this case. As shown in the figure, the FEM simulation matches quite well with the experiment. It should be noted that, as discussed earlier, the calculation of coefficient of friction due to deformation is simplistic and also there might be an interaction between adhesion and deformation part of friction which the hypothesis did not take in to account. Nevertheless, by employing the simplistic method of calculating frictional value using Equation 3.10, FEM simulation predicts the SCOF quite reasonably.

Figure 6.5 shows the instantaneous scratch depth and residual scratch depth (or scratch depth) obtained *via* FEM simulation and the percent elastic recovery calculated in case of PC. As shown in the figure, the percent elastic recovery decreases with increasing normal load, but there is an elastic recovery of ~ 70% calculated at scratch normal load of 35 N. Comparing this result with the viscoelastic recovery reported in

Section 4.5.3.2 based on the residual scratch depth, the viscoelastic recovery is considered insignificant during the scratch process and is reasonable not to include in the constitutive relationship for FEM modeling.

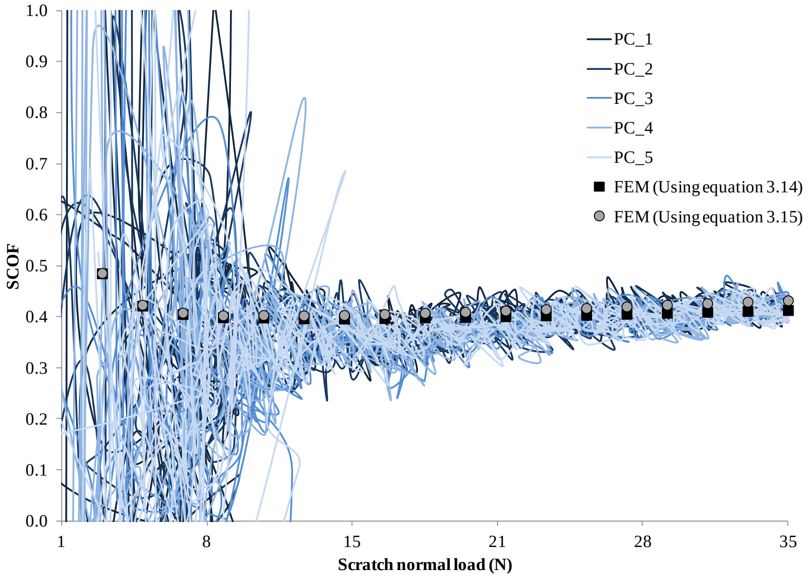

Figure 6.4. Comparison of scratch coefficient of friction (SCOF) obtained *via* experiments with development of friction calculated using FEM simulation for PC.

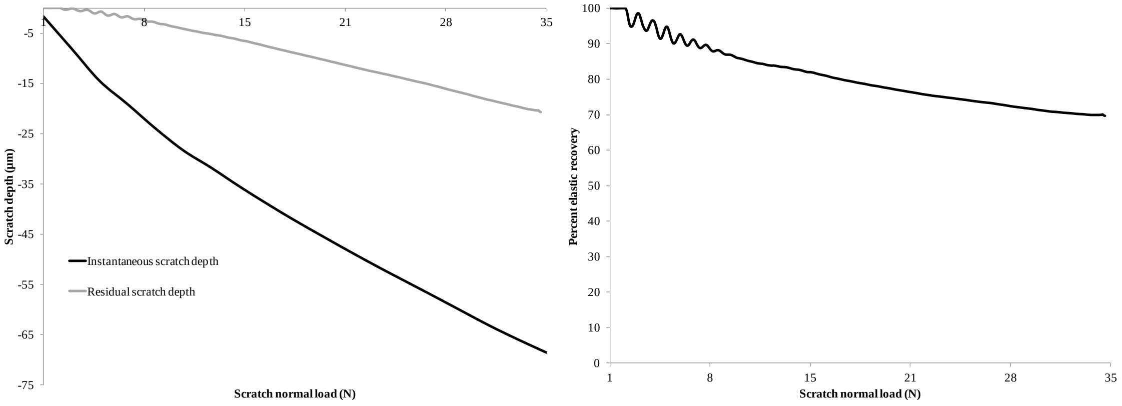

(a) (b)

Figure 6.5. FEM simulation findings on - (a) Instantaneous and residual scratch depth; and (b) Percent elastic recovery; for PC.

6.2 Comparison of FEM Simulation and Experiment for Scratch Behavior of SAN

Figures 6.6-6.8 show the comparison of FEM simulation and experiment on residual scratch depth, shoulder height and scratch width formed during the scratch process in SAN. As shown in the figures, the scratch depth and scratch width prediction using FEM matches well with the experiment. For shoulder height, similar reasoning as discussed earlier based on a previous study [2] can be applied to explain the discrepancy in FEM simulation and experiment for SAN. As a whole, FEM simulation of scratch behavior of SAN shows reasonable success in predicting the behavior observed experimentally.

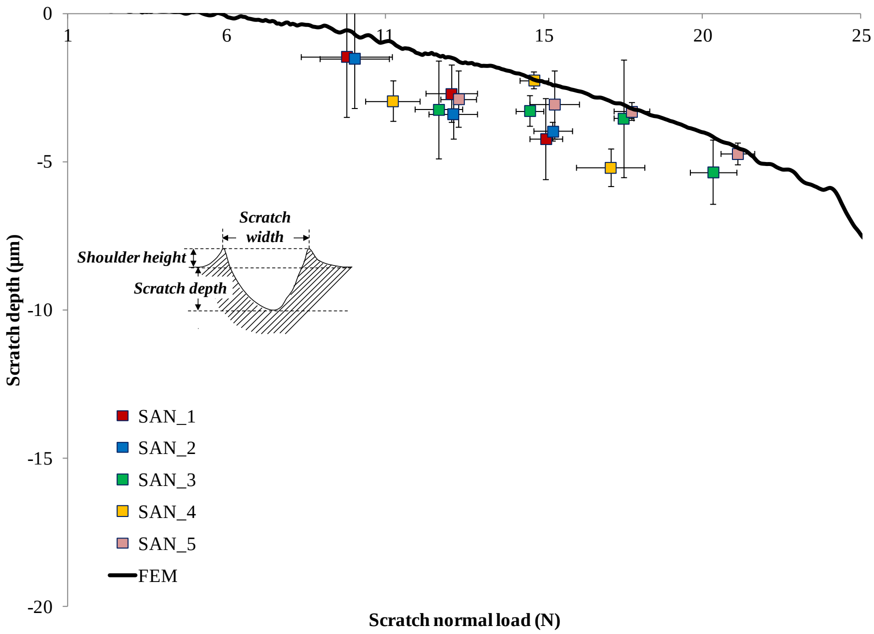

Figure 6.6. Comparison of FEM simulation and experiments on scratch depth evolution as a function of scratch normal load for SAN.

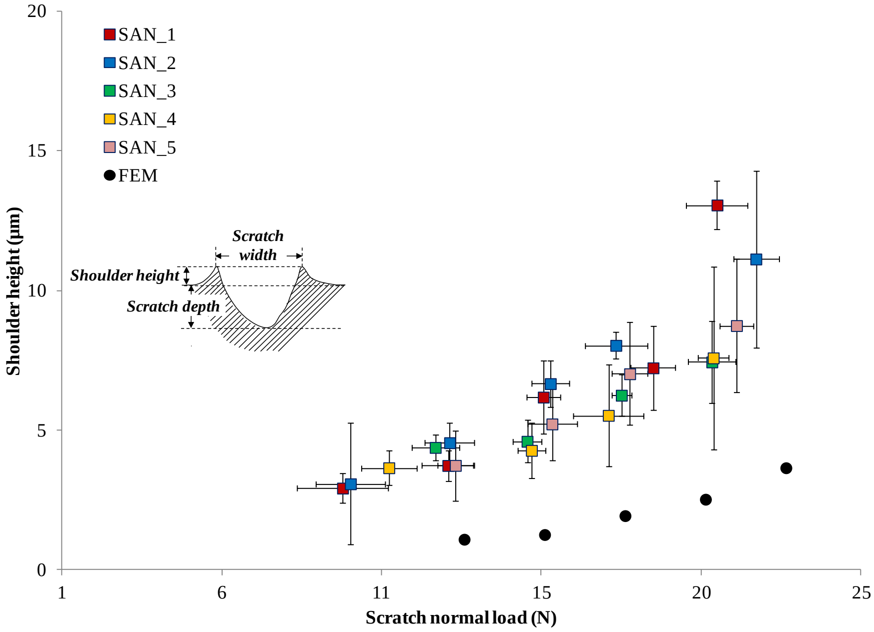

Figure 6.7. Comparison of FEM simulation and experiments on shoulder height evolution as a function of scratch normal load for SAN.

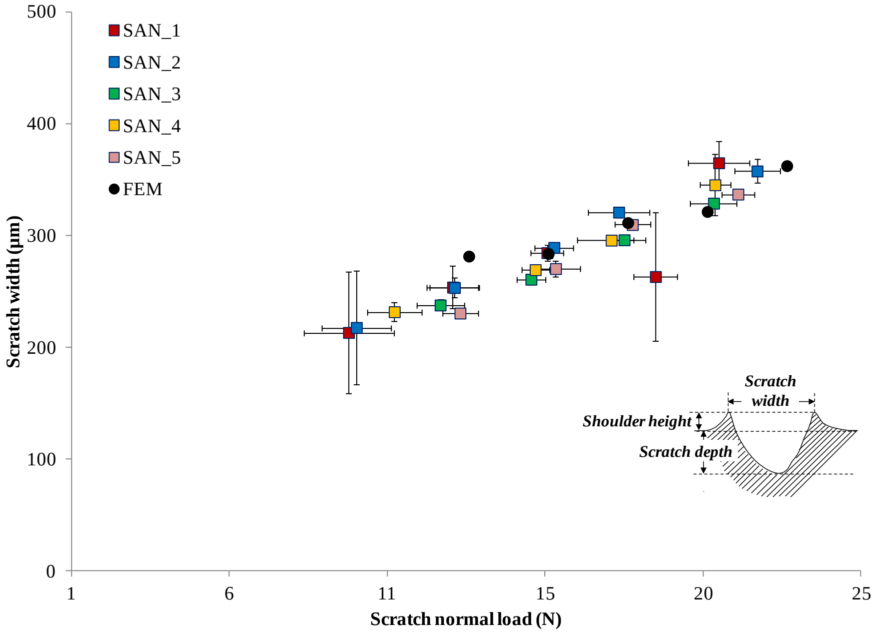

Figure 6.8. Comparison of FEM simulation and experiments on development of scratch width as a function of scratch normal load for SAN.

Similar to PC, Figure 6.9 shows the comparison of scratch coefficient of friction (SCOF) obtained during experiment for SAN with the friction value obtained from FEM simulation by adding the coefficient of adhesive friction and coefficient of friction due to deformation using Equation 3.10. As mentioned earlier, this method of calculating coefficient of friction is generally applicable for ductile materials. As shown in the figure, the FEM simulation overestimates the scratch coefficient of friction. Since SAN is brittle in tension, this simulation results indicate that indeed the frictional calculations for ductile polymers may not be applicable for brittle polymers.

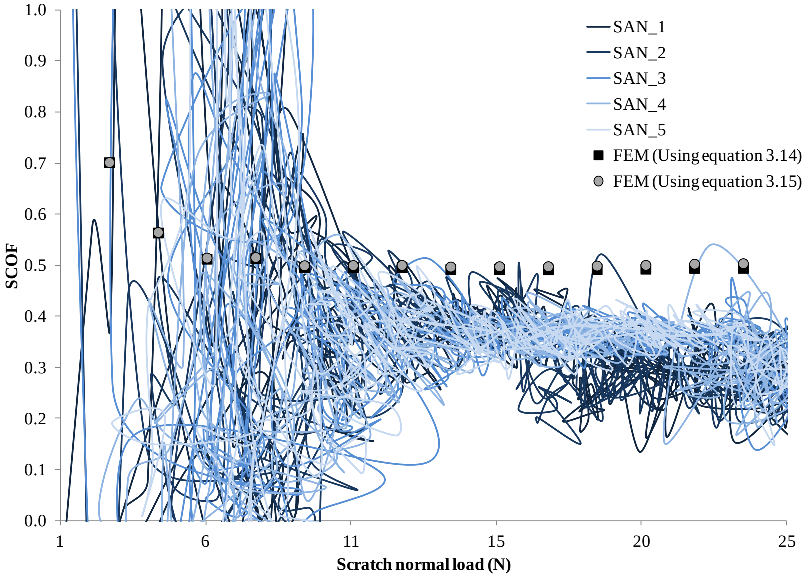

Figure 6.9. Comparison of scratch coefficient of friction (SCOF) obtained *via* experiments with development of friction calculated using FEM simulation for SAN.

Figure 6.10 shows the instantaneous scratch depth and residual scratch depth (or scratch depth) obtained *via* FEM simulation and the percent elastic recovery in case of SAN. As shown in the figure, the elastic recovery decreases with increasing normal load, but there is an elastic recovery of ~ 82% calculated at scratch normal load of 25 N. Similar to PC, the viscoelastic recovery can be considered insignificant and is reasonable not to include in the constitutive relationship for FEM modeling.

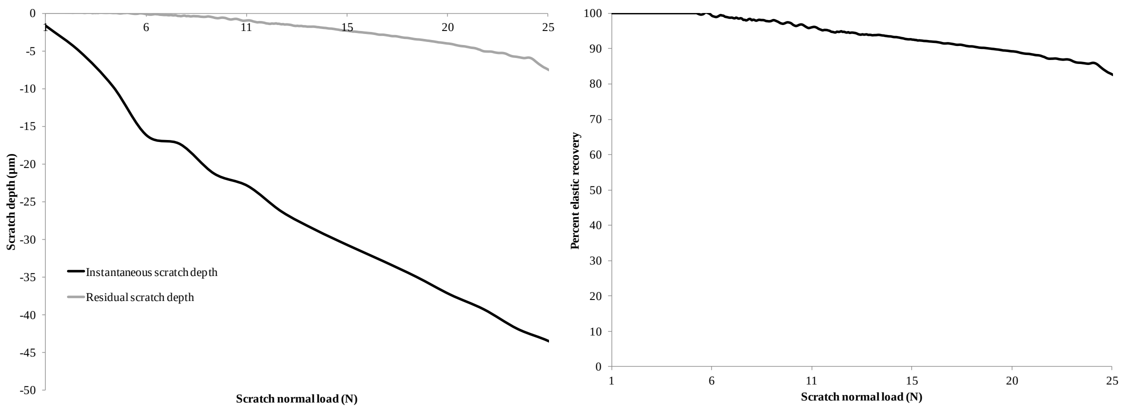

(a) (b)

Figure 6.10. FEM simulation findings on - (a) Instantaneous and residual scratch depth; and (b) Percent elastic recovery calculated; for SAN.

The discrepancy in shoulder height between FEM model and experiment for both model polymers can be attributed to the bulk material flow from the scratch tip front to the sides at higher loads, which contribute to the shoulder height formation. In this study, ABAQUS® default Lagrangian analysis was used which is insufficient in simulating the bulk material flow. An Arbitrary Lagrangian Eulerian (ALE) adaptive meshing option in ABAQUS®, which ranges from purely Lagrangian analysis to purely Eulerian analysis, can be used to simulate the shoulder height formation during scratch. Although it provides control of mesh distortion, the accuracy can be compromised while using this option. Furthermore, since the ALE adaptive technique allows material flow through the elements, although limited, it will affect the stress-strain correspondence in an element, and, thus, may result in faulty analysis. The discrepancy in FEM simulation and experiment can also be attributed to the simplistic constitutive model employed in this study. The rate dependency of modulus and Drucker-Prager coefficients which were not taken into account in this study may be partially responsible for the observed discrepancy between FEM simulation and experiments. Furthermore, the unavailability of triaixial test data for the model polymers and the assumption regarding that can also cause the variation. Thus, an appropriate constitutive relationship taking into account the aforementioned factors with adequate frictional model is expected to provide more accurate prediction of scratch-induced deformation in polymers.

CHAPTER VII

CONCLUSIONS AND CONSIDERATIONS FOR FUTURE RESEARCH

7.1 Summary and Conclusions

Numerical analyses along with experimental work were performed in this research effort in order to gain comprehensive understanding of polymer scratch behavior. The focuses of this study were as follows:

1. Using numerical modeling and experimental work, investigate the effect of material parameters and surface properties on the development of scratch-induced deformation features in polymers, qualitatively,
2. By employing theoretical model and experimental data, predict the rate dependent mechanical behavior of model polymers,
3. Identify and incorporate the key features of polymer constitutive behavior along with appropriate contact model in the FEM simulation to quantitatively predict the scratch behavior of model systems,
4. Quantitatively predict the scratch behavior of model polymers *via* FEM.

The qualitative study using FEM simulation and experiments show that the residual scratch depth and shoulder height formation during scratch are strongly influenced by compressive behavior, i.e., yield stress, strain at stress recovery and strain hardening slope beyond the strain at stress recovery in compression. Tensile behavior has little influence on the shoulder height and scratch depth formation but affects the surface roughness in the scratch groove along the scratch path. The onset of groove formation is primarily affected by compressive yield stress, which is influenced by coefficient of surface friction. Frictional effect on the evolution of scratch-induced deformation features in ductile polymers can be reduced by increasing the strain hardening slope. Thus, the qualitative study suggest that the scratch-induced deformation, such as shoulder height and scratch depth formation, and surface roughness inside the scratch groove can be correlated with the constitutive behavior of polymers. Furthermore, the effect of coefficient of friction on scratch-induced deformation can be altered by modifying the constitutive behavior of polymers.

Using the Ree-Eyring theory and experimental data at lower strain rates, the mechanical behavior of model polymers at high strain rate is predicted. The rate and pressure dependent material model is constructed based on these data. From the qualitative study and experimental observations, key characteristics of polymer constitutive behavior are identified and incorporated accordingly in the FEM model for quantitative prediction of scratch behavior of model polymers. The experimental study on model polymers shows that viscoelasticity of polymers plays a minor role on the scratch behavior. A pressure dependent frictional model is developed and included in the FEM model.

The correlation between the experimentally observed scratch-induced deformation and the FEM model shows reasonable success. Therefore, it can be pointed out that the choices of the constitutive relation, frictional behavior, and assumptions involved in the modeling are appropriate. Thus, by knowing the mechanical behavior and surface condition of polymers, one can predict the scratch behavior using FEM simulation. Consequently, the study facilitates understanding the scratch behavior of polymers in a more comprehensive fashion.

7.2 Considerations for Future Research

The findings presented in this dissertation, specifically, successful implementation of the quantitative modeling of polymer scratch behavior using FEM opens up new horizon of research to further our understanding in the field.

7.2.1 Extended Study on Quantitative Modeling

As the findings of this research suggest that the scratch behavior of polymers can by quantitatively modeled using FEM; similar approach can be taken for semi-crystalline polymers, e.g., PP. By knowing the rate, time, temperature and pressure dependent behavior of semi-crystalline polymers and employing an appropriate contact model, efforts can be made to quantify the scratch behavior. It would be interesting to learn if the current approach undertaken for amorphous polymers is sufficient for semi-crystalline polymers too, taking in to account the crystallinity effect. The same approach can also be extended to the thermosetting polymers such as epoxy. It would be of great impact if the modeling approach performed in this dissertation can be extended to different kind of polymers in order to establish a general model, as it would allow establishing quantitative correlation between material and surface properties with scratch-induced deformation in general polymers. This generalization would enable better and in-depth understanding of scratch behavior of polymers.

7.2.2 FEM Simulation of Brittle Damage Features Developed during Scratch

As discussed earlier, micro-cracking and/or crazing in the scratch groove can be a dominant deformation mechanism during scratch depending on the applied stress state and type of polymer utilized. Researchers have observed crazes in polystyrene (PS), crack formation in polycarbonate (PC) and epoxy using the ASTM/ISO scratch testing standard [7]. Thus, it would be of great interest to simulate the evolution of micro-crack formation inside the scratch groove during the scratch process.

An appropriate damage initiation criterion has to be used to simulate the beginning of failure or fracture during the scratch process. Subsequently, a damage evolution criterion has to be prescribed so that the material stiffness and load bearing capability could be gradually degraded when the damage initiation criterion is met. Finally, the element has to be removed from the mesh when the maximum degradation is reached to simulate the micro-crack formation. It has been shown experimentally using SAN model systems [8] that the onset of micro-cracking depends on tensile strength. Thus, rate and pressure dependent tensile behavior could be of prime importance for simulating the crack formation in addition to the compressive behavior. Successful implementation of crack simulation along with experimental study would allow understanding the stress and strain field developed in the crack formation during scratch, and, thus, comprehensive understanding of the mechanics behind it.

7.2.3 FEM Simulation of Fish-scale Formation during Scratch

Another area lacks comprehensive understanding is the onset and extent of fish-scale formation during scratch, generally observed in PP and TPO. It would be of great importance to understand the material and surface properties that is responsible for the stick-slip phenomenon which results in formation of fish-scales. The frictional properties of the polymers and interaction with the scratch tip need careful consideration in this respect. Thus, to simulate the fish-scale formation *via* FEM, efforts should be given to construct an appropriate contact model. Once modeled quantitatively, it would enable understanding scratch behavior of polymers in a more comprehensive fashion.

REFERENCES

[1] Browning, R.L., Jiang, H., Sue, H.-J., *Scratch behavior of polymeric materials*, in *Tribology of Polymeric Nanocomposites*, K. Friedrich, Schlarb, A.K., Editor. 2008, Elsevier: Oxford. p. 354-373.

[2] Lim, G.T., *Scratch behavior of polymers*, in *Mechanical Engineering*2005, Texas A&M University: College Station, Texas.

[3] Wong, M., Lim, G.T., Moyse, A., Reddy, J.N., Sue, H.-J., *A new test methodology for evaluating scratch resistance of polymers.* Wear, 2004. **256**(11-12): p. 1214-1227.

[4] Wong, M., *The Development of Scratch Test Methodology and Characterization of Surface Damage of Polypropylene*, in *Mechanical Engineering*2003, Texas A&M University: College Station, Texas.

[5] ASTM D7027-05, *Standard Test Method for Evaluation of Scratch Resistance of Polymeric Coatings and Plastics using an Instrumented Scratch Machine*, 2005, ASTM International: Pennsylvania.

[6] Jiang, H., Browning, R.L., Hossain, M.M., Sue, H.-J., Fujiwara, M., *Quantitative evaluation of scratch visibility resistance of polymers.* Applied Surface Science, 2010. **256**(21): p. 6324-6329.

[7] Jiang, H., Browning, R.L., Sue, H.-J., *Understanding of scratch-induced damage mechanisms in polymers.* Polymer, 2009. **50**(16): p. 4056-4065.

[8] Browning, R.L., Sue, H.-J., Minkwitz, R., Charoensirisomboon, P., *Effects of acrylonitrile content and molecular weight on the scratch behavior of styrene-acrylonitrile random copolymers.* Polymer Engineering & Science, 2011. **51**(11): p. 2282-2294.

[9] Jiang, H., Lim, G.T., Reddy, J.N., Whitcomb, J.D., Sue, H.-J., *Finite element method parametric study on scratch behavior of polymers.* Journal of Polymer Science Part B: Polymer Physics, 2007. **45**(12): p. 1435-1447.

[10] Hossain, M.M., Jiang, H., Sue, H.-J., *Effect of constitutive behavior on scratch visibility resistance of polymers-A finite element method parametric study.* Wear, 2011. **270**(11-12): p. 751-759.

[11] Hossain, M.M., Browning, R.L., Minkwitz, R., Sue, H.-J., *Effect of asymmetric constitutive behavior on scratch-induced deformation of polymers.* Tribology Letters, 2012. **47**(1): p. 113-122.

[12] Bucaille, J.L., Gauthier, C., Felder, E., Schirrer, R., *The influence of strain hardening of polymers on the piling-up phenomenon in scratch tests: Experiments and numerical modelling.* Wear, 2006. **260**(7-8): p. 803-814.

[13] Hossain, M.M., Minkwitz, R., Sue, H.-J., *Minimization of surface friction effect on scratch-induced deformation in polymers.* Polymer Engineering & Science, 2013. **53**(7): p. 1405-1413.

[14] Hossain, M.M., Jiang, H., Sue, H.-J. *Correlation between constitutive behavior and scratch visibility resistance of polymers-A finite element method parametric study*. in *SPE TPO Global Conference*. 2011. Detroit, Michigan.

[15] Reddy, J.N., *An Introduction to the Finite Element Method*. 2nd ed. 1993, New York: McGraw-Hill.

[16] Mackerle, J., *Finite element and boundary element simulations of indentation problems: A bibliography (1997–2000).* Finite Elements in Analysis and Design, 2001. **37**(10): p. 811-819.

[17] Lee, J.H., Xu, G.H., Liang, H., *Experimental and numerical analysis of friction and wear behavior of polycarbonate.* Wear, 2001. **251**(1-12): p. 1541-1556.

[18] Bucaille, J.L., Felder, E., Hochstetter, G., *Mechanical analysis of the scratch test on elastic and perfectly plastic materials with the three-dimensional finite element modeling.* Wear, 2001. **249**(5-6): p. 422-432.

[19] Subhash, G., Zhang, W., *Investigation of the overall friction coefficient in single-pass scratch test.* Wear, 2002. **252**(1-2): p. 123-134.

[20] Jiang, H., Browning, R.L., Whitcomb, J.D., Ito, M., Shimouse, M., Chang, T.A., Sue, H.-J., *Mechanical modeling of scratch behavior of polymeric coatings on hard and soft substrates.* Tribology Letters, 2010. **37**(2): p. 159-167.

[21] Lim, G.T., Wong, M., Reddy, J.N., Sue, H.-J., *An integrated approach towards the study of scratch damage of polymer.* JCT Research, 2005. **2**(5): p. 361-369.

[22] Jiang, H., *Experimental and numerical study of polymer scratch behavior*, in *Mechanical Engineering*2009, Texas A&M University: College Station, Texas.

[23] Pelletier, H., Gauthier, C., Schirrer, R., *Influence of the friction coefficient on the contact geometry during scratch onto amorphous polymers.* Wear, 2010. **268**(9-10): p. 1157-1169.

[24] Pelletier, H., Durier, A.-L., Gauthier, C., Schirrer, R., *Viscoelastic and elastic–plastic behaviors of amorphous polymeric surfaces during scratch.* Tribology International, 2008. **41**(11): p. 975-984.

[25] Schirrer, R., Gauthier, C., Pelletier, H., *Experimental and finite-element analysis of scratches on amorphous polymeric surfaces.* Proceedings of the Institution of Mechanical Engineers, Part J: Journal of Engineering Tribology, 2008. **222**(3): p. 221-230.

[26] Pelletier, H., Gauthier, C., Schirrer, R., *Strain and stress fields during scratch tests on amorphous polymers: Influence of the local friction.* Tribology Letters, 2008. **32**(2): p. 109-116.

[27] Bucaille, J.L., Felder, E., Hochstetter, G., *Experimental and three-dimensional finite element study of scratch test of polymers at large deformations.* Journal of Tribology, 2004. **126**(2): p. 372-379.

[28] Briscoe, B.J., Pelillo, E., Sinha, S.K., *Scratch hardness and deformation maps for polycarbonate and polyethylene.* Polymer Engineering & Science, 1996. **36**(24): p. 2996-3005.

[29] Briscoe, B.J., Evans, P.D., Pellilo, E., Sinha, S.K., *Scratching maps for polymers.* Wear, 1996. **200**(1-2): p. 137-147.

[30] Briscoe, B.J., Pelillo, E., Ragazzi, F., Sinha, S.K., *Scratch deformation of methanol plasticized poly(methylmethacrylate) surfaces.* Polymer, 1998. **39**(11): p. 2161-2168.

[31] Xiang, C., Sue, H.-J., Chu, J., Coleman, B., *Scratch behavior and material property relationship in polymers.* Journal of Polymer Science Part B: Polymer Physics, 2001. **39**(1): p. 47-59.

[32] Hamilton, G.M., Goodman, L.E., *The stress field created by a circular sliding contact.* Journal of Applied Mechanics, 1966. **33**(2): p. 371-376.

[33] Hamilton, G.M., *Explicit equations for the stresses beneath a sliding spherical contact.* Proceedings of the Institution of Mechanical Engineers, Part C: Journal of Mechanical Engineering Science, 1983. **197**(1): p. 53-59.

[34] Bellemare, S.C., Dao, M., Suresh, S., *Effects of mechanical properties and surface friction on elasto-plastic sliding contact.* Mechanics of Materials, 2008. **40**(4-5): p. 206-219.

[35] Hadal, R.S., Misra, R.D.K., *Scratch deformation behavior of thermoplastic materials with significant differences in ductility*. Materials Science and Engineering: A, 2005. **398**(1-2): p. 252-261.

[36] Browning, R.L., Lim, G.T., Moyse, A., Sun, L., Sue, H.-J., *Effects of slip agent and talc surface-treatment on the scratch behavior of thermoplastic olefins.* Polymer Engineering & Science, 2006. **46**(5): p. 601-608.

[37] van Melick, H.G.H., Govaert, L.E., Meijer, H.E.H., *On the origin of strain hardening in glassy polymers.* Polymer, 2003 **44**(8): p. 2493-2502.

[38] Tabor, D., Williams, D.E.W., *The effect of orientation on the friction of polytetrafluoroethylene.* Wear, 1961 **4**(5): p. 391-400.

[39] Bely, V.A., Savkin, V.G., Sviridyonok, A.I., *Effect of structure on polymer friction.* Wear, 1971. **18**(1): p. 11-18.

[40] ABAQUS. *ABAQUS® Analysis User's Manual, Version 6.9*. Available from: www.simulia.com.

[41] ASTM D638-10, *Standard Test Method for Tensile Properties of Plastics*, 2010, ASTM International: Pennsylvania.

[42] ASTM D695-10, *Standard Test Method for Compressive Properties of Rigid Plastics*, 2010, ASTM International: Pennsylvania.

[43] Jiang, H., Browning, R.L., Fincher, J., Gasbarro, A., Jones, S., Sue, H.-J., *Influence of surface roughness and contact load on friction coefficient and scratch behavior of thermoplastic olefins.* Applied Surface Science, 2008. **254**(15): p. 4494-4499.

[44] Richeton, J., Schlatter, G., Vecchio, K.S., Rémond, Y., Ahzi, S., *A unified model for stiffness modulus of amorphous polymers across transition temperatures and strain rates.* Polymer, 2005. **46**(19): p. 8194-8201.

[45] Siviour, C.R., Walley, S.M., Proud, W.G., Field, J.E., *The high strain rate compressive behaviour of polycarbonate and polyvinylidene difluoride.* Polymer, 2005. **46**(26): p. 12546-12555.

[46] Boyce, M.C., Arruda, E.M., *An experimental and anaiytical investigation of the large strain compressive and tensile response of glassy polymers.* Polymer Engineering & Science, 1990. **30**(20): p. 1288-1298.

[47] Moy, P., Weerasooriya, T., Hsieh, A., Chen, W., *Strain rate response of a polycarbonate under uniaxial compression.* Proceedings of the SEM Conference on Experimental Mechanics, 2003.

[48] Mulliken, A.D., Boyce, M.C., *Mechanics of the rate-dependent elastic–plastic deformation of glassy polymers from low to high strain rates.* International Journal of Solids and Structures, 2006. **43**(5): p. 1331-1356.

[49] Robertson, R.E., *Theory for the plasticity of glassy polymers.* Journal of Chemical Physics, 1966. **44**(10): p. 3950-3956.

[50] Argon, A.S., *A theory for the low-temperature plastic deformation of glassy polymers.* Philosophical Magazine, 1973. **28**(4): p. 839-865.

[51] Ree, T., Eyring, H., *Theory of non-Newtonian flow. I. Solid plastic system.* Journal of Applied Physics, 1955. **26**(7): p. 793-800.

[52] Eyring, H., *Viscosity, plasticity, and diffusion as examples of absolute reaction rates.* Journal of Chemical Physics, 1936. **4**(4): p. 283-291.

[53] Mulliken, A.D., *Low to high strain rate deformation of amorphous polymers : Experiments and modeling*, in *Mechanical Engineering*2004, Massachusetts Institute of Technology: Massachusetts.

[54] Richeton, J., Ahzi, S., Daridon, L., Rémond, Y., *Modeling of strain rates and temperature effects on the yield behavior of amorphous polymers*. Journal of Physics IV France, 2003. **110**: p. 39-44. Available from: http://jp4.journaldephysique.org/.

[55] Bauwens, J.C., Bauwens-Crowet, C., Homès, G., *Tensile yield-stress behavior of poly(vinyl chloride) and polycarbonate in the glass transition region.* Journal of Polymer Science Part A-2: Polymer Physics, 1969. **7**(10): p. 1745-1754.

[56] Bauwens-Crowet, C., Bauwens, J.C., Homès,G., *Tensile yield-stress behavior of glassy polymers.* Journal of Polymer Science Part A-2: Polymer Physics, 1969. **7**(4): p. 735-742.

[57] Bauwens, J.C., *Relation between the compression yield stress and the mechanical loss peak of bisphenol-A-polycarbonate in the β transition range.* Journal of Materials Science, 1972. **7**(5): p. 577-584.

[58] Bauwens-Crowet, C., Bauwens, J.C., Homès, G., *The temperature dependence of yield of polycarbonate in uniaxial compression and tensile tests.* Journal of Materials Science, 1972. **7**(2): p. 176-183.

[59] Bauwens-Crowet, C., *The compression yield behaviour of polymethyl methacrylate over a wide range of temperatures and strain-rates.* Journal of Materials Science, 1973. **8**(7): p. 968-979.

[60] Roetling, J.A., *Yield stress behaviour of poly(ethyl methacrylate) in the glass transition region.* Polymer, 1965. **6**(11): p. 615-619.

[61] Roetling, J.A., *Yield stress behaviour of polymethylmethacrylate.* Polymer, 1965. **6**(6): p. 311-317.

[62] Rietsch, F., Bouette, B., *The compression yield behaviour of polycarbonate over a wide range of strain rates and temperatures.* European Polymer Journal, 1990 **26**(10): p. 1071-1075.

[63] Richeton, J., Ahzi, S., Vecchio, K.S., Jiang, F.C., Adharapurapu, R.R., *Influence of temperature and strain rate on the mechanical behavior of three amorphous polymers: Characterization and modeling of the compressive yield stress.* International Journal of Solids and Structures, 2006. **43**(7-8): p. 2318-2335.

[64] Okereke, M.I., Buckley, C.P. *High-rate compression of polypropylene*. in *IV International Conference on Times of Polymers (TOP) and Composites*. 2008. Ischia (Italy): American Institute of Physics.

[65] Okereke, M.I., Buckley, C.P., Siviour, C.R., *Compression of polypropylene across a wide range of strain rates.* Mechanics of Time-Dependent Materials, 2012. **16**(4): p. 361-379.

[66] Wang, Y., Arruda, E.M., *Constitutive modeling of a thermoplastic olefin over a broad range of strain rates.* Journal of Engineering Materials and Technology, 2006. **128**(4): p. 551-558.

[67] Omar, M.F., Akil, H.M., Ahmad, Z.A., *Mechanical properties of nanosilica/polypropylene composites under dynamic compression loading.* Polymer Composites, 2011. **32**(4): p. 565-575.

[68] Spitzig, W.A., Richmond, O., *Effect of hydrostatic pressure on the deformation behavior of polyethylene and polycarbonate in tension and in compression.* Polymer Engineering & Science, 1979. **19**(16): p. 1129-1139.

[69] Sauer, J.A., Mears, D.R., Pae, K.D., *Effects of hydrostatic pressure on the mechanical behaviour of polytetrafluoroethylene and polycarbonate.* European Polymer Journal, 1970. **6**(7): p. 1015-1032.

[70] Powers, J.M., Caddell, R.M., *The macroscopic volume changes of selected polymers subjected to uniform tensile deformation.* Polymer Engineering & Science, 1972. **12**(6): p. 432-436.

[71] Kitagawa, M., Yoneyama, T., *Plastic dilatation due to compression in polymer solids.* Journal of Polymer Science Part C: Polymer Letters, 1988. **26**(4): p. 207-212.

[72] Bowden, F.P., Tabor, D., *The Friction and Lubrication of Solids: Part I.* 1954, Oxford, England: Clarendon Press.

[73] Bhushan, B., *Introduction to Tribology*. 2nd ed. 2013, New York: John Wiley & Sons Ltd.

[74] Wong, M., Moyse, A., Lee, F., Sue, H.-J., *Study of surface damage of polypropylene under progressive loading.* Journal of Materials Science, 2004. **39**(10): p. 3293-3308.

[75] Bowden, F.P., Tabor, D., *The Friction and Lubrication of Solids: Part II.* 1964, Oxford, England: Clarendon Press.

[76] Briscoe, B.J., Tabor, D., *Shear properties of thin polymeric films.* The Journal of Adhesion, 1978. **9**(2): p. 145-155.

[77] Bowers, R.C., *Coefficient of friction of high polymers as a function of pressure.* Journal of Applied Physics, 1971. **42**(12): p. 4961-4970.

[78] Briscoe, B.J., Tabor, D., *The effect of pressure on the frictional properties of polymers.* Wear, 1975 **34**(1): p. 29-38.

[79] Amuzu, J.K.A., Briscoe, B.J., Tabor, D., *Friction and shear strength of polymers.* ASLE Transactions, 1977. **20** (4): p. 354-358.

[80] Duckett, R.A., Goswami, B.C., Smith, L.S.A., Ward, I.M., Zihlif, A.M., *The yielding and crazing behaviour of polycarbonate in torsion under superposed hydrostatic pressure.* British Polymer Journal, 1978. **10**(1): p. 11-16.

[81] Rabinowitz, S., Ward, I.M., Parry, J.S.C., *The effect of hydrostatic pressure on the shear yield behaviour of polymers.* Journal of Materials Science, 1970. **5**(1): p. 29-39.

[82] Suh, N.P., Sin, H.-C., *The genesis of friction.* Wear, 1981 **69**(1): p. 91-114.

[83] Blok, H., *Theoretical study of temperature rise at surfaces of actual contact under oiliness lubricating conditions.* Proceedings of the Institution of Mechanical Engineers, 1937. **2**: p. 222-235.

[84] Jaeger, J.C., *Moving sources of heat and the temperature of sliding contacts.* Proceedings of Royal Society of New South Wales, 1942. **76**: p. 203-224.

[85] Archard, J.F., *The temperature of rubbing surfaces.* Wear, 1959. **2**(6): p. 438-455.

[86] Archard, J.F., Rowntree, R.A., *The temperature of rubbing bodies; part 2, the distribution of temperatures.* Wear, 1988. **128**(1): p. 1-17.

[87] Ashby, M.F., Abulawi, J., Kong, H.S., *Temperature maps for frictional heating in dry sliding.* Tribology Transactions, 1991. **34**(4): p. 577-587.

[88] Gulino, R., Bair, S., Winer, W.O., Bhushan, B., *Temperature measurement of microscopic areas within a simulated head/tape interface using infrared radiometric technique.* Journal of tribology, 1986. **108**(1): p. 29-34.

[89] Bhushan, B., *Magnetic head-media interface temperatures: Part 2-Application to magnetic tapes.* Journal of Tribology, 1987. **109**(2): p. 252-256.

[90] Wong, J., Campen, S., *Tribology of PEEK.*

[91] Locati, G., Tobolsky, A.V., *Studies of the toughness of polycarbonate of bisphenol a in light of its secondary transition.* Advances in Molecular Relaxation Processes, 1970 **1**(4): p. 375-408.

[92] Neto, E.A.d.S., Peri´c, D., Owen, D.R.J., *Computational Methods for Plasticity: Theory and Applications*. 2008, West Sussex, UK: John Wiley & Sons Ltd.

[93] Drucker, D.C., Prager, W., *Soil mechanics and plastic analysis or limit design.* Quarterly Journal of applied mathematics, 1952. **10**(2): p. 157-165.

[94] Anandarajah, A., *Computational Methods in Elasticity and Plasticity: Solids and Porous Media*. 2010, New York: Springer.

[95] Bardia, P., Narasimhan, R., *Characterisation of pressure-sensitive yielding in polymers.* Strain, 2006. **42**(3): p. 187-196.

[96] Rittel, D., Dorogoy, A., *A methodology to assess the rate and pressure sensitivity of polymers over a wide range of strain rates.* Journal of the Mechanics and Physics of Solids, 2008. **56**(11): p. 3191-3205.

[97] Seltzer, R., Cisilino, A.P., Frontini, P.M., Mai, Y.-W., *Determination of the Drucker–Prager parameters of polymers exhibiting pressure-sensitive plastic behaviour by depth-sensing indentation.* International Journal of Mechanical Sciences, 2011. **53**(6): p. 471-478.

[98] Dean, G., Wright, L., *An evaluation of the use of finite element analysis for predicting the deformation of plastics under impact loading.* Polymer Testing, 2003. **22**(6): p. 625-631.

[99] Chowdhury, K.A., Benzerga, A.A., Talreja, R., *A computational framework for analyzing the dynamic response of glassy polymers.* Computer Methods in Applied Mechanics and Engineering, 2008. **197**(49-50): p. 4485-4502.

[100] ABAQUS. *ABAQUS® Analysis User's Manual, Version 6.7*. Available from: www.simulia.com.

APPENDIX A

EFFECT OF MESHING

The effect of three different meshing along the critical length (A-B) of the FEM model was investigated to find optimum meshing for the numerical study. It should be mentioned that, the finer the mesh the more computation time is required for completing the simulation. Also, the slower the scratch speed the more computation time is required. Thus, FEM simulation on two different scratch speeds by scaling the constitutive relation in order to get the scratch behavior comparable with the experiment is conducted on three different meshes. Table A.1 lists the element dimension of the three different meshing adopted in this investigation.

Table A.1. Mesh information to study the effect of meshing.

Number of elements along the critical length (A-B)	Element dimension
256	45.8 μm × 56.3 μm × 46.7 μm
512	22.8 μm × 28.1 μm × 33.3 μm
1024	11.6 μm × 14.1 μm × 15 μm

Figure A.1 shows the effect of meshing on scratch depth obtained *via* FEM simulation of scratch behavior of PC. As shown in the figure, the scratch depths for all the meshes agree reasonably well. Similar results have been found in simulating scratch depth of SAN and also in shoulder height development for both PC and SAN. Thus, a mesh of 512 elements along the critical length (A-B) was chosen in this study.

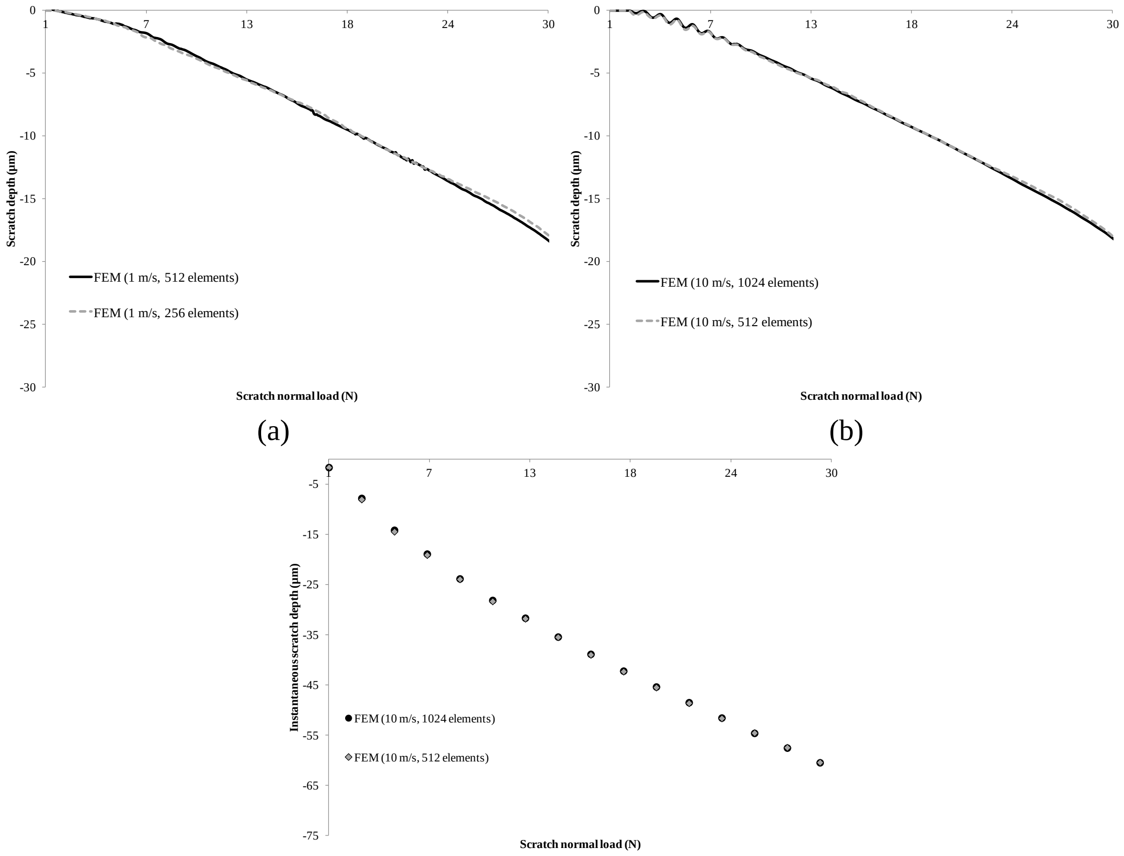

(a) (b)

(c)

Figure A.1. Effect of meshing on - (a) Scratch depth formation at 1 m/s; (b) Scratch depth formation at 10 m/s; and (c) Instantaneous scratch depth formation at 10 m/s; during FEM simulation of PC scratch.

APPENDIX B

EFFECT OF SCRATCH SPEED

As mentioned earlier, although the scratch experiments on PC and SAN model systems were done at 100 mm/s, FEM simulation for this scratch speed with the meshing adopted in this study requires enormous amount of computation time. As a result, to reduce the computation time, the FEM simulation was carried out at two different speeds (1 m/s and 10 m/s) to find the optimum speed with reasonable accuracy. The constitutive relationship was scaled accordingly in order to get the scratch behavior at 100 mm/s. As mentioned earlier, the slower the scratch speed the more computation time is required. Figure B.1 shows the FEM simulation results of scratch depth development in PC. As can be deduced from the figure, since the constitutive relationship was scaled accordingly, the FEM simulation of scratch speed of 10 m/s is expected to provide results corresponding to the experimental data at 100 mm/s. Similar results were also obtained for scratch depth of SAN and shoulder height of both PC and SAN. Thus, a scratch speed of 10 m/s was chosen for the FEM simulation with the constitutive relation scaled accordingly in order to save computation time.

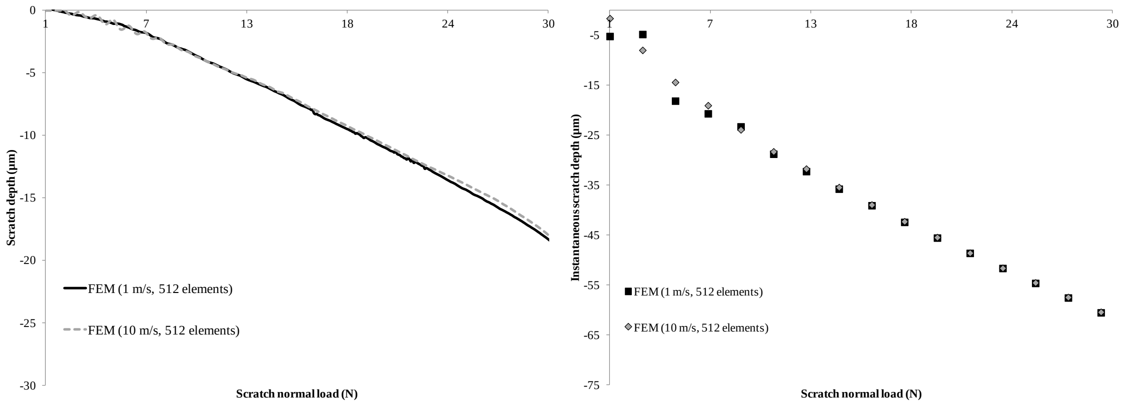

(a) (b)

Figure B.1. Effect of scratch speed on **-** (a) Scratch depth; and (b) Instantaneous scratch depth formation; during FEM simulation of scratch behavior of PC.

APPENDIX C

EFFECT OF LOAD GRADIENT

The scratch tests on PC and SAN model system were conducted at a scratch normal load of 1-70 N with a scratch length of 100 mm. Therefore, the load gradient in the experiment was 0.69 N/mm which is much lower than that used in FEM simulation. In FEM simulation, to save computation time, the scratch length was 12 mm and, for PC, the scratch normal load was 1-35 N, rendering a load gradient of 2.83 N/mm. The effect of this difference in load gradient was studied in this part to investigate its effect on scratch depth. As shown in Figure C.1, the effect is negligible and the difference in load gradient between experiment and FEM simulation can be neglected.

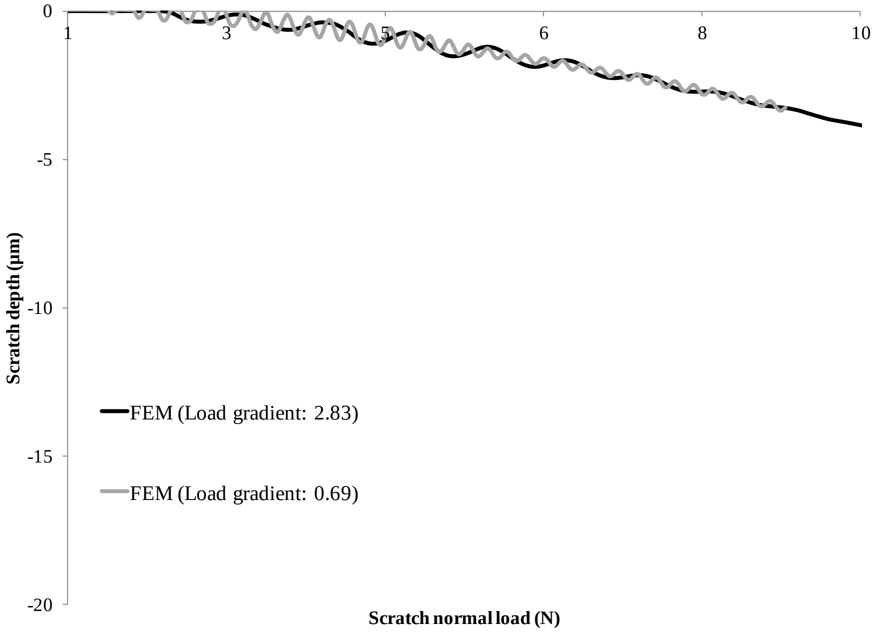

Figure C.1. Effect of load gradient on scratch depth formation during FEM simulation of scratch behavior of PC.